Electromechanical Fatigue Process of Lead-Free Alkali Niobate Piezoceramics

March 2016

Alexander Martin

Table of contents

1 Introduction

Electroceramics are used in a very broad range of functional ceramics, making them important materials for the industry. By forming the materials for the majority of electronic applications, such as capacitors, actuators, and sensors, electroceramics command a large market. In 2015, the export sales in Japan were about 4 trillion Yen (~ 30 billion $). Figure 1.1 (a) and (b) show how these sales numbers are separated in different areas of electroceramics.

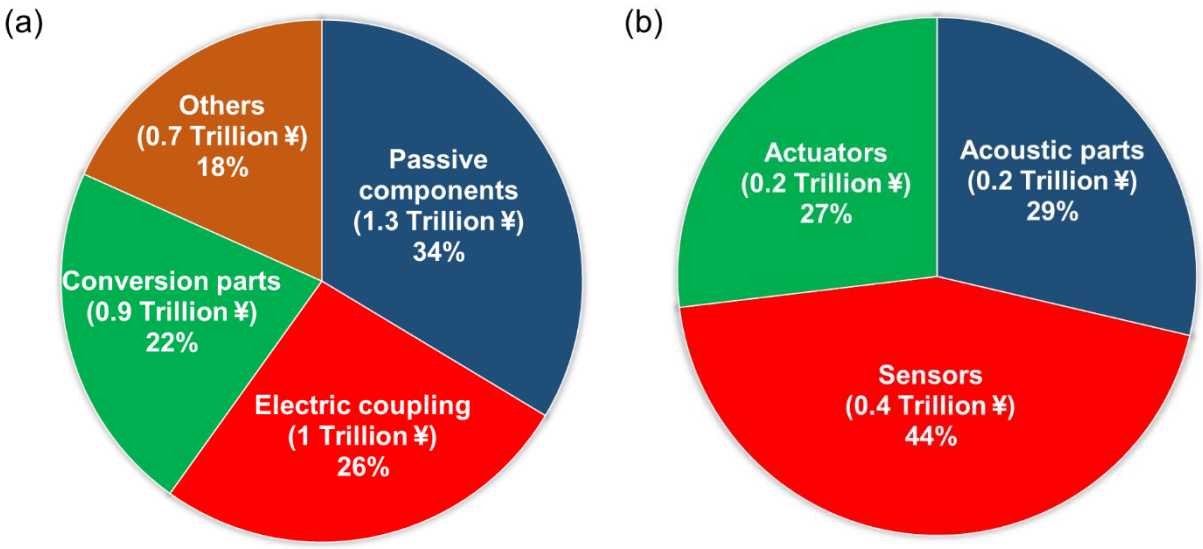

Figure 1.1: Market share of different electroceramics (a) and conversion parts (b). Numbers taken from [1]

The major focus of this study dealt with piezoceramics, which belong to the area of conversion parts and are further separated into three main subgroups, which are shown in Figure 1.1 (b). It should be noted that the subgroup of actuators not only contains the sales of piezoelectric actuators. However, these figures give a good insight on the whole market of piezoceramics. The advantages of those materials are their high efficiency, unlimited resolution and ultrahigh accelerations.[2–4] For this reason, they can be found in many different applications such as fuel injectors, nanopositioners and pulse drive motors, which involve the coupling of mechanical strains with high electric AC fields. Under these conditions the material is susceptible to changes in their characteristics. It was shown that lead zirconate titanates (abbreviated as PZT) decrease in piezoelectric and dielectric properties after a certain

amount of electric cycles. Electric cycles can be applied as unipolar, bipolar or sesquipolar. Depending on the kind of the electric field, different processes can be deduced as the main reasons for these degradations. In case of bipolar and sesquipolar fatigue, domain pinning is the major process. Space charge accumulation occurs during unipolar cycling, and describes the shift of space charges due to a depolarization field and their accumulation at the grain boundary. In all three cases, a second and more critical process can occur, which is micro crack formation. Not only causes it a decrease in the electric and piezoelectric properties, but also additional degradation in the mechanical strength[5,6]. More information about the occurring processes that lead to these changes can be deduced from fatigue experiments. Given the widespread use of PZT in industrial applications, most fatigue studies published in the scientific literature deal with lead-based materials. Detailed reviews were given by Genenko et al. and by Lupascu and Rödel for bulk PZT[6,7].

Nevertheless, a major problem is the lead contained in these materials, which volatilizes during calcination and sintering. It ends up mainly in the form of hazardous lead oxide in the environment. In 2003, the European Union (EU) included in its legislation PZT as a material to be substituted by safer materials in electric and electronic equipment. This led to an acceleration in the research and development of lead-free alternatives over the past few years. In 2004, the research of Saito et al. showed a highly promising alternative in sodium potassium niobate-based ceramics with the general chemical formula of $Na_xK_{1-x}NbO_3$ (abbreviated as NKN). The piezoelectric coefficients d_{ij} of NKN ceramics are relatively low compared with those of PZT, but the Curie temperature is comparatively high (T_C = 420 °C).[7,8] Pure NKN undergoes a polymorphic phase transition from orthorhombic to tetragonal structure at temperatures of about 200 °C (T_{O-T}). By doping NKN ceramics with Li [$Li_x(Na_{0.5}K_{0.5})_{1-x}NbO_3$] (abbreviated as LNKN), the orthorhombic-tetragonal phase transition temperature decreases even further and at Li contents in the range $0.05 < x < 0.07$, the polymorphic phase boundary between orthorhombic and tetragonal phases is stabilized at room temperature.

Figure 1.2 (a) and (b) show a collection of values from the literature for different piezoelectric materials and their respective piezoelectric coefficient d_{33} and permittivity ε. Both values are shown as a function of the relative Curie temperature.

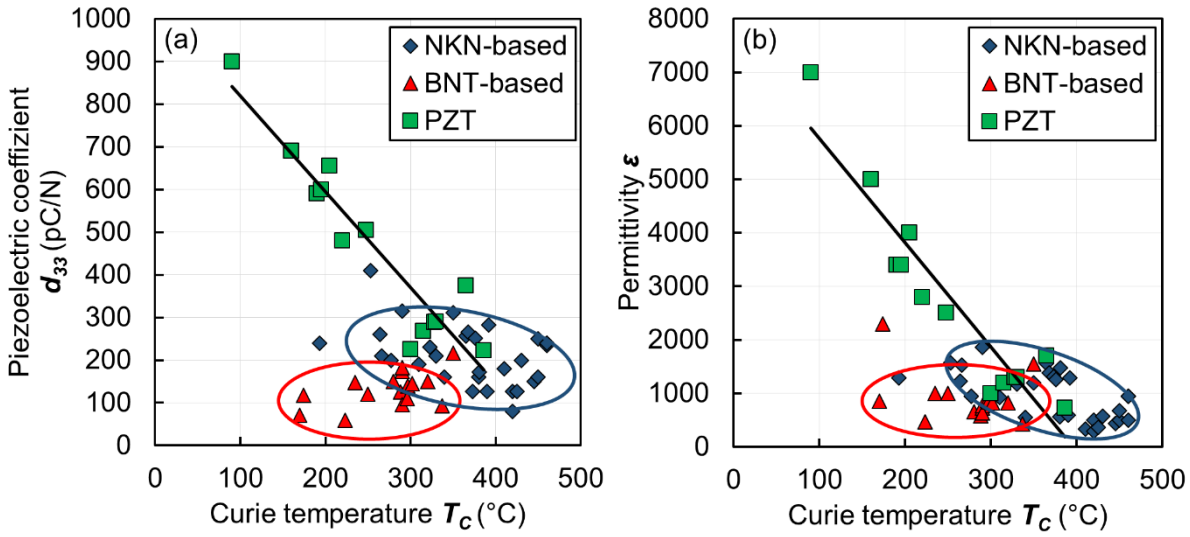

Figure 1.2: Various values of piezoelectric coefficient d_{33} and permittivity ε as a function of Curie temperature T_C. Values were taken from [8–11]

Figure 1.2 (a) shows the aforementioned points about the d_{33} value of NKN compared to PZT. Overall, NKN-based ceramics have lower piezoelectric coefficients, but by taking the Curie temperature into account, they are on par with PZT. BNT-based ceramics possess lower piezoelectric coefficients and Curie temperatures compared to PZT and NKN-based materials. From Figure 1.2 (b) can be concluded, that NKN ceramics and consequently LNKN ceramics have a lower permittivity ε than PZT and therefore do not generate much heat during application.[12] Furthermore, LNKN ceramics can be cofired with Cu[13], have high piezoelectric properties and Curie temperature (T_C = 460 °C).[14,15] Therefore, these materials are promising for industrial applications, such as multilayer actuators under high temperature conditions. Although NKN-based ceramics were extensively studied since 2004, only a few publications dealt with the fatigue behavior of alkali niobate ceramics.[16–21]

The influence of mechanical degradation has not been observed in any of these studies. Before observing the mechanical degradation, it is important to know the mechanical properties of NKN based ceramics. Only a few publications were published with mechanical properties of NKN ceramics as the focus of attention.[22–24] To determine the mechanical properties of ceramic materials in general, flexural tests have proven to be the most reliable. Besides the usual factors for the mechanical strength, such as grain size and porosity, piezoelectric materials have a complex electro mechanical coupling relationship. Therefore, the strength of piezoelectric materials is affected by the strength and direction of an applied electric field. In order to estimate the flexural strength of piezoceramics, these factors need to be considered. In the case of PZT, if an external electric field is applied, the flexural strength decreases.[25,26]

For the above mentioned reasons, this work has the following objectives:

1 Determination of mechanical properties of lead-free alkali niobate ceramics
2 Influence of different electric field conditions
   2.1 DC-field
   2.2 unipolar AC-field
   2.3 bipolar AC-field
3 Observation of fatigue behavior under harsh environments, such as high pressure and temperature

These points will then give information about NKN-based ceramics and whether or not these materials can be applied in industrial application.

2 Theoretical background and state of the art

In this chapter, the theories behind ferroelectricity and piezoelectricity are discussed briefly. The information used can be found in detail in references [8–11]. Furthermore, a summary of lead-free alkali niobate piezoelectric materials is given as well as an overview of the literature in the field of fatigue.

2.1 Electroceramics

Ferroelectric materials are a specific subclass, which combine dielectric and piezoelectric characteristics in addition to ferroelectric characteristics. Figure 2.1 shows the subclasses of dielectrics and the relationship between the aforementioned classes.

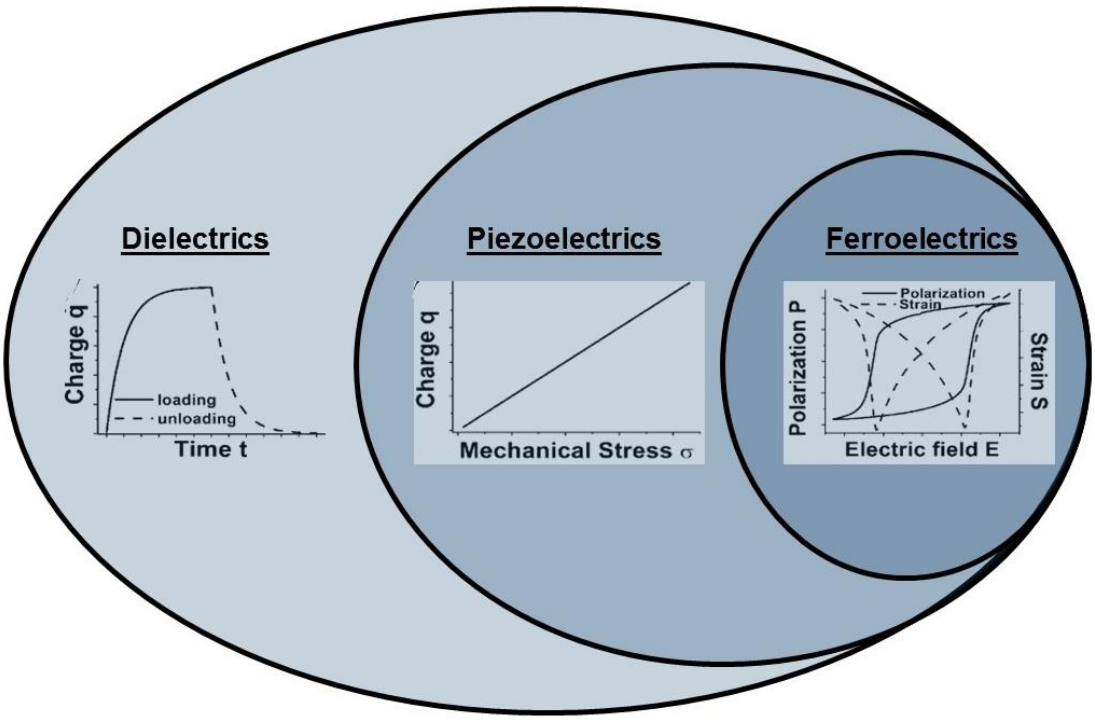

Figure 2.1: Subclasses of dielectrics and examples of their application. Taken from [27)]

2.1.1 Dielectric ceramics

Insulators and dielectrics can be defined as materials with high electric resistivity. In practice, most of these materials are solid, such as ceramics, glass, plastics, and the oxides of various metals. Whereas insulators are primarily used for shielding

conductive elements, dielectrics have a wide variety of uses. The reason is that if an electric field is applied onto an ideal dielectric material, no charge transportation occurs. Instead, charge displacements in the material shift relative to each other, thereby acquiring a dipole moment and polarize the material. This induced polarization can be subdivided into 4 different variations:

- *Atomic polarization:* relative shift of the electron cloud to the positive nucleus
- *Ionic polarization:* displacement of ions from their initial position
- *Dipolar polarization*: existing dipoles are aligned to the electric field
- *Space charge polarization*: free charge carrier are separated in certain regions

For better understanding, we consider a dielectric material, which is placed in between two parallel placed plates. If a voltage is applied onto this set-up an electric field ***E*** as well as dielectric displacement ***D*** emanates from these electrodes. The relationship between both physical quantities is defined by the equation:

$$D_i = \varepsilon_0 \varepsilon_{ij} \cdot E_j + P_j \tag{2.1}$$

with ***P*** as the polarization, $\boldsymbol{\varepsilon_0}$ and $\boldsymbol{\varepsilon_{ij}}$ as the permittivity of the vacuum and material, respectively. The subscripts describe the direction of the physical quantity in a 3-dimensional Cartesian space. The permittivity of the material describes the charge stored on an electrode slab during application of a voltage and the permittivity of the vacuum describes the charge stored on a set of identical electrodes separated by vacuum. The latter is a natural constant and has a value of $\boldsymbol{\varepsilon_0} = 8.85 \cdot 10^{-12}\,{}^{\mathrm{F}}/_{\mathrm{m}}$.

2.1.2 Piezoelectric ceramics

Besides polarization, the displacement of charges can also cause deformation, which is called electrostriction. It is a phenomenon which is present very weakly in all materials, but only observable in isolating materials, because in conductive materials electric fields are shielded by free charge carriers. The deformation ***S*** is hereby proportional to the applied electric field ***E***. In materials with special crystal structure, the piezoelectric effect can also occur besides electrostriction.

In nature, solid materials appear in crystalline as well as in non-crystalline (amorphous) form, whereas the former possesses higher binding forces between the atoms.

Crystals can be thought of as an array of smaller crystals, called unit cells. Such a unit cell is the smallest unit of volume that contains all of the structural and symmetry information of the lattice. Most of the materials are polycrystalline, meaning they consist of crystal areas of varying sizes called grains. Depending on their geometry, crystals are commonly classified into seven systems. These systems can again be subdivided into point groups (crystal classes) according to their symmetry with respect to a point. There are 32 such crystal classes and 11 possess a center of symmetry. For all 32 systems, mechanical stress $\boldsymbol{\sigma}$ causes a proportional strain $\boldsymbol{S}$. However, for the 21 non-centric crystal classes, all except one additionally create an electric charge when subject to stress $\boldsymbol{\sigma}$. This characteristic is called the direct piezoelectric effect. In terms of dielectric displacement, the equation changes to the following:

$$D_i = \varepsilon_0 \varepsilon_{ij} \cdot E_j + d_{jk} \cdot \sigma_k \tag{2.2}$$

Moreover, if an electric field is applied to a piezoelectric material a certain strain $\boldsymbol{S}$ can be measured and is called the inverse piezoelectric effect.

$$S_i = d_{ij} \cdot E_j \tag{2.3}$$

In both cases, the proportional constant is the piezoelectric coefficient $\boldsymbol{d_{ij}}$. A high piezoelectric coefficient is desirable for materials intended to develop motion or vibration, such as sonar or ultrasonic cleaner transducers. Furthermore, the piezoelectric effect can be described with the electromechanical coupling factor $\boldsymbol{k}$. It measures the fraction of the electrical energy converted to mechanical energy and vice versa. The relationship can be described by the following equations:

$$k_{ij}^2 = \frac{output\ mechanical\ (electrical)\ energy}{input\ electrical\ (mechanical)\ energy} \tag{2.4}$$

Typical values of $\boldsymbol{k_{ij}}$ are 0.4 – 0.5 for lead free piezoceramics, such as barium titanate and alkali niobate ceramics and 0.5 - 0.7 for PZT.

2.1.3 Ferroelectric ceramics

A further subdivision of piezoelectric materials are ferroelectrics. In polar crystals, ferroelectricity is defined as the reversibility of the direction of the spontaneous polarization $\boldsymbol{P_S}$ by means of an applied electric field. Since it requires polarity in a crystal, it can occur only in 10 of the 20 previous non-centric crystal classes, because they contain a spontaneous polarization in the unstrained condition. As with grains, which represent a uniform collection of one unit cell, domains exist in ferroelectric materials which consist of a uniform polarization direction. Moreover, neighboring domains with different preferential directions are separated by domain walls. Hereafter, the details of ferroelectric characteristics will be explained on the basis of lead-free alkali niobate ceramics and their perovskite structure, to which for example $BaTiO_3$, $PbTiO_3$ and $KNbO_3$ belong.

2.2 Lead free alkali niobate ceramics

Figure 2.2 shows the perovskite structure, which is an example of a unit cell capable of a spontaneous polarization $\boldsymbol{P_S}$. The perovskite structure has the structural formula of ABO_3. In this case, ions on the A side consist of large metal cations such as K, or Pb, whereas ions on the B side are mostly small cations such as Nb^{5+} or Ti^{4+}.

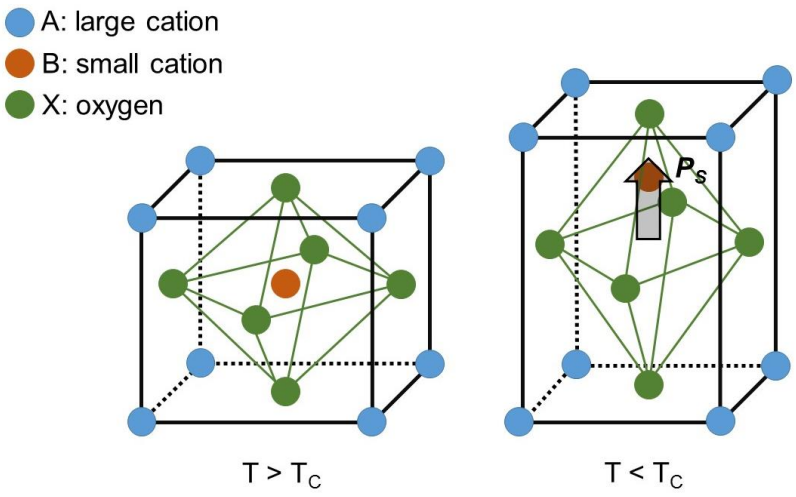

Figure 2.2: Unit cell of perovskite structure and dipole formation underneath Curie temperature.

Matthias et al. firstly reported the ferroelectric character of the mixed solution of $NaNbO_3$ and $KNbO_3$, by measuring the dielectric properties over a certain temperature range.[28] Since then, the solid solution $Na_xK_{1-x}NbO_3$ (abbreviated as NKN) was well studied regarding crystal structure, processing as well as dielectric, ferroelectric and piezoelectric characteristics. The phase diagram is depicted in Figure 2.3.

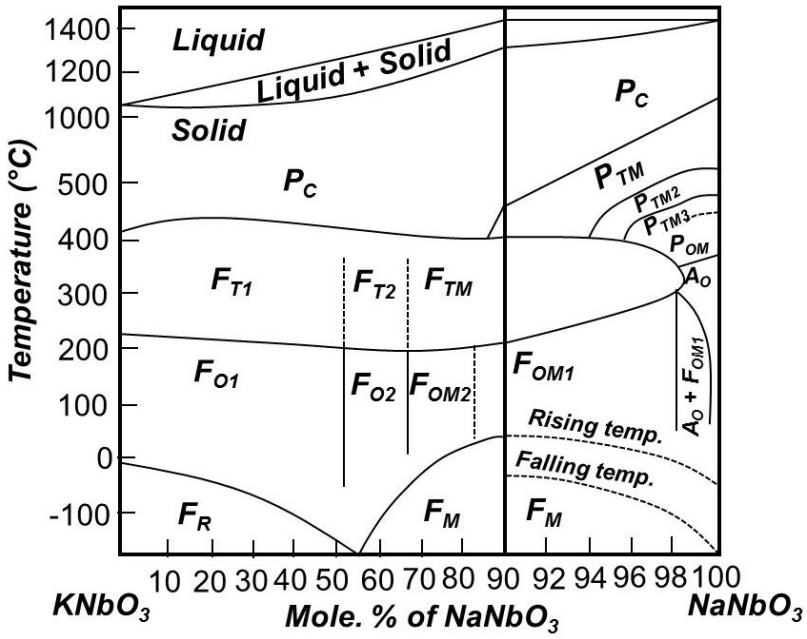

Figure 2.3: Phase diagram of $KNbO_3$ and $NaNbO_3$.Taken from[8].

Noteworthy is that the substitution of K ions with Na ions, does not change the phase transition temperatures significantly, except for the orthorhombic-rhombohedral transition at negative temperatures. This fact is represented by the two nearly horizontal lines at about 200 °C and 400 °C. The latter represents the Curie temperature T_C. By heating the material over this temperatures, the material has a cubic structure and shows no piezo- or ferroelectric properties. This state is called paraelectric. If the temperature is lowered underneath this temperature, the crystal structure deforms depending on the material composition. In case of NKN, the material transforms first into a tetragonal structure at temperatures around 420 °C. A phase-transformation from tetragonal to orthorhombic $T_{O\text{-}T}$ occurs at around 200 °C. Both phases show piezo- and ferroelectric characteristics. The phase diagram is comprised of another ferroelectric monoclinic region and an orthorhombic antiferroelectric region. These antiferroelectric phases are found in Na-rich compositions since $NaNbO_3$

possesses an orthorhombic antiferroelectric phase at room temperature. Two electric field-enforced phases with a rhombohedral and a monoclinic structure with ferroelectric properties also exist at low temperatures.

In case of a ferroelectric phase, the B-ion shifts from its central position, thereby forming a spontaneous polarization $\boldsymbol{P_S}$ and conclusively domains and domain walls. Domains are areas of a number of crystals with the same polarization orientation, which are separated by domain walls. For tetragonal and orthorhombic phases, the spontaneous polarization $\boldsymbol{P_S}$ points in the [001] and [010]-direction, respectively. Thus, 6 equivalent orientations exist for the tetragonal and 12 for the orthorhombic phase. Depending on the crystal structure, these polarizations can orientate in different angles to each other:

- Tetragonal: 90 ° and 180 °
- Orthorhombic: 60°, 90 °, 120 ° and 180 °
- Rhombohedral: 71°, 109° and 180°

Domains can have the same angle differences to each other as polarizations. Figure 2.4 shows the domain structure of Li-doped NKN ceramics (LNKN), which possess a mix of orthorhombic and tetragonal structures. The picture shows 60°, 90°, 120° and 180° domain walls.

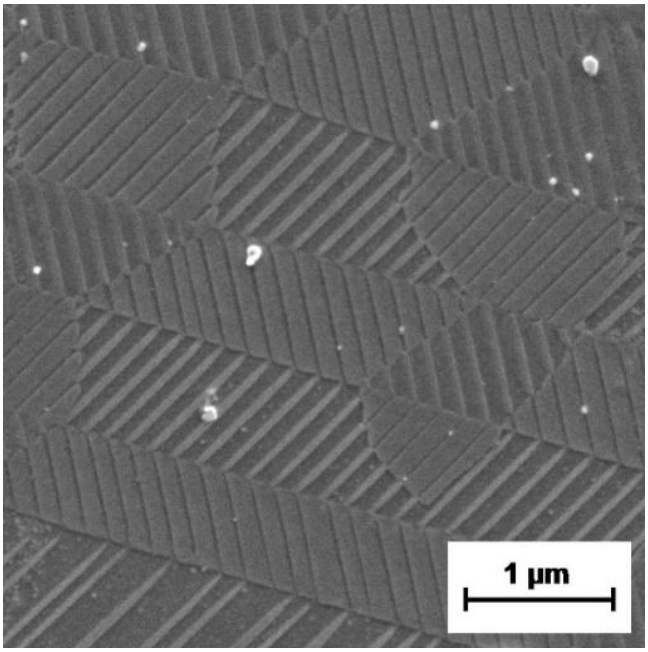

Figure 2.4: SEM image of the etched surface of LNKN with different domain walls.

Through the application of electric fields, domains as well as domain walls can be rearranged, which leads to the ferroelectric hysteresis loops ***P(E)*** and ***S(E)***. Figure 2.5 shows an example of a ***P(E)*** and ***S(E)*** loop. At first, the orientation of grains and domains are statistically distributed in a ferroelectric ceramic. Hence, the macroscopic polarization and strain is zero. An applied electric field increases the polarization and aligns the domains in the direction of the field. As the electric field increases, more and more domains will switch in the direction of the field and the polarization increases further. During this process, domains with the favorable orientation will grow at the expense of not favorable orientated domains. This behavior changes, if the majority of the domains are aligned in one direction and the material reaches a point of saturation P_S (A→B). With the decrease in field strength, the domains will start to switch back. However, the material will retain most of its polarization at zero field, called the remanent polarization P_r (B→C). Equally, the material will remain a certain macroscopic strain called the remanent strain S_r. If a negative electric field is applied, the polarization decreases and reaches zero at the coercive field E_C (C→D). If a negative electric field is applied even further, the domains will be aligned up to another saturation point (D→E). Removing the negative electric field resolves in a poled sample with negative polarization, but with positive remanent strain (F). For this reason, the ***S(E)***-loop is also called the butterfly loop with minima at the coercive fields $\pm E_C$.

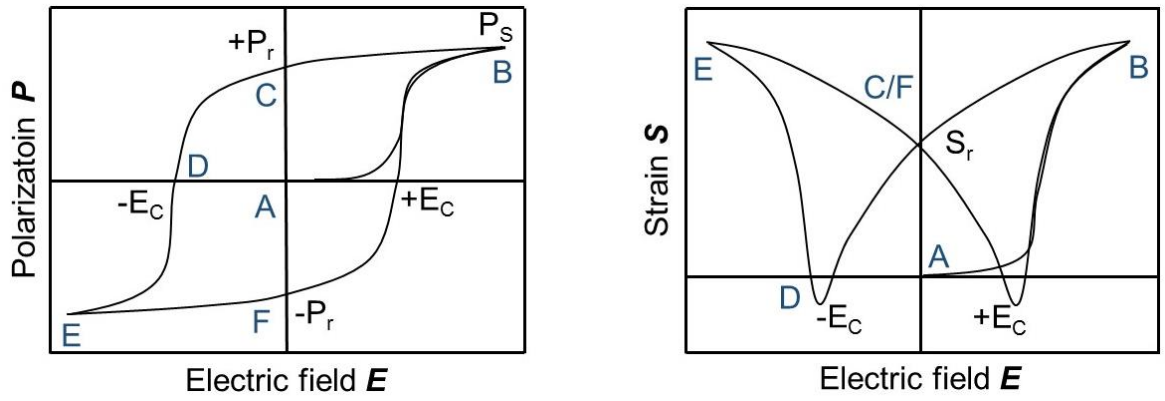

*Figure 2.5 Schematic representation of a **P(E)** and **S(E)**-loops of ferroelectric materials.*

During the alignment of the domains two different processes appear, which are called intrinsic and extrinsic contribution. The former one describes the volume change of the

unit cell if an electric field is applied. Domain switching of 180 ° and non-180 ° domains are called the extrinsic contribution.

2.2.1 Doping of NKN

Since Matthias et al., extensive research showed that the composition of $Na_xK_{1-x}NbO_3$ near x = 0.5 has superior piezoelectric and ferroelectric properties as well as a high Curie temperature.[9,29–32] For these reasons, the material is considered a leading lead-free candidate. In 2004, Saito et al. strengthened the idea of NKN ceramics as highly promising candidate by adding dopants such as Li, Ta, and Sb.[7] As a result, piezoelectric properties were improved significantly. Further studies, tried a large number of dopants on both A and B sites as well as different solid solutions in order to improve the piezoelectric properties of NKN[14,15,33–38]. Ahn et al. studied the dependence of the piezoelectric coefficient d_{33} from the transition temperature $T_{O\text{-}T}$[36]. It was shown, that the d_{33} value increases with decreasing transformation temperature. Moreover, the study showed that the Curie temperature T_C increases with increasing dopant, whereas the transformation temperature decreased.

Owing to the high cost of Ta and the toxicity of Sb, simple Li-doped NKN $[Li_x(Na_{0.5}K_{0.5})_{1-x}NbO_3]$ (LNKN) ceramics are still very popular. Guo et al. studied the effect of lithium doping on the piezoelectric properties of NKN by synthesizing the samples $Li_x(Na_{0.5}K_{0.5})_{(1-x)}NbO_3$ (LNKN), for x varying between 0.00 and 0.20.[14] They observed the presence of a morphotropic phase boundary (MPB) between the orthorhombic and tetragonal phase in the range $0.05 < x < 0.07$. Additional confirmation for a MPB was given by a sharp peak in piezoelectric properties (d_{33} = 235 pC/N, k_p = 44%) in this composition range. Du studied the effect of the poling temperature on the same lithium-doped MPB compositions (x = 0.05, 0.06, 0.07) and found that a significant improvement in piezoelectric properties can be achieved if poling is done at orthorhombic to tetragonal transition temperature $T_{O\text{-}T}$.[37]

In addition, Li improves sinter ability, which is a general problem for pure NKN ceramics. Note that only hot-pressed samples can be sufficiently densified.[29,39] Besides Li, MnO_2 increases the density of materials, because it inhibits grain growth during sintering. Different amounts of sintering additives CuO and MnO_2 were also tried to suppress the volatilization of Na_2O by decreasing the sintering temperature.[40] It was found that the

addition of 2 mol% CuO and 0.5 mol% MnO_2 reduces the sintering temperature to 950 °C and improves the piezoelectric properties with increased d_{33} value from 220 pC/N to 248 pC/N. Furthermore, hardening of ferroelectric properties can be detected owing to the formation of oxygen vacancies.[41)]

High temperature applications of piezoelectric materials require not only high Curie temperatures, but also good thermal stability between room and Curie temperature. NKN-based ceramics seems to be an excellent candidate for high temperature applications with T_C being close to 420 °C, but at the same time the presence of $T_{O\text{-}T}$ gives rise to discontinuity in piezoelectric properties. Peaks in the coupling coefficient k_p and permittivity ε can be seen clearly at the phase transition temperatures. To solve this problem, Ahn et al. studied the variation in k_p-temperature slopes in the solution of NKN with $BaTiO_3$. In comparison, the slopes of both materials are opposite to each other and thus the combination of these two compositions compensate the effect of fluctuations in piezoelectric properties with temperature[38)].

2.2.2 Point defects

Crystals contain two major categories of defects: “point” defects and “line” defects. The understanding of line defects, such as dislocations, is qualitative and thus this chapter focuses only on point defects occurring in ceramics.

Point defects occur when atoms are missing (= vacancies), occupy the interstices between normal sites (= interstitials) or are of foreign nature. The literature distinguishes between two major defects. Schottky defects, consist of unoccupied anion and cation sites, which are called vacancies. These vacancies are formed in stoichiometric units, to maintain an overall neutral charge in the ionic solid. These vacancies are free to move as their own entities. Frenkel defects are misplaced ions, which form when an atom or smaller ion (usually cation) leaves its place in the lattice. As a result, besides creating a vacancy, the misplaced ion also becomes an interstitial by lodging in a nearby location. Frenkel defects depend on the existence of empty spaces in a crystal lattice that can accommodate displaced ions. Especially for electroceramics, these defects are of crucial significance. Moreover, these effects are caused through the introduction of foreign ions and need to be studied. To exemplify this fact, we use MnO_2 doped NKN ceramics. In this case, Mn-ions will take

the place of the Nb-ion on the B site. Due to the fact that Mn possess a lower charge than Nb, Mn-ions are called acceptors and will have an effective negative charge. This negative charge can be compensated by a positively charged oxygen vacancy or an interstitial positively cation or hole. The chemical equation can be expressed as

$$Mn_2O_3 \leftrightarrow 2Mn'_{Nb} + 3O_O + V_O^{\cdot\cdot} \tag{2.5}$$

Kröger and Vink introduced a convenient notation for describing a defect and its effective electrical charge relative to the surrounding lattice. These effective charges are to be distinguished from the real charges on an ion. A defect that carries an effective single positive electronic charge bears a superscript dot, as shown by the oxygen vacancy $V_O^{\cdot\cdot}$. A defect with an effective negative charge bears a superscript prime, as shown by Mn'_{Nb}. Moreover, Mn'_{Nb} has a subscript which signalizes that Mn occupies the site of Nb.

2.3 Fatigue processes

Fatigue is a term most commonly associated with mechanical cyclic loading leading to failure of materials. In the case of fatigue due to electric cycling, the change in ferroelectric and piezoelectric properties as well as the mechanisms that lead to deteriorating properties are altogether different. Ferroelectric ceramics are subject to electrical, mechanical or electromechanical cycling over time. The mechanisms that lead to fatigue are mostly due to defects such as mobile vacancies, electrons or holes. Figure 2.6 shows the different effects of these defects.

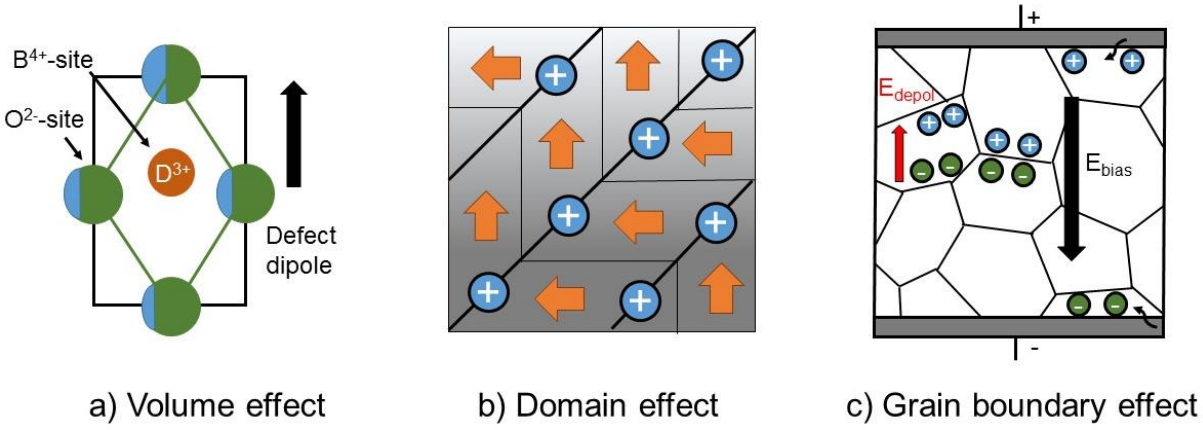

Figure 2.6: Schematics of the microstructural mechanisms for domain wall pinning according to scale.

Carl and Härdtl proposed three mechanisms to describe microscopically the defect-induced stabilization of the domain-wall structure in ferroelectrics[42]. In principle, they differ in the location of the defects that stabilize the domain configuration:

a) <u>Volume effect</u>

Especially in aged samples, point defects have the possibility to form defect dipoles. During the application of an electric field, defect dipole moments cannot be rotated in such a diffusionless process. Therefore, this unswitchable defect symmetry, and the associated defect dipole moment, provide a restoring force or a reverse internal field favoring a reverse domain switching when electric field is removed.[43,44]

b) Domain wall effect

Defects diffuse in the course of time into the domain walls and fix their position. The driving forces may be elastic (neutralization of internal stresses) or electric (compensation of electric charges, e.g. by valency changes of the foreign atoms).[45)]

c) Grain boundary effect

This effect describes the accumulation of space charges, such as ions, electrons or vacancies. Figure 2.6 c) shows there are 3 major processes that are included in the grain boundary effect. Two processes occur, when an electric field is applied onto the sample. Space carriers drift according to the field's direction and accumulate not only on the grain boundary (= first process), but also to interfaces between dissimilar phases, such as secondary phases or electrodes (= second process). The third process is caused by a depolarization field. For better understanding, this process is schematically represented in Figure 2.7 (a) – (c).

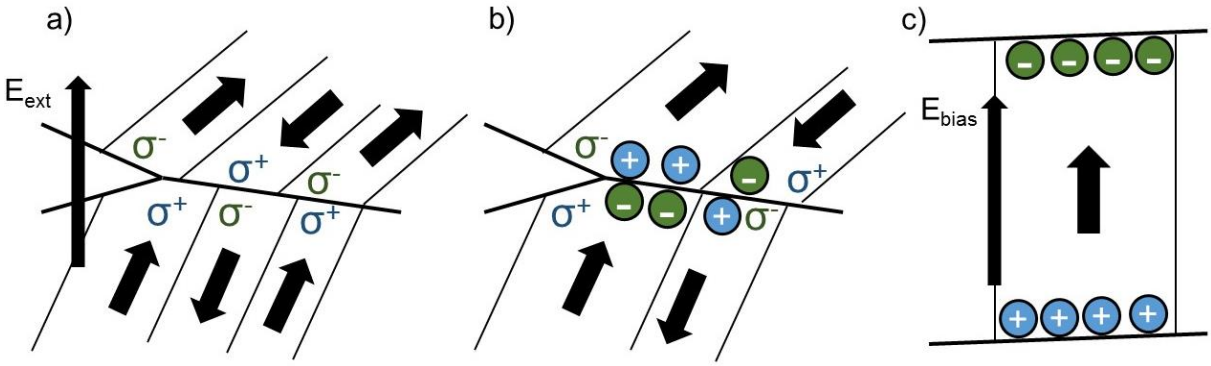

Figure 2.7: Schematics of space charge carrier accumulation near the grain boundary during fatigue process. Taken from [20)]

During the application of a DC or unipolar AC field, domains align according to the applied field. However, slight mismatches between domains near the grain boundary can lead to formation of charges $\boldsymbol{\sigma}$. In the literature, the electric field between the positive charge $\boldsymbol{\sigma^+}$ and the negative charge $\boldsymbol{\sigma^-}$ is referred to as local depolarizing field $\boldsymbol{E_{depol}}$ (Figure 2.7 a). The application of an electric field increases the size of domains in favorable direction and conclusively increases $\boldsymbol{E_{depol}}$. Mobile space charge carriers start drifting to compensate the depolarization field (Figure 2.7 b). This charge carrier

drift results in the internal bias field E_{bias}, which has the same direction as the external field E_{ext} (Figure 2.7 c).[20,46)]

However, besides these three microscopic mechanisms, macroscopic changes in form of mechanical degradation can occur. Mechanical degradation is divided in mechanical degradation in the sample and degradation in the interface between sample and electrode and the electrode itself. Figure 2.8 shows the first case, in which cracks form in the ceramics due to mismatches of domains in neighboring grains.

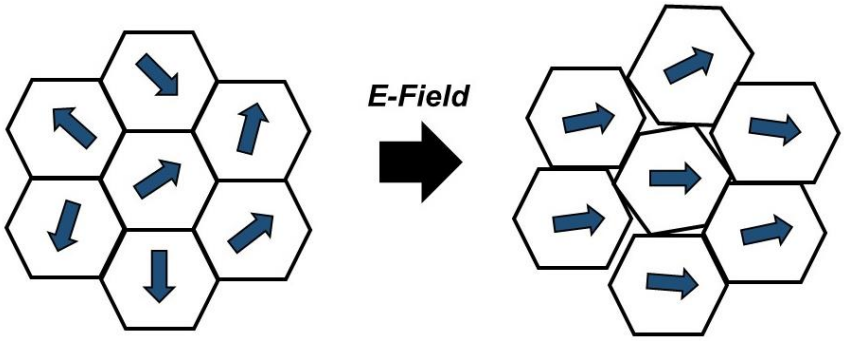

Figure 2.8: Schematic representation of micro crack formation due to mismatch in the domain structure between neighboring grains.

As mentioned before, the application of an electric field onto piezoelectric can strain the material. Depending on the orientation of the initial domains compared to the direction of the applied field, this strain can be of various dimensions. Thus, neighboring grains experience a different strain, which causes internal stresses at the grain boundary and at worst micro crack formation. The second case, describes the detachment of the electrode from the sample and the third case characterizes crack formation in the electrode itself. The latter processes are not critical to the mechanical strength of the ceramics. However, internal cracks as descript in the first case are especially severe for the mechanical strength of the material.

In the following chapters, the different fatigue mechanisms will be discussed on the basics of different fatigue conditions as well as NKN ceramics.

2.3.1. Fatigue under DC and unipolar AC field

The fatigue mechanisms between an applied DC and unipolar AC field do not differ much and will be discussed together for this reason. Piezoelectric samples are especially during polarization exposed to a DC field for a certain amount of time. In contrast, a unipolar AC field is applied during application. In both cases characteristic changes of the ferroelectric hysteresis occurs as shown in Figure 2.9.

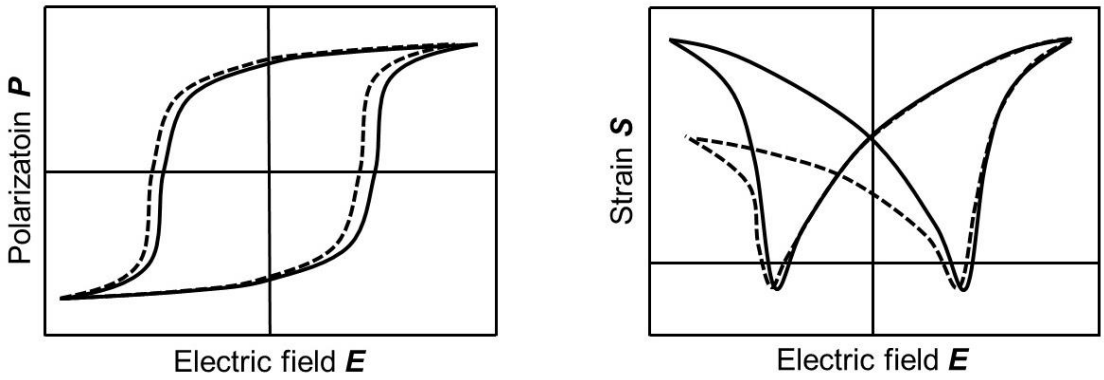

*Figure 2.9: **P(E)** and **S(E)** – hysteresis loops before (solid line) and after fatigue (dashed line) under DC and unipolar AC loading.*

In general, the fatigue effect is a pronounced asymmetry in ***S(E) –*** hysteresis loops, and a shift of ***P(E)*** – hysteresis loops. Usually, the switchable polarization and unipolar strain are hardly changed, but, for PZT, sinusoidal electric loadings up to 10^9 cycles were found to decrease the maximum unipolar strain and the piezoelectric coefficient d_{31}.[46–48] For non-commercial lead-free ceramics of the composition $0.94(B_{0.5}Na_{0.5})TiO_3 – 0.06BaTiO_3$ about 35% of the switchable polarization is lost after 10^4 cycles already.[49] In both lead-based and lead-free materials the cycling procedure leads to a larger maximum strain under electric fields with the same polarity. Besides a horizontal shift, ***P(E)*** hysteresis loops can also shift in vertical direction, which is called offset polarization. In general, all the measured effects are attributed to the depolarization field. Offset polarization was defined by Nuffer et a/.[50], and was explained by the Landau-Devonshire theory for electrostrictive materials, where strain is proportional to the square of total polarization. Technically, this is only fully applicable in cases of single domains near the Curie temperature. As modelled by Lupascu et al., a curve fit develops asymmetry only when an offset polarization

is applied and not when combinations of two volume sets of switchable and non-switchable polarizations within a material are considered for a given domain.[6] This indicates that an increasing polarization offset alone leads to the observed asymmetry.

Few scientific papers have addressed the fatigue behavior of NKN materials and the processes that lead to fatigue.[16–21] Yao et al. showed that, by modifying (K,Na,Li)(Nb,Ta)O_3 ceramics with $CaZrO_3$, nanodomains can form and increase temperature stability as well as resistance to unipolar fatigue.[21] The same results were obtained in a few other papers; whereby the authors doped NKN-LiSb with $CaZrO_3$[21] or Sm_2O_3[18]. Patterson et al. doped NKN materials with CuO and found a significant decrease in unipolar fatigue behavior. Acceptor doping increased the amount of oxygen vacancies and the possibility of accumulation on grain boundaries was enhanced.[19] The domain structure changes during the application of a unipolar field over a certain amount of cycles, as shown by Tsurekawa et al., who observed these changes via piezoresponse force microscopy (PFM).[16] Polarized MnO_2 doped LNKN6 samples were fatigued under a unipolar field of 30 V/mm at the resonance frequency of about 160 – 170 kHz. Piezoelectric properties, as well as the polarization of the domains decreased after 10^8 cycles. In addition, the domain width and length started to increase after the same number of cycles.

Besides electrical effects in the sample, cracks can also form during polarization.[51–56] Through the alignment of non-180° domains during polarization, stresses in between the different grains occur, which can lead to micro crack formation. Micro crack formation is dependent on the grain size[51,52,56], tetragonality of the unit cell[53], porosity[54] the electric field as well as time[55,56]. Moreover, during the application of a unipolar AC field, cracks can form and propagate. On PZT, many studies have shown that cracks form and propagate in piezoelectric ceramics under cyclic electric fields[57–63] in dependence of grain size[57], and temperature[48,60]. Jiang et al. tested lanthanum doped lead zirconate titanate (PLZT), which showed no crack formation for samples with small grain sizes (= 5µm), but formed cracks at larger grain sizes (≥ 10 µm). The significance of fatigue, indicated by the beginning and magnitude of the decreasing electrical properties, increased with increasing grain size. The major cause for this behavior was the incompatible large deformations, resulting from the anisotropic piezoelectric coefficients.

A theoretical approach was derived from the results, and a formula for a critical grain size l_c was introduced.[57)]

$$l_c = \frac{2g_b}{E_V} = \frac{2g_b}{3Y \cdot [(d_{33} - d_{31})E]^2} \tag{2.6}$$

where E_V is the anisotropic volume energy, Y the Young's modulus, d_{33} and d_{31} the piezoelectric coefficients, E the applied electric field and g_b the fracture surface energy of the grain boundary. For PLZT the critical grain size was estimated to be 7 µm, which was consistent with the obtained experimental results. Cracks are in so far critical to the electric properties, as they represent an area with a very low permittivity ε compared to the rest of the sample. Thus, the electric field in the sample is inhomogeneous and mostly concentrated at the crack tip. Schneider et al. showed a decrease in the electric potential over the crack length by means of an atomic force microscopy (AFM) in Kelvin probe mode (KPM). The highest loss of the electric potential was measured at the half length of the crack.[64)] Furthermore, with increasing crack opening the loss in potential increases. Therefore, if the crack reaches a certain length and width, the electric field in certain areas will be significantly smaller than the applied field. As a consequence, domain switching is inhibited in these areas and the macroscopic coercive field is increased.

Wang et al. observed the influence of temperature on the fatigue behavior of PZT. It was shown that fatigue tests performed under electric field levels below the coercive field value, no mechanical degradation occurs. On the other hand, larger electric field values cause degradation, which is an increasing function with increasing electric field strength or decreasing temperature. Again, the major reason for degradation was attributed the electrically induced stresses caused by internal anomalies. Hill et al., found the same relationship between temperature and fatigue behavior. The formed cracks are mostly find close to the electrode.[48,57)]

By applying a small mechanical uniaxial stress onto piezoelectric materials, the strain per applied electric field unit increases. Kerkamm et al. showed that the piezoelectric coefficient d_{33} as well as strain S had maximum values if a preload of about 35 – 40 MPa was applied on soft-doped PZT multilayer actuators. Compared to no preload, the strain and piezoelectric coefficient showed increased values by about 6 % and 16 % respectively.[65)] For fatigue under unipolar AC-fields, Wang et al. observed the

influence of a mechanical preload. It was shown that with increasing pressure, fatigue occurred at a decreasing number of cycles.[66)]

2.3.2. Fatigue under bipolar AC field

Bipolar AC fields and the related fatigue mechanisms are most important for ferroelectric applications. The consequential characteristic changes of the ferroelectric hysteresis are shown in Figure 2.10.

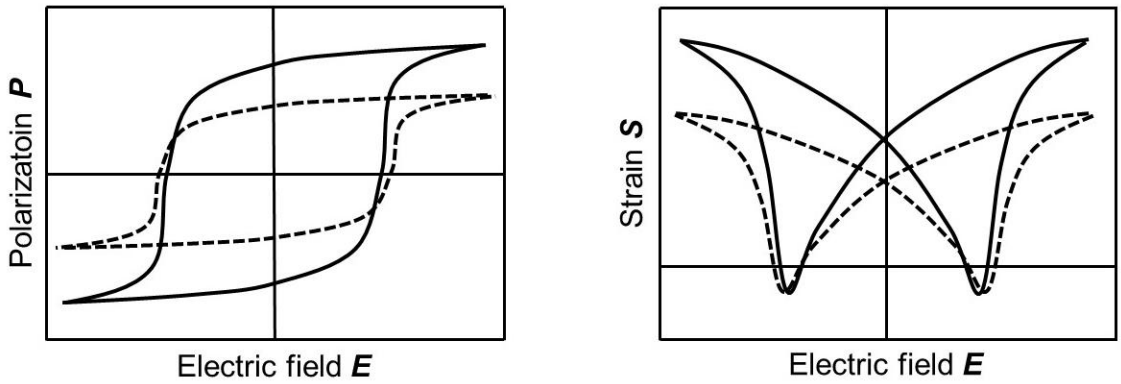

*Figure 2.10: **P(E)** and **S(E)** – hysteresis loops before (solid line) and after fatigue (dashed line) under bipolar AC loading.*

In bipolar fatigue, the permanent effects are tied to reduction in strain and switchable polarization simultaneously, implying a reduction of the mobility of 90° domain walls. In contrast to unipolar and DC loading the degradation of remanent large and small signal values is severe if the applied electric field is bipolar. The ***P(E)*** hysteresis loops in PZT show strong degradation of maximum and remnant polarization. Asymmetric changes can appear, but are not as significant as in DC or unipolar fatigue. Lupascu proposed that piezoelectric fatigue could be explained by a common mechanism that reduces switchable polarization and strain simultaneously by focusing in a mechanism that could possibly suppress 90° domain switching. These obstacles would inherently need to grow during the fatigue cycling process in order to make sense. After 2 E_C bipolar fatigue of PZT samples, the application of an increased electric field of 4 E_C lead to an restored hysteresis loops with approximately full values of remanent and maximum polarization.[67)] Fatigue-lowered maximum and remanent polarization values are surpassed by the application of higher fields but the

decreases are not removed permanently. The origin of bipolar fatigue still remains controversial to this day, and many models have been proposed. The most widely observed mechanism is domain wall pinning, which is shown in Figure 2.6 (b).[68] In 2015, Guo et al. showed for the first time the in-situ observation of domains during bipolar fatigue in $[(Bi_{0.5}Na_{0.5})_{0.95}Ba_{0.05}]_{0.98}La_{0.02}TiO_3$.[69] These observations complemented the domain wall pinning effect, by verifying a novel fatigue mechanism of domain fragmentation. TEM images showed, that with increasing bipolar cycles the domains fragmented into smaller nanodomains and the grain showed an increased domain wall density. Furthermore, the domain walls were gradually pinned and became less mobile during cycling. In general, oxygen vacancies are widely considered to lead to domain wall pinning. However, most of the time various fatigue mechanism occur at the same time. Verdier et al. observed commercial PZT, which decreased its remanent polarization and coercive field.[70] Impedance measurements as well as ***P(E)*** hysteresis loops were recovered after the sample were annealed at 600 °C. They explained this fact through the growth of a non-ferroelectric layer or passive layer. The passive layer occurs due to an increasing amount of defects or doping due to inclusion of material from the electrode.[71] Lee et al. also reported the existence of a passive layer in Pt/PZT/Pt thin films after fatigue.[72] By measuring the permittivity close to the electrode, they showed that the permittivity at the PZT/PT interface decreased with increasing fatigue. The dielectric permittivity of the bulk PZT film remained constant.

Micro crack formation is more pronounced in bipolar fatigue than in DC or unipolar loading. The reason is the mostly due to the bipolar electric field, which concludes in a large strain difference between negative and positive polarized materials. Micro crack formation during long-term cyclic loading is a major mechanism of fatigue generation and is mostly induced by bipolar electric fields with amplitudes high enough to induce polarization switching.[63] It was reported that severe crack growth mostly originates near the electrode[73], but pre-existing micro cracks and pores[74], secondary phases[60], as well as the relief of residual stresses[75] can serve as additional sources for crack growth. Luo et al. observed the bipolar fatigue behavior for $0.94(B_{0.5}Na_{0.5})TiO_3 – 0.06BaTiO_3$ under 6 kV/mm (≈2 E_c).[49] A decrease of polarization and strain, was observed, and most of the degradation occurred within 10^4 cycles. Micro cracks were found near the electrode, which contributed significantly to the degradation of the ferroelectric properties and to the increase of the coercive field. Overall, the remanent

polarization decreased by 50 % and the coercive field increased for 22 % after 10^6 cycles. Balke et al. showed via PFM measurements the difference in the thickness profile of PZT samples with different attached electrodes after bipolar fatigue.[76)] PZT with Pt electrodes showed micro cracks underneath the electrode, which affect the internal electric field distribution. Micro cracks effectively screen the applied electric field and protect the remainder of the sample bulk from further domain wall pinning. In contrast, PZT samples with Ag electrodes showed fatigue in the entire volume of the sample. Nevertheless, ***P(E)*** hysteresis loops showed a stronger degradation of the remanent polarization in the samples with Pt electrodes, which should imply that micro cracks have a more severe effect on the fatigue behavior.

By combining mechanical preloads during fatigue under bipolar AC-fields, increased fatigue resistivity was observed by Yang et al.[77)]. As mentioned above piezoelectric degradation in the fatigue process is due to domain pinning caused by point defects. Mechanical loads up to 60 MPa suppress non-180° domain switching and micro cracking in multilayered PZT.

2.4 Fracture mechanics

The most serious cause for an instrument or material to fail is by fracture. It is therefore important to analyze and understand the causes for fracture to occur, in order to build a safe and reliable machine. A difficulty hereby is the estimation when and how a certain component will break. Fracture depends on the environmental conditions, the form of the component and type of loading, such as static, cyclic and creeping stress. In reality, most of the time a mix in between these types and conditions are present. Fracture mechanics is dealing with the problem of describing the lifetime or load-bearing under different conditions.

Fracture is defined as the breaking of atomic bonds and the resulting macroscopic separation of the solid material. This can lead to the formation and propagation of cracks on a micro- as well as macroscopic level. The loss of stability is reached after cracks reach a critical length and can be of brittle and ductile nature. Ceramics show generally brittle fracture, which means that no deformation or small deformation in close vicinity at the crack tip occurs. Two characteristic fracture surfaces occur in brittle materials, which are shown in Figure 2.11.

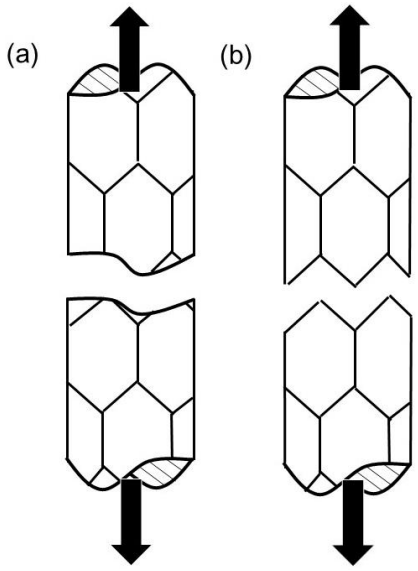

Figure 2.11: Schematic representation of transgranular (a) and intergranular fracture (b)

Each material has a theoretical cohesion strength, which depends on the binding forces between the atoms and temperature. This theoretical value is never reached,

due to defects in the material which enhance crack propagation. Crack propagation can either be stable (energy input) or instable (energy output). For instable crack propagation, Griffith assumed that the saved elastic strain energy decreased significantly more than the surface energy to form an increased crack surface. If both energies are in an equilibrium, one can estimate the critical stress σ_C necessary for instable crack propagation.

$$\sigma_c = \sqrt{\frac{2g_{pc}Y}{\pi a}} \tag{2.7}$$

where g_{pc} is the fracture surface energy, Y the Young's modulus and a the crack length. One problem with the criteria of Griffith is the fact that it is difficult to compare samples to each other. For this reason the stress intensity factor K was introduced to determine and compare the fracture toughness of different brittle materials. K describes the strength of the tension field at the crack tip and can be estimated by following equation.

$$K = \sigma\sqrt{(\pi a)}f\left(\frac{a}{W}\right) \tag{2.8}$$

where σ is the stress, a the crack length and $f\left(\frac{a}{W}\right)$ a dimensionless correction parameter, which describes the relationship between crack configuration and sample dimensions. Instable crack propagation only occurs if K reaches a critical value, called fracture toughness K_C. The fracture toughness is determined during experiments and can be used to compare different materials. Furthermore, K_C gives also information which stress condition had an effect on the crack. There are three testable modes, which are shown in Figure 2.12.

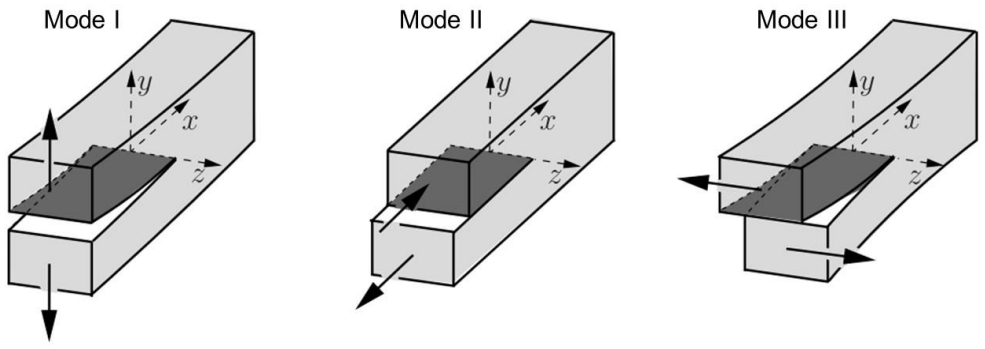

Figure 2.12: Crack opening modes taken from [78)]

For applying K_C on a component, it is important to determine to most critical mode for the material. In case of ceramic materials, tensile stress is the most critical and thus, usually K_{IC} is used to evaluate the fracture toughness.

Different methods can be applied to observe and determine the stress intensity factor K. Three of the most commonly used methods are the single edge V notched beam (SEVNB) method, the compact tension (CT) method and the Vickers indentation fracture (VIF) method. Compared to the other methods the VIF is easy to perform and repeatable on multiple samples. No specific sample dimensions or preparation is needed, which is usually a problem for ceramic samples. Furthermore, the VIF method gives information about anisotropic crack propagation in the material. For these reasons, we decided to use the VIF method for testing the fracture toughness in this work.

2.4.1 Vickers indentation fracture (VIF) method

The VIF method was developed to estimate the fracture toughness of ceramic materials by measuring the lengths of cracks caused from Vickers indents. The schematic concept of Vickers indentation and conclusive crack propagation are schematically represented in Figure 2.13.

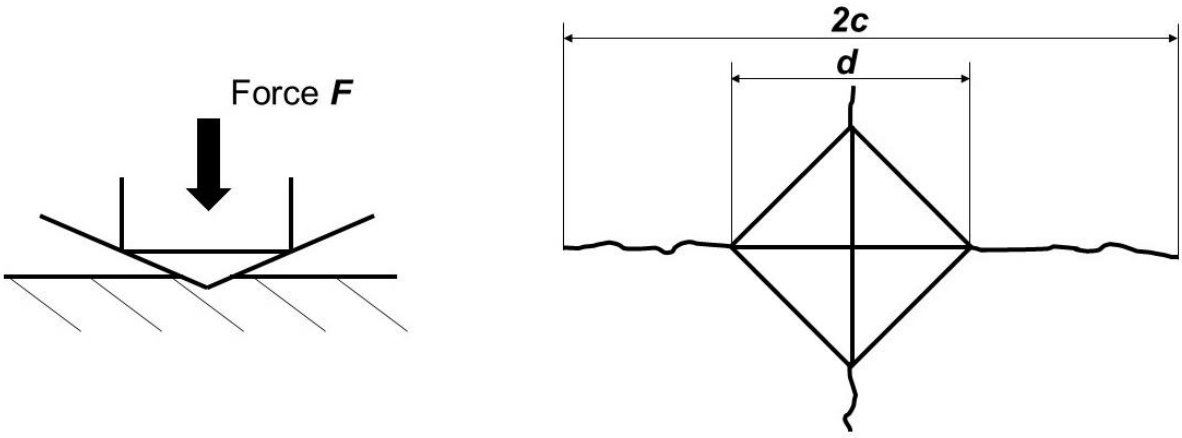

Figure 2.13: Schematic representation of Vickers indentation and the formed dimensions of cracks.

The method has recently received much attention for measuring the fracture toughness of biomaterials. Many different equations exist in the literature for determining the

fracture toughness. In our case, the VIF fracture toughness K_C is calculated using the equation within the guidelines of the Japanese Standard Association, which was derived from the original concept by Lawn et al. [79,80]:

$$H = \frac{F \cdot \sin(\alpha/2)}{d^2} \tag{2.9}$$

$$K_C = 0.018 \sqrt{\left(\frac{Y}{H}\right)} \frac{F}{c^{3/2}} \tag{2.10}$$

where F is the applied load, Y is Young's modulus, H is the hardness, d the diagonal length of the indented pyramid base and c is the length of the surface trace of the half penny crack measured from the center of the indent. The value α is the angle of the Vickers indentation pyramid, which is 136°. In addition Park and Sun developed a concept to estimate K_{IC} for ferroelectric materials[81,82].

$$K_{IC} = 0.0113 \frac{d\sqrt{F \cdot Y}}{c^{3/2}} \tag{2.11}$$

where c is the length of the surface trace of the half penny crack measured from the center of the indent, d the diagonal length of the indented pyramid base, F the applied indentation load, and Y the Young's modulus.

The fracture toughness measured via indentation tests has the advantage of being the easiest method for ceramic samples. However, the measured value K_C can only be compared to fracture toughness values estimated with the same procedure. Furthermore, internal stresses in the sample are likely to distort the actual value. Therefore, the measured values via VIF have to be critically examined. Both equations (2.10) and (2.11) were used to determine the respective values.

3 Methods used for sample preparation and characterization

In this chapter the experimental procedures as well as the material which were used throughout this work are described in general.

3.1 Ceramics processing and firing

All ceramic samples were synthesized by a mixed-oxide route. The starting powders K_2CO_3, Na_2CO_3, Nb_2O_5 (99.9%) and Li_2CO_3 (99.8%) were dried separately at 120 °C for at least 4 h to remove moisture. The MnO_2 powder was stored at room temperature. After weighing and mixing the powders prior to the respective composition, they were milled with ZrO_2 - balls for 16 h. Afterwards, calcination was carried out at 910 °C for 10 h and a second milling step for 16 h was performed. Before using the finished powders, they were stored at 120 °C for 4 h more. At first, the calcined powders were pressed uniaxially at 10 MPa for 0.5 min and at 75 MPa for 1 min. The green bodies, were then inserted in a PU tube in which a vacuum was generated. The samples were than cold isostatically pressed at 300 MPa for 2 min into the required shape. The pressure was slowly decreased with a rate of 20 MPa/min. All samples were sintered at $\boldsymbol{T}$ = 1082 °C for 0.5 h with a heating and cooling rate of 3 °C/min. Surfaces were coated with silver and annealed at 700 °C for 5 min. Subsequently, the samples were poled in silicon oil under an applied electrical field of $\boldsymbol{E}$ = 3 kV/mm for 30 min. The poling temperature depended on the composition, but all samples were cooled down to 40 °C with the electric field still switched on.

3.2 Fatigue experiments

For the fatigue tests, a custom-made experimental setup was used, which is shown in Figure 3.1.

Figure 3.1: Experimental set-up for fatigue experiments.

A silicone oil bath was attached onto a compression testing machine (Universal testing machine EZ-LX, Shimadzu, Kyoto, Japan) to apply a certain force to a sample. The maximum force that can be applied is 2 kN. Furthermore, the silicone oil bath prevents arcing and enables the control of temperature during the experiments. By using a multifunction generator (Multifunction Synthesizer WF 1943A, NF Corporation, Yokohama, Japan) and an amplifier (Model 610D, TRek Inc, New York, USA), the samples could be electrically fatigued. The set-up allows for a maximum applied Voltage of 10 kV and maximum frequencies up to 4 kHz.

3.2 Impedance method

In order to measure piezoelectric coefficients, resonant and antiresonant frequency measurements were used. Hereby, the natural resonances of the sample are stimulated by a small electrical AC field. In the area of the mechanical resonance frequency, the impedance is minimized, which is called resonance frequency $\boldsymbol{f_r}$. On the

other hand, for applied frequencies above this value, the mechanical branch becomes inductive and reaches a maximum in impedance, which is called antiresonance frequency f_a. Piezoelectric ceramics show numerous resonance and antiresonance frequencies distributed over the spectrum, due to coupling of the direct and inverse piezoelectric effect. Depending on the sample dimensions, different values can be calculated. For example, a thin rectangular sample is suitable to measure the coupling factor k_{31}, the elastic compliance s_{11} and the piezoelectric coefficient d_{31}. A rectangular rod is used to measure k_{33}, s_{33} and d_{33}. Figure 3.2 shows an example for a measured impedance spectrum with f_r and f_a.

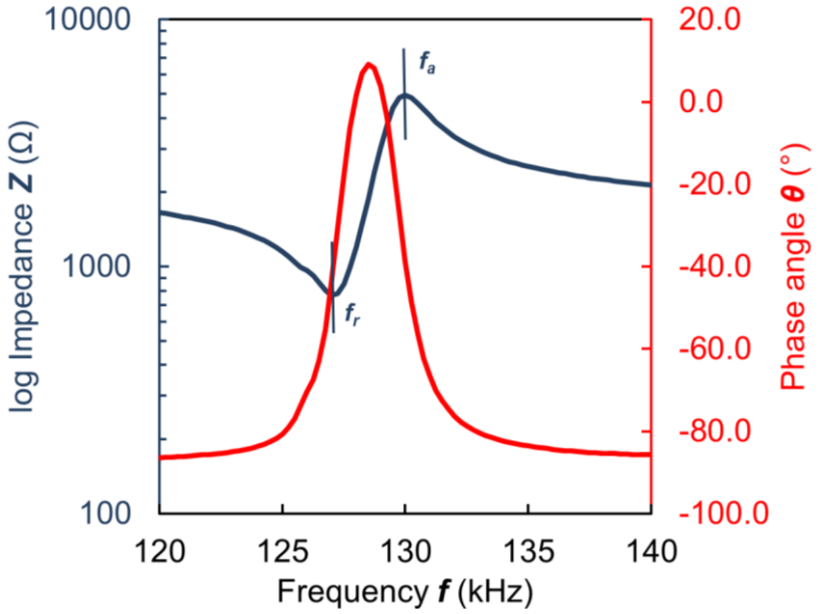

Figure 3.2: Example for an impedance spectrum of a LNKN sample near a fundamental resonance.

Besides the impedance spectrum, also the phase angle θ is obtained via the measurement. This value gives a good overview of how well the sample is polarized. The higher the maximum phase angle, the more domains are aligned in the same direction. With the values from the impedance measurement, the elastic compliance can be calculated with the following equation:

$$2f_r \cdot l = \frac{1}{\sqrt{\rho \cdot s_{ij}^E}}, \tag{3.1}$$

where $\boldsymbol{\rho}$ is the density of the sample and $\boldsymbol{l}$ is the controlling dimension. In case of a thin rectangular samples, the value correspond to the length of the sample and the measured elastic compliance would be $\boldsymbol{s_{11}^E}$. In a ceramic rod, where the electrodes are far apart, the controlling dimension would be the height and $\boldsymbol{s_{33}^E}$ can be obtained. The coupling factor $\boldsymbol{k_{31}}$ can be evaluated using equation

$$k_{31}^2 = \frac{\frac{\pi}{2}\left(\frac{f_a}{f_r}\right)\tan\left[\frac{\pi}{2}\left(\frac{f_a - f_r}{fr}\right)\right]}{1 + \frac{\pi}{2}\left(\frac{f_a}{f_r}\right)\tan\left[\frac{\pi}{2}\left(\frac{f_a - f_r}{fr}\right)\right]} \tag{3.2}$$

and for $\boldsymbol{k_{33}}$

$$k_{33}^2 = \frac{\pi}{2}\left(\frac{f_a}{f_r}\right)\tan\left[\frac{\pi}{2}\left(\frac{f_a - f_r}{fr}\right)\right] \tag{3.3}$$

The piezoelectric coefficient can then be calculated, using the evaluated values of the coupling factors and elastic compliances.

$$d_{31}^2 = k_{31}^2 s_{11} \varepsilon_{33}, \tag{3.4}$$

$$d_{33}^2 = k_{33}^2 s_{33} \varepsilon_{33}, \tag{3.5}$$

where $\boldsymbol{\varepsilon_{33}}$ is the permittivity at a frequency $\boldsymbol{f}$ = 1 kHz, which can be obtained by dielectric measurements.

3.3 X-ray Diffraction (XRD)

The physical background is based on the diffraction of X-rays at the structured lattices of the material. Diffraction occurs, if the distance of the lattice is in the same dimension as the wavelength of the ray. The wavelength of X-rays is about 1 pm to 10 nm and is therefore useful for the interaction with the lattice. The x-rays are diffracted at the electron cloud and the out coming waves interfere with each other. The interference can be of constructive or destructive nature, depending on the incidence angle and distance between the atoms. If constructive interference occurs, a peak can be seen in the measured spectrum. X-ray diffraction data were obtained by an X-ray diffractometer (X'Pert Pro, PANalytical, Almelo, Netherlands) with a Bragg-Brentano configuration. Hereby, the sample is put on one axis of the diffractometer and tilted by

an angle ***θ*** while a detector rotates around it on an arm at ***2θ***. The radiation source is of CuKα1, with a wavelength of 1.54 Å.

XRD was primarily used to evaluate the domain configuration and the phase composition. The former was obtained by measuring the domain switching fraction η_{hkl}. Depending on the crystal structure, the equation changes. For example, η_{002} for tetragonal and η_{200} for orthorhombic need to be determined with following equations:

$$\eta_{002} = \frac{R_{002}}{R_{002} + 2R_{200}} - \frac{1}{3} \tag{3.6}$$

$$\eta_{200} = \frac{R_{200}}{R_{200} + R_{020}} - \frac{1}{2} \tag{3.7}$$

where R_{hkl} is the ratio of the intensity of the peak hkl to the intensity of an unpoled sample. To determine the peak intensity, a Lorentzian fit was carried out. The idea is that the volume of domains with a certain crystallographic pole is a fraction of the total volume of all possible domain states. Furthermore, it is known that the intensity of a peak is proportional to the volume of the diffracting material.[27,28)]

Figure 3.3 shows how the intensity changes independently of the sample's composition from the unpoled to the poled state.

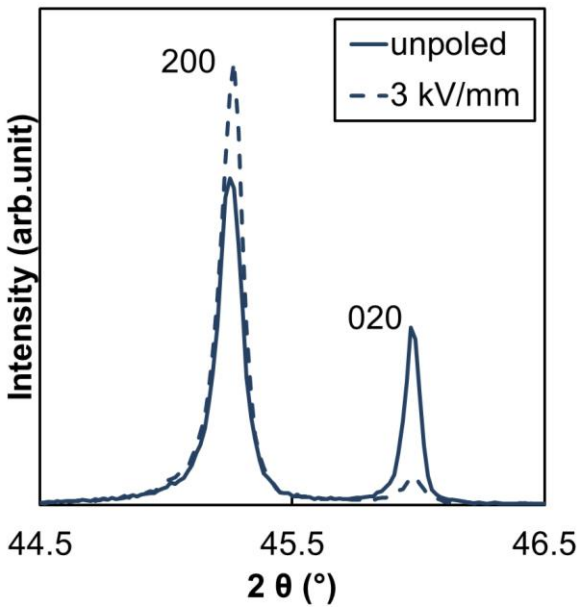

Figure 3.3: X-ray diffraction of NKN between 2Θ = 44.5 – 46.5, with peak intensity shifts of 200 and 020 before and after poling.

The intensity of the 020 peak decreases after poling, whereas the intensity of the 200 peak increases. In this case, domain reorientation occurred in the material during poling, where the crystal structure acquired a preferential orientation of 200.

By comparing the peak intensities, it is further possible to determine electric-field-induced structural phase transformation. Hereby, the peak intensities from 44° to 47° were used to evaluate the percentage of the tetragonal phase F_T with the following equations[83]:

$$I_{Small-Bragg} = {}^{1}/_{3}\, S_{IT} + {}^{2}/_{3}\, S_{IO} \tag{3.8}$$

$$I_{Large-Bragg} = {}^{2}/_{3}\, S_{IT} + {}^{1}/_{3}\, S_{IO} \tag{3.9}$$

$$F_T = \frac{S_{IT}}{S_{IT} + S_{IO}} \tag{3.10}$$

With $I_{Small\text{-}Bragg}$ and $I_{Large\text{-}Bragg}$ as the intensities of the peaks with small and large Bragg angles and S_{IT} and S_{IO} as the sums of the peak intensities for tetragonal and orthorhombic phases, respectively. However, by using only equations (3.6) to (3.10), it is not possible to distinguish if changes in the peak intensities were due to a phase transformation, or further polarization of the sample, as both mechanisms can change the intensity of the peaks. For this reason, phase composition was evaluated using additional Rietveld refinements. Hugo Rietveld devised this technique to characterize crystalline materials. Many aspects of the material's structure is dependent on the height, width and position of the measured peaks. The Rietveld method uses a least squares approach to refine a theoretical line profile until it matches the measured profile. In our case, we refined the collected data using the software FULLPROF.[84] X-ray diffraction also allows the evaluation of the lattice parameter of the perovskite structure. By looking at different Rietveld refinements in the literature, better reliability factors can be achieved by describing the perovskite structure of the two phase system (orthorhombic/tetragonal) as a monoclinic one, as shown by Hatano et al.[85]. To determine the lattice parameters, the same assumption was made.

The first equation describes the calculation of the distance ***d*** between the lattice in the monoclinic system:

$$\frac{1}{d^2} = \frac{1}{\sin^2\beta}\left\{\frac{h^2}{a^2} + \frac{k^2\sin^2\beta}{b^2} + \frac{l^2}{c^2} - \frac{2hl\cos\beta}{ac}\right\} \tag{3.11}$$

Whereas, ***a***, ***b*** and ***c*** are the lattice parameters and ***β*** is the angle between the ***a*** and ***c*** axis. The miller indices ***h, k*** and ***l***, which we focused on are 020, 200, 002, 222, $22\bar{2}$ and the corresponding distances ***d(200)***, ***d(002)***, ***d(222)***, ***d(22$\bar{2}$)*** are described in the following equations:

$$\frac{1}{d(020)} = \frac{2}{b} \tag{3.12}$$

$$\frac{1}{d(200)} = \frac{2}{a \cdot \sin\beta} \tag{3.13}$$

$$\frac{1}{d(002)} = \frac{2}{c \cdot \sin\beta} \tag{3.14}$$

$$\frac{1}{d(222)^2} - \frac{1}{d(22\bar{2})^2} = \frac{16\cos\beta}{ac \cdot \sin^2\beta} \tag{3.15}$$

In equation (3.15) it is further possible to replace the product with equation (3.13) and (3.14), which results in:

$$\frac{1}{d(222)^2} - \frac{1}{d(22\bar{2})^2} = \frac{4\cos\beta}{d(200) \cdot d(002)} \tag{3.16}$$

By converting the equations, it is possible to describe the lattice parameters and angle with the following equations:

$$\cos\beta = \frac{d(200)\cdot d(002)}{4}\left\{\frac{1}{d(222)^2} - \frac{1}{d(22\bar{2})^2}\right\} \tag{3.17}$$

$$a = \frac{2\cdot d(200)}{\sin\beta} \tag{3.18}$$

$$c = \frac{2\cdot d(002)}{\sin\beta} \tag{3.19}$$

$$b = 2\cdot d(020) \tag{3.20}$$

The lattice parameters were used to measure the tetragonality ***c/a***, which is an important indicator for micro crack formation during the application of an electric field.

3.4 Mechanical properties

If mechanical forces are applied onto a material, a reversible deformation takes place, which is called elasticity. At higher forces a permanent deformation can occur, but has only a minor importance for ceramics at lower temperatures. More important is the fact that ceramics will break if a sufficient force is applied to them. The resistance against forces, which can break the material, is called the mechanical strength. Ceramic materials show an elastic behavior to an outside applied force. In the linear case of tensile stress, the elastic deformation is proportional to the applied force and can be described by the Hooke's law:

$$\sigma = SY \tag{3.21}$$

with $\boldsymbol{\sigma}$ as the tensile stress, ***S*** the strain and ***Y*** the Young's modulus. Different methods exist to estimate the Young's modulus. In our case, the Young's modulus as well as other material constants were evaluated via the ultrasonic wave velocity method. Ultrasonic waves belong to mechanical oscillations, which means that they transport mechanical energy in the material. To simplify matters, forces in between the lattice elements can be pictured as springs, which represent the elastic restoring force. The oscillation propagates from atom to atom and has wave like character. There are many different possibilities how ultrasonic waves can propagate in a material. The two most

important ways are the longitudinal waves and transverse waves. In longitudinal waves, oscillation and propagation have the same direction whereas in transverse waves the oscillation is perpendicular to the propagation. The latter can only propagate in media hat can transfer shear forces. For this reason, these waves cannot propagate in liquids and gases and a special couple medium with high viscosity is needed to transfer the ultrasonic waves from the generator into the material. By using an ultrasonic pulser-receiver (Ultrasonic pulser-receiver 5072PR, Olympus Corporation, Tokyo, Japan) and oscilloscope (Digital oscilloscope DS-8822P, Iwatsu Electric Corporation, Tokyo, Japan), the longitudinal v_L and transverse v_S acoustic wave velocities were measured to determine the Young's modulus Y_{33} and Poisson's ratio σ. The equations are:

$$Y_{33} = 3\rho v_S^2 \frac{v_L^2 - \frac{4}{3}v_S^2}{v_L^2 - v_S^2}, \tag{3.22}$$

$$\sigma = \frac{1}{2}\left(1 - \frac{1}{(v_L/v_S)^2 - 1}\right), \tag{3.23}$$

where ρ is the density of the sample. The subscript of the Young's modulus describes the relation between the electrical and mechanical quantities. For example, if an electric field is applied in thickness direction (3) the strain would be measured in the same direction (3).

If the stress that is applied to the material reaches a certain value, cracks form and propagate which lead to breaking of the material or at least influence the mechanical strength. This stress can be determined experimentally or theoretically, whereby the real values are considerably lower than the theoretical ones. Moreover, the experimentally determined values are not constant and depend on the size of the measured sample as well as the microstructure. Particularly the porosity has a significant impact on the mechanical strength. There are several measuring methods to determine the mechanical strength of ceramic materials. With regards to effort and accuracy, bending tests are given the preference. In our case 3-point bending tests were used to estimate the flexural strength.

Figure 3.4 shows the experimental set-up of the 3-point bending tests. The instrument used was an Instron 5582 (Instron, Boston, USA) with a load cell capacity of 5 kN.

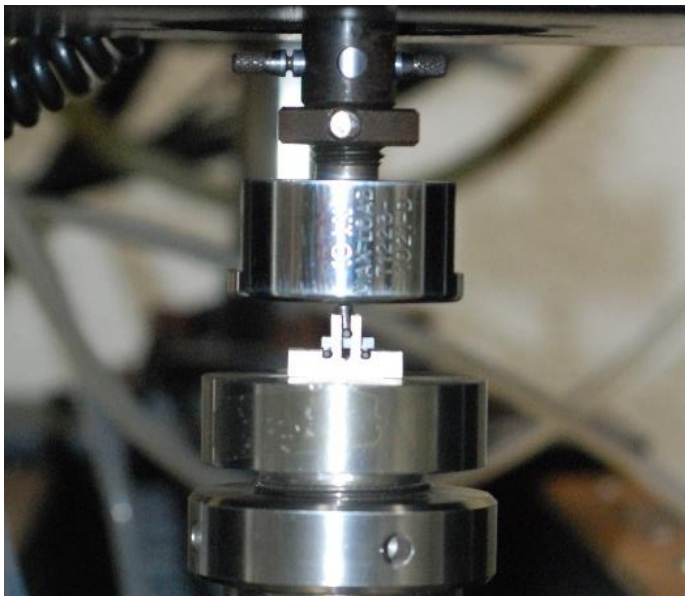

Figure 3.4: Experimental set-up of 3-point bending tests, with LNKN6 sample.

For all experiments, the samples had a length ***l*** of 10 mm and a width ***w*** of 2 mm. The thickness ***t*** changes, depending on the experiment and is stated in more detail in the experimental procedure section of the respective chapters. The flexural strength was estimated using equation:

$$\sigma_f = \frac{3Fl_S}{2wt^3} \tag{3.24}$$

where, ***F*** is the force when the samples breaks and l_S the support span of the experimental set-up, which was 8 mm in our case. The analysis of bending tests usually takes place with statistical methods. Especially meaningful is the Weibull-statistic, which can be described with the following equation:

$$F = exp\left[-V \cdot \left(\frac{\sigma}{\sigma_0}\right)\right]^m \tag{3.25}$$

Hereby is ***F*** the probability of the material to fail, ***V*** the volume of the sample, σ the measured bending strength, σ_0 and ***m*** are considered material constants. σ_0 describes the bending strength at which 62.5% of the samples will probably fail. The Weibull

modulus ***m*** describes the dispersion range of the measured strengths. The higher this value the lower the dispersion and the more accurate the results. For ceramic materials, this value usually ranges from 5 to 20. To solve equation (3.25) it is necessary to transform it into equation:

$$lnln\left(\frac{1}{F}\right) = \ln(\sigma) - mln(\sigma_0) \tag{3.26}$$

The measured values from the bending tests, will then be sorted according size and lnln[1/(1-F)] is plotted against ln(σ). ***F*** for the ***i***-th value is for ***N*** in total measured values F = *1-i/(N+1)*. An example for a Weibull statistic is shown in Figure 3.5:

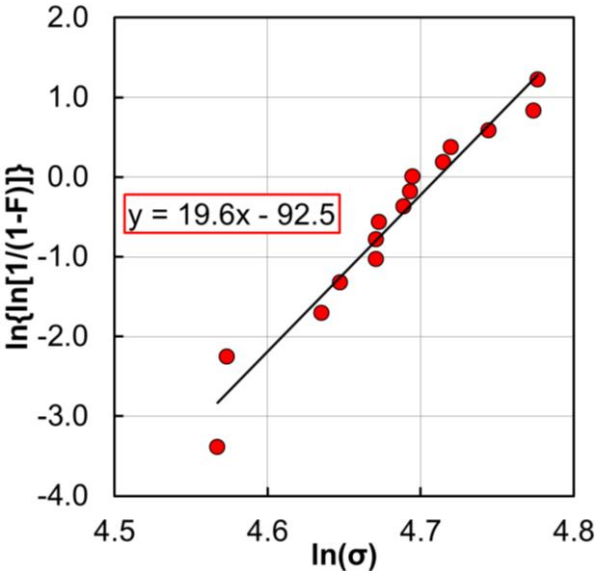

Figure 3.5: Weibull statistic of $Li_{0.06}(Na_{0.47}K_{0.47})NbO_3$.

The slope of the function represents the Weibull modulus ***m*** and $\boldsymbol{\sigma_0}$ can be calculated by equating the linear function to zero.

4 Electromechanical fatigue process under DC field

In this chapter, we discuss the influence of the polarization field and domain structure on the piezoelectric and mechanical properties of NKN-based ceramics. For this purpose, differently poled $Li_x(Na_{0.5}K_{0.5})_{1-x}NbO_3$ ceramics have been observed by means of 3-point bending tests. Best results were achieved with $Li_{0.02}Na_{0.49}K_{0.49}NbO_3$, with a flexural strength of 115 MPa in unpoled state. This value was maximized at a 90° domain switching fraction $\boldsymbol{\eta}$ of about 20% to 134 MPa. Other compositions showed similar behavior, which led to the idea that domain switching can be used to enhance the mechanical properties of NKN ceramics. Internal stresses induced via domain reorientation might be the cause of this phenomenon and was examined in this study.

4.1 Experimental procedure

Ceramic samples with the composition of $Li_x(Na_{0.5}K_{0.5})_{1-x}NbO_3$ ($\boldsymbol{x}$ = 0 – 0.06) were synthesized by a mixed-oxide route, which is described in chapter 3.2. Disks (diameter $\boldsymbol{d}$ = 10 mm; height $\boldsymbol{h}$ = 1 mm) and bars (area $\boldsymbol{A}$ = 6 x 6 mm^2; length $\boldsymbol{l}$ = 10 mm) were manufactured for acoustic wave-velocity tests and for bending and indentation tests, respectively. The rectangular shapes for the bending tests were then cut, ground, and polished into bars of different dimensions (area $\boldsymbol{A}$ = 2 x 2 mm^2; length $\boldsymbol{l}$ = 10 mm). The bulk densities were determined via the Archimedes method. For the poling treatment, all the samples were sputtered with gold electrodes and afterwards poled in silicon oil under applied electrical fields $\boldsymbol{E}$ of 1, 2, and 3 kV/mm for 30 min. The temperature $\boldsymbol{T}$ is 75 °C for the compositions with x ranging from 0.02 to 0.06 and 150 °C for the pure NKN ($\boldsymbol{x}$ = 0) samples. By using different temperatures on the different compositions, the respective maximum piezoelectric properties could be obtained. The piezoelectric constant $\boldsymbol{d_{33}}$ was estimated using a Berlincourt-type quasistatic meter (Quasistatic meter ZJ-6B, H.C. Materials Corporation, Bolingbrook, USA) at 110 Hz. The electromechanical coupling coefficients $\boldsymbol{k_p}$ and $\boldsymbol{k_{31}}$ were determined by resonance and antiresonance methods based on IEEE standards using an impedance analyzer (Impedance analyzer 4294A, Agilent Technologies, Santa Clara, USA). Before the samples were used for mechanical tests, gold electrodes were removed via polishing. Afterwards, by using equations (3.22) and (3.23), the Young's modulus $\boldsymbol{Y_{33}}$ and Poisson's ratio $\boldsymbol{\sigma}$ were determined.

3-point bending tests were carried out using an Instron 5582 (Instron, Boston, USA) with a load cell capacity of 5 kN and a crosshead speed of 0.1 mm/min. To quantify the average bending strength and reliability of each composition, the flexural strength data for each material is fit to a Weibull distribution, which is described in chapter 3.4. 15 samples were tested for each composition and poling condition, including the unpoled case as well.

For the indentation tests, the samples had a dimension of 6 x 6 x 4 mm^3 and were poled under 3 kV/cm, Au electrodes were removed by polishing, and all the surfaces were indented with a 196 N load. The resulting intendations were photographed by laser microscopy, and the dimensions measured to estimate Vickers hardness with equation (2.9). The cracks emanating from the corners of the Vickers indents were used to estimate the fracture toughness $\boldsymbol{K_{IC}}$ and $\boldsymbol{K_C}$, equations (2.10) and (2.11).

The domain orientation was characterized by X-ray diffractometry (XRD) using equations (3.6) and (3.7). The total scanning range was from 20 ° to 105 ° with a step width of 0.017°.

4.2 Results and Discussion

The samples were observed via SEM and representative microstructures for the materials are shown in Figure 4.1 (a) - (d).

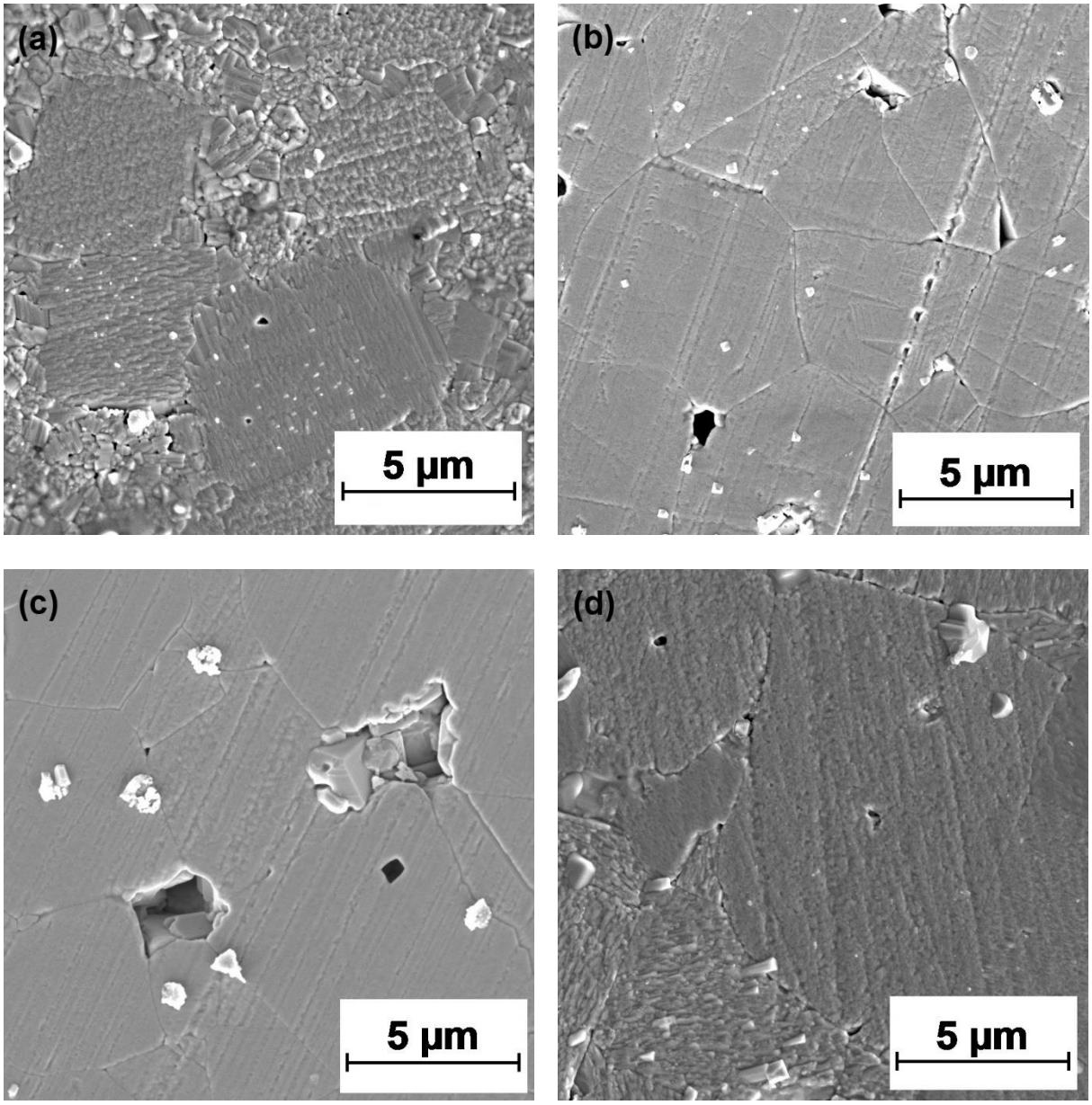

Figure 4.1: SEM images of the microstructure of NKN (a), LNKN2 (b), LNKN4 (c) and LNKN6 (d).

From the SEM images, the influence of Lithium can be obtained. NKN showed larger grains surrounded by smaller grains. At a Li-content of x = 0.02 these grains seem to have disappeared and grew even further with increasing Lithium. The different sizes

that were displayed in these images were measured and summarized. The basic physical characteristics of the compositions are given in Table 4-1.

Table 4-1: Physical characteristics of the modified NKN compositions.

Composition	**Abbreviation**	**Grain size *l* (µm)**	**Density *ρ***	
			Absolute(g/cm³)	**Relative (%)**
$Na_{0.5}K_{0.5}NbO_3$	**NKN**	1.1 – 8.4	4,21 ± 0,04	94
$Li_{0.02}Na_{0.49}K_{0.49}NbO_3$	**LNKN2**	3.2 – 8.1	4,30 ± 0,05	95.5
$Li_{0.04}Na_{0.48}K_{0.48}NbO_3$	**LNKN4**	7.7 ± 1.5	4,26 ± 0,04	95
$Li_{0.06}Na_{0.47}K_{0.47}NbO_3$	**LNKN6**	8.6 ± 1.4	4,29 ± 0,05	95.5

Based on the composition, the bulk densities of the samples varied between 4.21 and 4.30 g/cm. The microstructural developments in different compositions were affected by the amount of Li. For the pure NKN and LNKN2 samples, a bimodal grain size distribution was observed. Both compositions showed coarse grains of about 8 µm size. Smaller grains had average sizes of 1.1 µm for NKN and 3.4 µm for LNKN2. At 4 mol% Li, the grain size distribution became unimodal. LNKN4 and LNKN6 had large grains with an average size of 7.7 ± 1.5 and 8.6 ± 1.4 µm, respectively. The obtained grain growth could be attributed to the improved sinter ability owing to the presence of Li.[15)]

Figure 4.2 shows the XRD patterns for each composition.

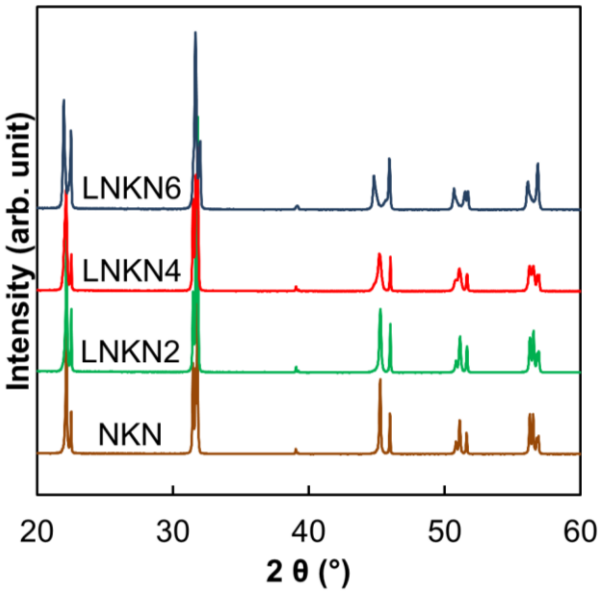

Figure 4.2: X-ray diffraction (XRD) patterns of modified NKN samples.

Noticeable are the peaks at about 2θ ≈ 45°, which are usually used as evidence of the phase transition in the literature. More data on the phase transition behavior of Li-modified NKN ceramics were collected from peaks at higher angles (Figure 4.3).[86)]

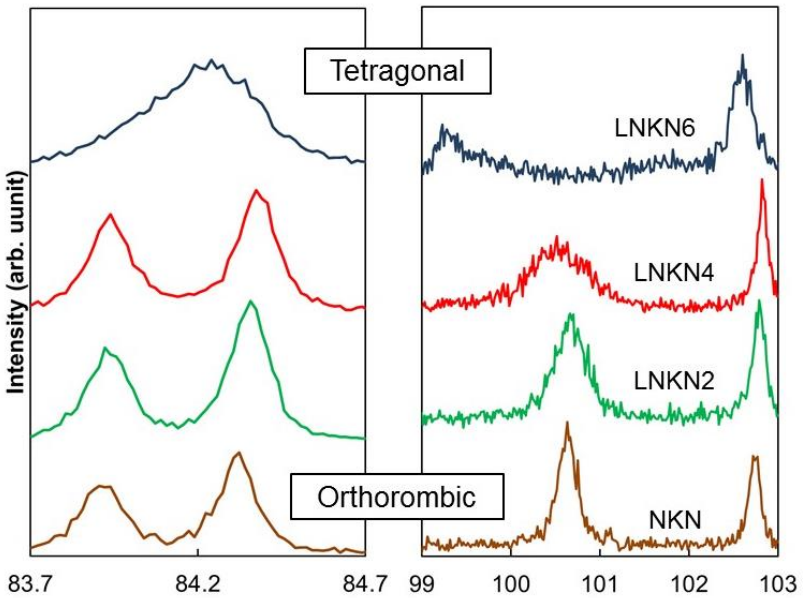

Figure 4.3: X-ray diffraction (XRD) patterns of modified NKN samples at higher angles.

Analysis of the patterns shown in Figure 4.3 revealed that two peaks occurred at approximately 84° for NKN ceramics with Li content ranging from 0 to 4 mol%. These peaks tend to merge into one single peak with increasing Li content. This was shown in the XRD pattern of LNKN6, which indicated a predominant tetragonal phase. Further investigations of the peaks between 99 to 103° showed that the intensity of the peak near 100° decreased with increasing amount of Li. This implied a change in the lattice parameters from orthorhombic to tetragonal. Nevertheless, the peak of LNKN6 is widely broadened, representing the coexistence of orthorhombic and tetragonal phases.

By comparing the peak intensities from 44° to 47°, it is further possible to determine the percentage of the tetragonal phase F_T, which were calculated with equations (3.8) to (3.10). In addition, these results were compared to values extracted from Rietveld refinements. Unpoled samples were observed, due to the fact that poling changes the peak intensities and alters the results. Figure 4.4 (a) and (b) show the results for different Lithium content.

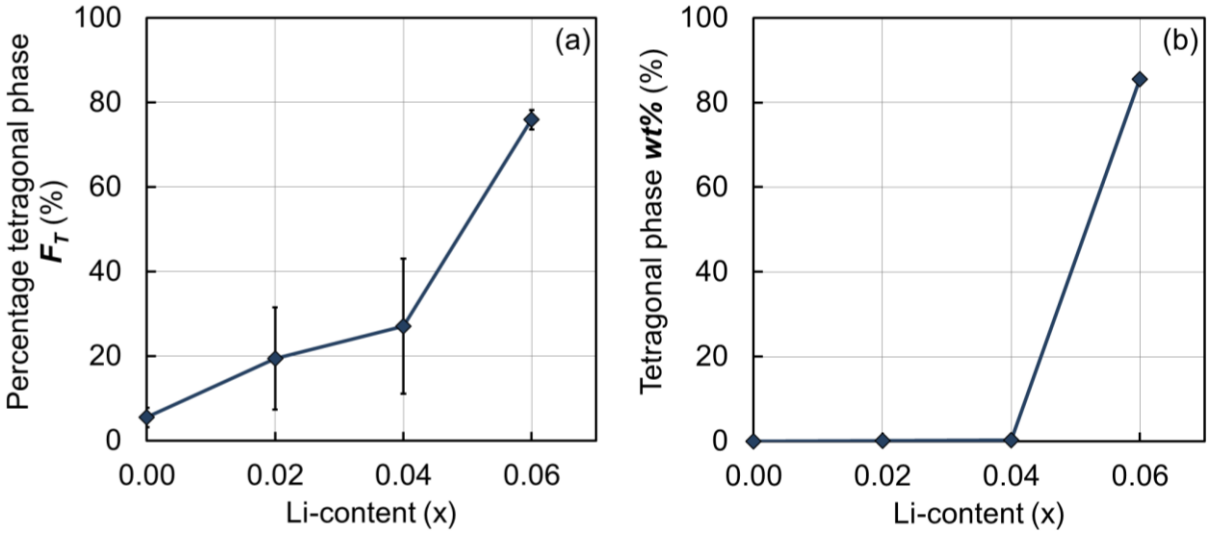

*Figure 4.4: Percentage of tetragonal phase F_T (a) and weight percentage **wt%** (b) of unpoled NKN-based samples as a function of different Lithium content.*

In both cases it was shown that the percentage of tetragonal phase increased with increasing Lithium content. NKN had a F_T of about 0%, whereas at = 0.02 – 0.04 a tetragonal percentage of about 20 % seemed to be included in the material. At x > 0.04 a significant increase to about 75 % of the tetragonal phase is observed. In contrast,

almost no tetragonal phase was observed for x = 0 – 0.04 after Rietveld refinement (Fig. 4.4 (b)). At Lithium contents of 0.06 the weight percentage ***wt%*** was about 85 %. Taken the predominant tetragonal characteristics at higher angles of the XRD patterns into account, as well as the higher estimated percentage of tetragonal phase, samples with a Li content of 0.06 were treated as tetragonal materials for the additional analysis of the domain orientation.

Figure 4.5 shows the results of the 90° domain switching fraction. As for compositions with Li content ranging from 0 to 4 mol%, equation (3.6) was used for calculating the fraction. Owing to the tetragonal characteristics, the 90° domain switching fraction of LNKN6 was calculated using equation (3.7). The graphs revealed an increasing fraction with increasing poling field. Hence, at high poling fields ***E***, the volume of aligned domains in the poling direction increased.

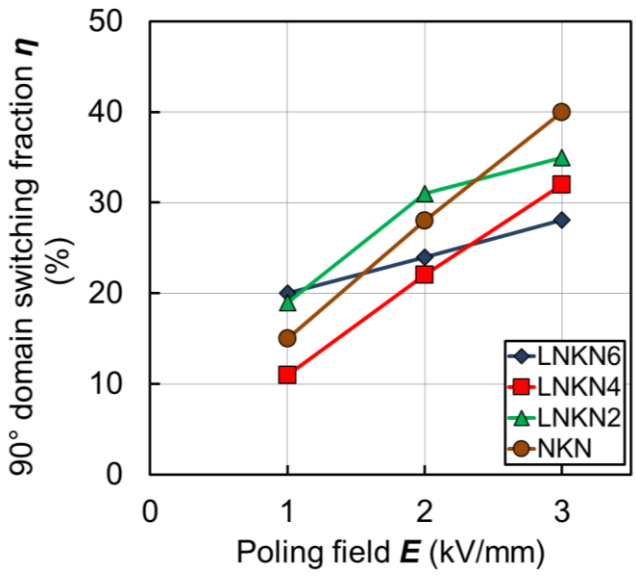

*Figure 4.5: Variation of the 90° domain switching fraction **η** of different compositions as a function of the applied field **E**.*

As mentioned earlier, the 90° domain switching fraction **η** depends on the present phase. X-ray observations showed that, except for NKN, no pure orthorhombic or tetragonal phase existed in the compositions used. Thus, the calculated results could not be treated as absolute values and a direct relationship between the domain structure and amount of Li was not found. However, the results were used as relative values in the discussion to predict certain tendencies.

A similar behavior was seen for the piezoelectric properties, represented by the coupling factors k_{31} and k_p. This is illustrated in Figure 4.6 (a) and (b). Both values showed a positive progress with increasing poling fields. Furthermore, the piezoelectric properties were also enhanced with an increasing amount of Li, which is consistent with other published data.[14,15)]

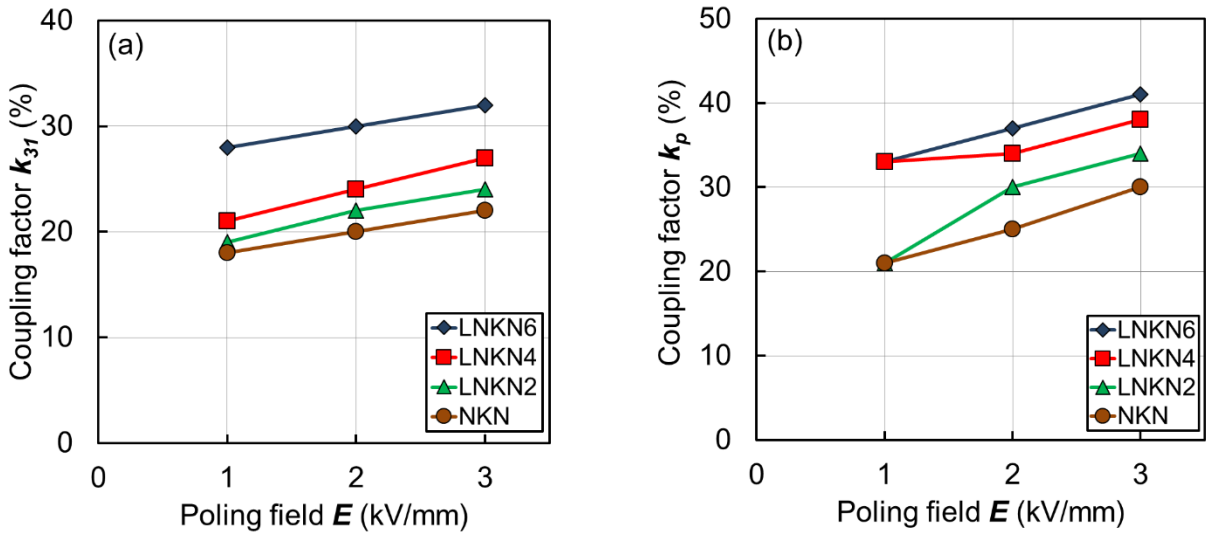

*Figure 4.6: Influence of poling field **E** on the coupling factor k_{31} (a) and k_p (b) for different compositions.*

As in the figures shown above, the 90° domain switching fraction and coupling factors linearly increased with increasing poling field. This indicates that aligned domains in the poling direction contribute to the piezoelectric properties. However, the properties of piezoelectric materials consist of intrinsic and extrinsic contributions, which could not be distinguished via XRD or resonance and antiresonance methods. If an electric field or mechanical load is applied to a sample, domain reorientation takes place and ions are initially oriented to the polarization direction. As a consequence, the lattice is distorted microscopically and the sample is strained. This case is referred to as the intrinsic or volume contribution and is followed by a 90° domain wall rearrangement. This domain wall motion also contributes to the total strain of the sample and is called extrinsic contribution. Owing to the fact that the strain consists of two contributions of varying values, the piezoelectric and mechanical properties are also affected.[87,88)]

Kobayashi et al. showed that, for NKN ceramics, the extrinsic contribution changes with varying Li content. A significantly higher contribution can be found for LNKN

ceramics with a Li content of 3 – 4 mol%. As for compositions with 0 – 2 mol%, the value was larger than that of samples with 6 – 8 mol%.[88)]

Figure 4.7 (a) and (b) show respectively Young's modulus Y_{33} and Poisson's ratio σ as functions of poling field. The values were calculated using equations (3.22) and (3.23). Additional data from Table 4-1 was required to analyze Y_{33}.

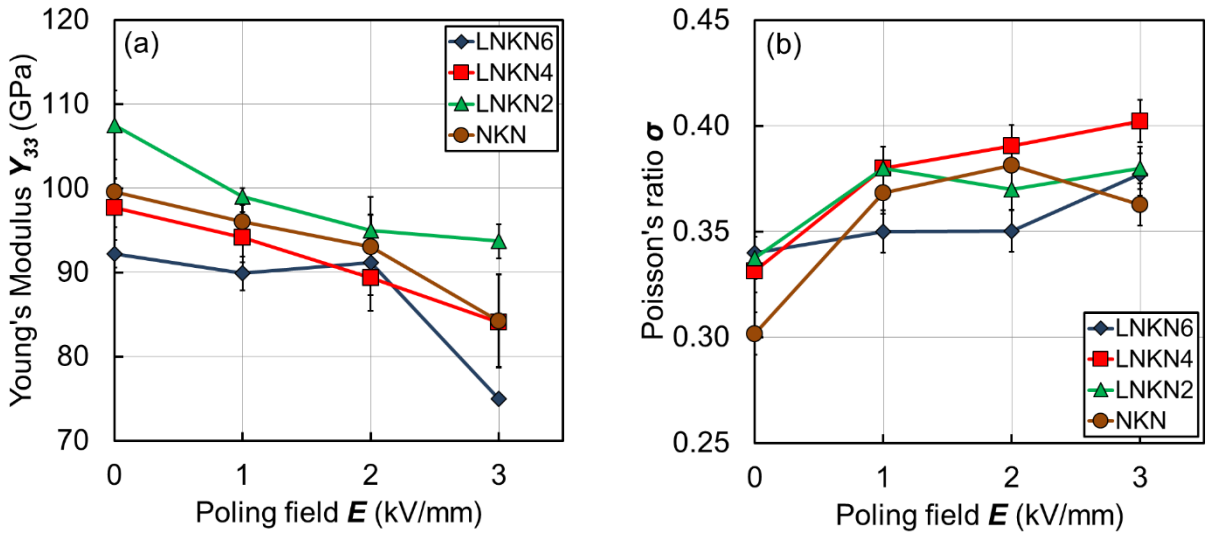

Figure 4.7: Young's modulus Y_{33} (a) and Poisson's ratio σ (b) for different compositions and poling fields E

With equation (3.22), it can be concluded that Y_{33} is proportional to the density of the material. However, NKN with the lowest density had a higher value than LNKN6. Hence, it can be suggested that Li had an effect on the elastic properties of the material and lowered Y_{33}. Additionally, Y_{33} decreased whereas σ increased with increasing poling field. One possible solution was found by Ogawa et al., who suspected domain switching as the cause of changes at different poling fields. Furthermore, a minimum in Y_{33} due to domain clamping was observed by this group. They showed further that materials with a low coupling factor k_p have relatively low Y_{33} and high σ.[89)] In the case of NKN ceramics, the domain clamping effect was not observed. However, even though the other results were not confirmed absolutely, the same tendency was examined. In particular, if the elastic constants and coupling factors of NKN and LNKN6 are compared, this tendency can be observed. As for pure NKN, the elastic modulus was determined to be 99.6 ± 1.6 GPa, which is slightly lower than the literature data of 104 GPa.[29,30)] The difference was associated with different density values.

Figure 4.8 (a) and (b) show flexural strength σ_0 and Weibull modulus m for each composition as function of poling field, respectively. In the unpoled state, LNKN2 showed the highest mechanical strength σ_0 of 115 MPa.

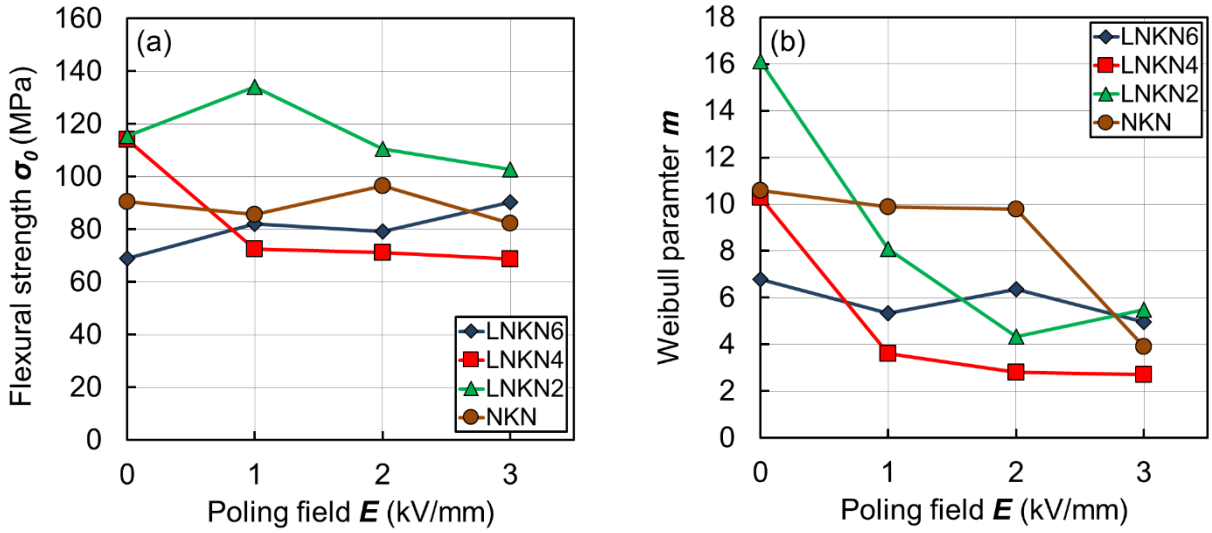

*Figure 4.8: Dependence of flexural strength σ_0 (a) and Weibull parameter **m** (b) on the poling field **E** for different compositions.*

For further information, the results of the bending tests were compared with the physical characteristics shown in Table 4-1. Due to the complex electromechanical coupling relationships and the non-linearity associated with the domain wall motion in piezoelectric ceramics, the mechanical strength depends on many factors, such as loading type and direction[90,91], microstructure[92–94], phase composition[95,96] and polarization state[90,97]. Loading type and direction were equal for each sample, so the main focus was on the latter factors. Knudsen describes how the porosity and grain size of a material affect the mechanical strength of brittle materials. The porosity has a more significant effect on the material strength than the grain size.[94] Although the microstructure and density did not differ substantially from each composition, the variation in the density had to be taken into account. The influence of the Li content on the flexural strength was found by comparing NKN with LNKN6. Even with less density, NKN showed higher mechanical strength, which indicated that the toughness of alkali niobates decreased with increasing Li content. This solution was consistent with the results obtained from the ultrasonic wave velocity experiments. As mentioned before, phase composition as well as polarization state are also factors that need to be taken

into account. Figure 4.9 (a) and (b) shows the influence of the phase composition on the flexural strength of unpoled samples, as well as the percentage difference in flexural strength between the unpoled and poled samples as a function of 90° domain switching fraction $\boldsymbol{\eta}$.

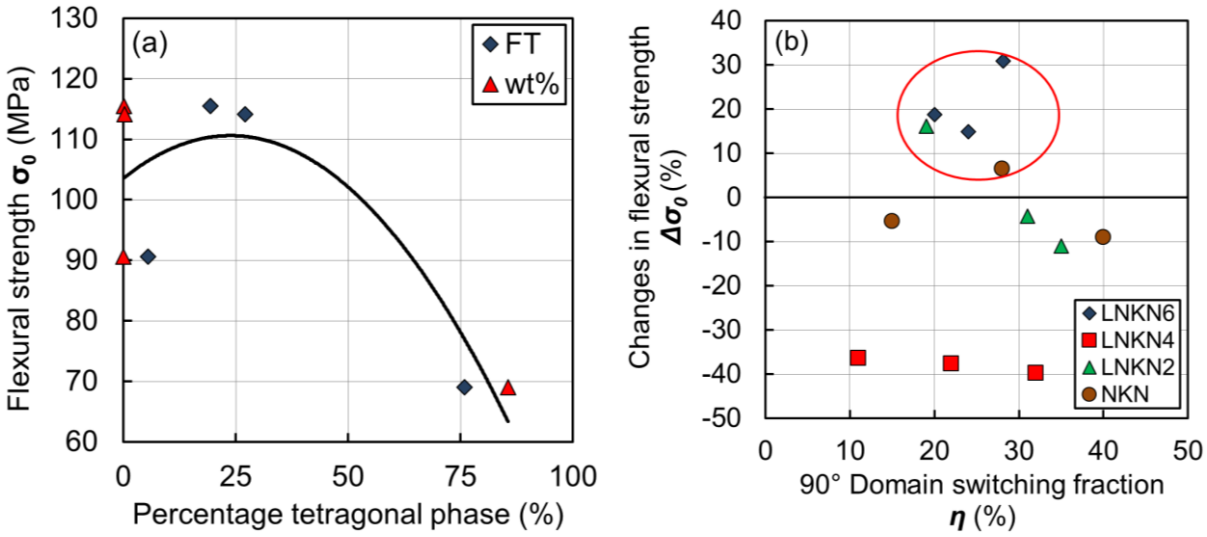

Figure 4.9: Flexural strength as function of the tetragonal phase (a) and change of the flexural strength plotted against the 90° domain switching fraction $\boldsymbol{\eta}$ (b).

Figure 4.9 (a) shows the flexural strength as a function of the percentage of the tetragonal phase. With increasing tetragonal phase the flexural strength decreased. The few results suggest a maximum flexural strength at about 25 %. However, the densities of the different materials is not considered in the results. Due to a lower density in NKN compared to the other compositions, it is possible that the actual flexural strength of NKN is significantly higher. It can therefore be concluded that the orthorhombic phase showed improved mechanical properties over the tetragonal phase in case of alkali niobate based ceramics.

By poling the samples, the flexural strength was improved for most of the compositions at a certain poling field. However, the flexural strength decreased for each material, except for LNKN6, after exceeding a certain value. In the case of LNKN4, $\boldsymbol{\sigma_0}$ decreased with increasing poling field. More detailed information was obtained from comparing the domain switching fraction and the changing flexural strength. As a result, some samples were improved by about 10 to 30% with increasing poling field and domain switching fraction. Notably, this enhancement was found in most of the materials for a

domain fraction of about 20 – 30%. In particular, LNKN4 showed no improvement of the mechanical properties and only a negative progress with increasing poling field. The Weibull factor ***m***, had a minimum scatter of strength (maximum value of ***m***) for all samples at ***E*** = 0 kV/mm. Poled samples showed a decreasing tendency of ***m*** with increasing poling field.

Several publications discussed the effect of the electric field on the mechanical properties of PZT. Crack formation and propagation in bulk samples can appear during the poling process.[51–55] Larger grain sizes, increased porosities and piezoelectric coefficients usually lead to a higher probability of cracking. From these points alone, no significant difference should be noted between LNKN4 and LNKN6. As mentioned earlier, two processes take place during poling, which both lead to mechanical tensions in neighboring grains and consequential crack formation. However, studies show that these tensions are also able to increase the mechanical properties.[26,82,98–100] These tensions can be the result of the earlier mentioned intrinsic and extrinsic contributions. Fu and Zhang discussed in their work how both contributions change the flexural strength of the material.[26] They derived a nonlinear relationship between the electric force on a domain wall and the applied electric field based on the domain wall kinetic model. Due to the nonlinear behavior, domain wall displacement and internal stress are also in a nonlinear relationship with the applied electric field. Hence, the internal stress field may assist or resist the applied mechanical load to fracture samples. Whereas the strength of the internal field is dependent on the ratio between intrinsic and extrinsic contribution. A higher extrinsic contribution leads to higher internal stresses. As mentioned earlier, this contribution has a maximum at approximately 4 mol% Li. Hence, the increased domain wall motion led to a higher internal stress field, a lower fracture strength in LNKN4 and consequential crack formation. However, for the other compositions, the extrinsic contribution is relatively small, thus leading to better mechanical properties.

Figure 4.10 shows the fracture cross section after bending tests of LNKN4 and LNKN6, poled under an electric field ***E*** of 3 kV/mm. The arrow in the figure represents the poling direction, and the samples shown serve as references for each composition.

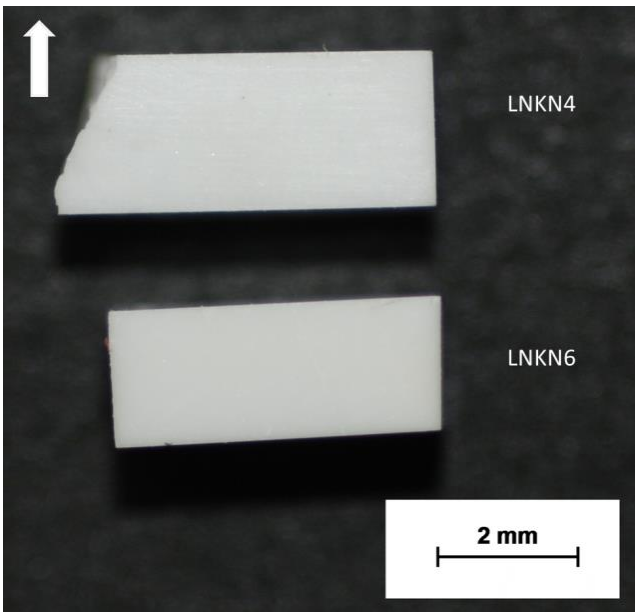

*Figure 4.10: Fracture cross section after bending tests of LNKN4 and LNKN6, poled under an electric field **E** = 3 kV/mm*

Whereas a straight crack can be found for LNKN6, the crack in LNKN4 propagated in a curve. Hence, samples with improved flexural strength generally showed the same cracking behavior as LNKN6. Samples with decreased flexural strength mainly acted like the LNKN4 sample shown. This was seen as an indicator of crack formation, mainly perpendicular to the poling direction.

Indentation tests gave more information about the phenomenon in NKN-based ceramics. It was shown that the mechanical properties are anisotropic after poling took place. Since the specimens are poled through the thickness, Vickers indents are isotropic on the electrode surface and anisotropic on the other surfaces.

Figure 4.11 shows the indentation-induced cracks for the isotropic and anisotropic planes.

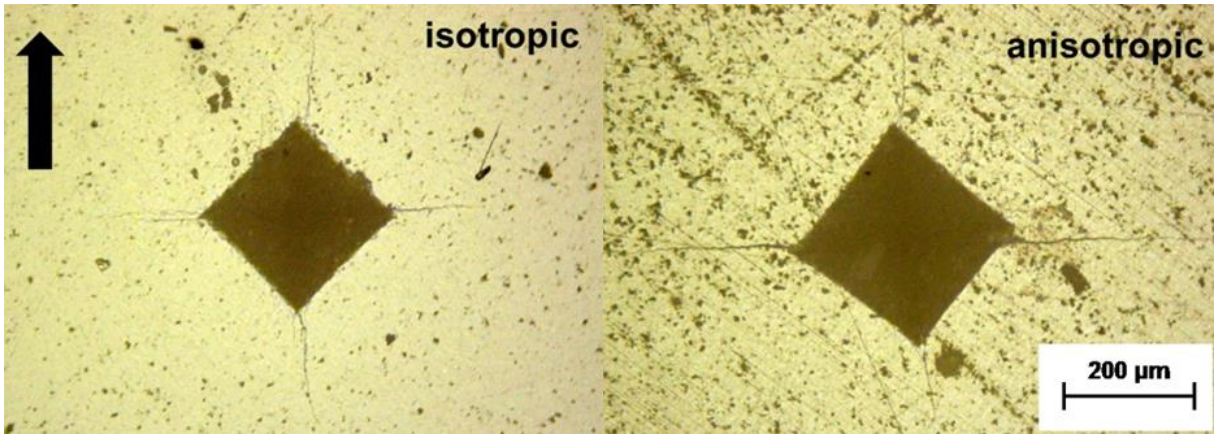

Figure 4.11: Indentation-induced cracks for the isotropic and anisotropic case.

From this figure, it can be seen that the indenting crack length increased perpendicular to the poling direction and decreased parallel to it. This result is consistent with the studies on PZT. [82,98–100] The hardness of the different materials was determined and the effect of Li observed. Figure 4.12 shows the hardness as a function of different Li-content.

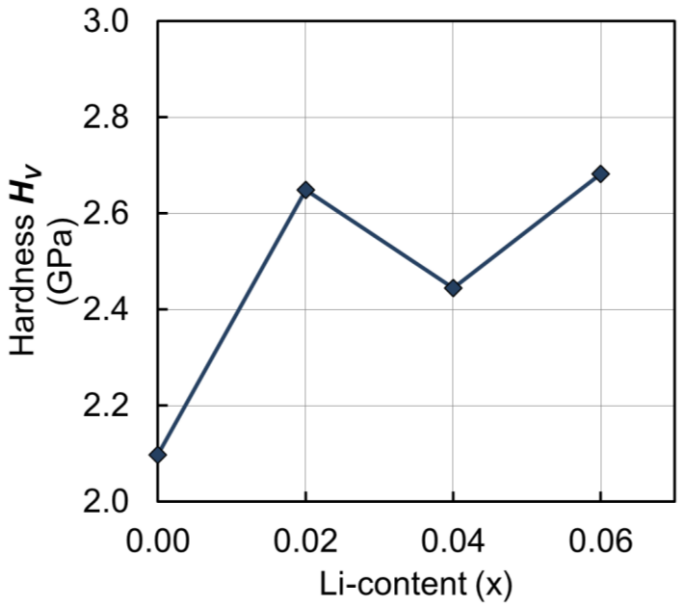

Figure 4.12: Hardness values from Vickers indentation tests as a function of Li-content.

The measurements implied that the hardness showed an increasing tendency with increasing Li content. Hardness is like the flexural strength dependent on the grain size and porosity of the sample. In this case, porosity seemed to be most pronounce as the hardness increased with increasing density. An influence of Li on the hardness can therefore not be made.

With the values of hardness and equation (2.10) the fracture toughness K_C could be determined. Figure 4.13 (a) and (b) summarize the resulting K_{IC} and K_C values for all materials.

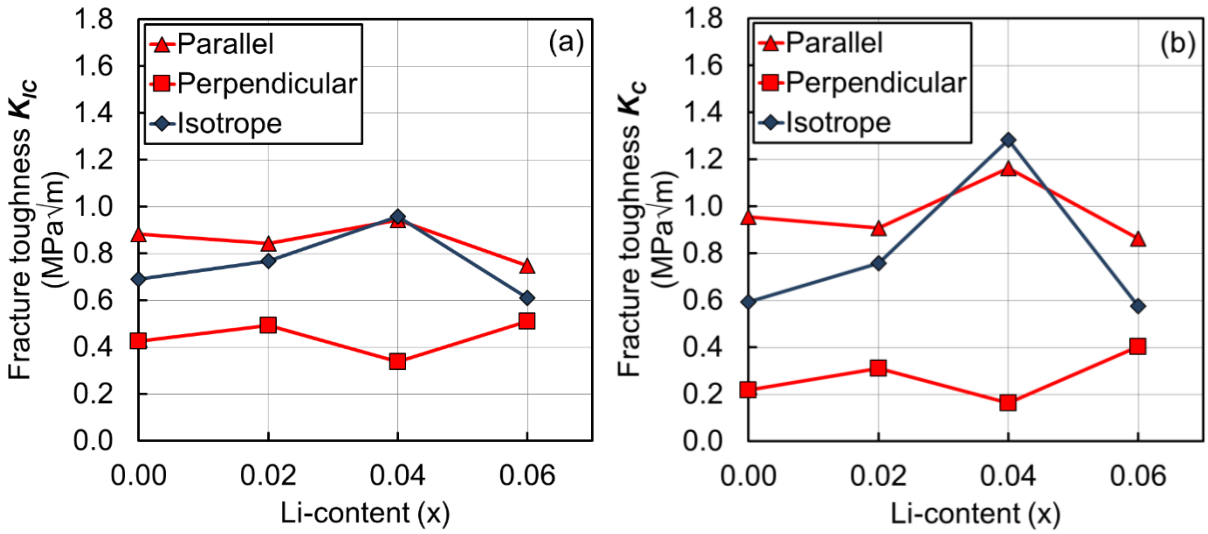

Figure 4.13: Influence of Li content on the fracture toughness K_{IC} (a) and K_C (b) of different surfaces. Parallel and perpendicular direction are subjected to the poling direction.

It is evident by comparing the fracture toughness K_{IC} and K_C, which were obtained using different equations, that K_C shows larger variation in its value, making it more sensitive for these calculations. Thus, changes in the material are more obvious when comparing the K_C value. In the isotropic case, both fracture toughness K_{IC} and K_C became maximum at a Li content of 4 mol%. Furthermore, LNKN4 experienced no recognizable improvement in the poling direction. K_C even shows a decrease for crack propagation parallel to the poling direction. Further, the fracture toughness K_{IC} and K_C decreased considerably in the perpendicular direction. The other compositions experienced a lower fracture toughness vertically as well. But in contrast to LNKN4, the other materials showed a significant improvement in parallel direction. This

anisotropic behavior is attributed to the internal stress due to the extrinsic and intrinsic processes. Another factor that cannot be excluded is the micro crack formation.[55)]

Another indicator of these processes can be found in the results of the Weibull modulus ***m***. At higher electric fields, the crack formation and propagation are more likely to occur.[55)] Hence, the variation of the resulting flexural strengths increased and the Weibull modulus ***m*** decreased eventually. In PZT ceramics, the flexural strength usually decreased by applying an electric field. Nevertheless, NKN ceramics showed improved mechanical strength at a 90° domain switching fraction of about 20 – 30%.

4.3 Conclusion

The effects of domain switching on the mechanical and piezoelectric properties of doped alkali niobate (NKN) based piezoelectric ceramics were examined. NKN ceramics with different amounts of Li were poled under different electric fields. Owing to increasing 90° domain switching with increasing poling field, the piezoelectric properties were enhanced. Nevertheless, the extrinsic contribution in the form of domain wall motion especially in the case of LNKN4 must not be excluded. Young's modulus Y_{33} and Poisson's σ ratio were measured via ultrasonic velocity tests. Y_{33} decreases and increases with increasing poling field. These results are consistent with findings from other piezoelectric materials such as PZT. A novelty obtained from our results is the improvement of the flexural strength at lower poling fields. Three-point bending tests were carried out to determine the flexural strength of NKN-based ceramics. The compositions, except for LNKN4, showed a relatively constant behavior with increasing poling field. The results indicated that domain wall motion is a critical factor and likely decreased the mechanical properties of LNKN4. For the other compositions, mainly due to the volume contribution, internal stress fields are formed, which enhanced the mechanical strength at a domain fraction of about 20 – 30%. Nevertheless, after exceeding a certain value, these internal stresses also caused crack formation and propagation. Indentation tests confirmed these ideas by showing the anisotropic behavior of the fracture toughness after poling. Whereas the cracks parallel to the poling field became shorter, an elongation was found perpendicular to the poling direction. In addition, LNKN4 showed the highest decrease in the fracture toughness, which might have led to the decrease in the flexural strength. The fracture cross section showed that the crack propagation had a curve like behavior. These facts

indicated that failure of the LNKN4 samples happened owing to the loss of the fracture toughness in perpendicular direction. In conclusion, the poling induced mechanical properties led to an increase and decrease of the flexural strength, respectively. It seemed possible that the variation of the intrinsic and extrinsic contributions could have been the main reason. Both processes led to internal stresses in the sample, which can improve or decrease the mechanical strength. Especially domain wall motion led to critical internal stresses and mainly decreased the mechanical properties.

5 Electromechanical fatigue process under unipolar AC field

Influence of different DC fields showed, that LNKN6 had the highest piezoelectric properties and had the second highest mechanical properties. For this reason, the unipolar fatigue behavior of pure $Li_{0.06}Na_{0.52}K_{0.42}NbO_3$ (LNKN6-a) and the same compound with additives (LNKN6-b) was observed. Unipolar cycling was performed between room temperature and 150 °C under a high unipolar electric field of 4 kV/mm. LNKN6-a fatigued under crack formation throughout the examined temperature range and the switchable polarization $2P_r$ decreased for 20 % (= 2µC/cm^2) at 150 °C. In contrast, mechanical degradation was not observed in LNKN6-b, but a decrease of $2P_r$ by 15 % (= 3.2 µC/cm^2) was observed at 150 °C. Noteworthy is the fact that at 50 °C, fatigue-free behavior was observed for LNKN6-b over at least 10^6 cycles. The influence of phase transition on this fatigue-free behavior was discussed.

5.1 Experimental procedure

Two different materials were used for the fatigue tests: $Li_{0.06}Na_{0.52}K_{0.42}NbO_3$ (LNKN6-a) and $Li_{0.06}Na_{0.52}K_{0.42}NbO_3$ with additives: 0.65 mol% Li_2CO_3, 1.3 mol% SiO_2, 0.2 mol% $MnCO_3$, 0.5 mol% $SrCO_3$, and 0.5 mol% ZrO_2 (LNKN6-b). More information about the materials can be found in [101]. The ceramic samples were cut and ground into rectangular bars with a thickness of about 0.6 mm, a width of 2.1 mm, and a length of 10.5 mm. The larger surfaces were coated with silver and annealed at 700 °C for 5 min. Subsequently, the samples were poled in silicon oil under an applied electrical field of E = 3 kV/mm for 30 min and a temperature of 100°C for LNKN6-a and 150 °C for LNKN6-b. The samples were cooled down to 40 °C with the electric field still switched on.

To apply the cyclic electric fields, the samples were placed between a metallic needle and electrode. To avoid arcing, this set-up was immersed in a bath of silicon oil. A function generator (Multifunction Synthesizer WF 1943A, NF Corporation, Yokohama, Japan) connected to an amplifier (Model 610D, TRek Inc, New York, USA) was used to apply a sinusoidal unipolar signal with a frequency of 50 Hz onto the samples for up to 10^6 cycles. The amplitude during these fatigue tests was 4 kV/mm; this is approximately four times the coercive field E_c for LNKN6-a and approximately 3 times that for LNKN6-b. The fatigue tests were performed at selected temperatures between

room temperature and 150 °C. Care was taken that the applied electric field was aligned in the same direction as the polarization field of each sample. The temperature of the sample during the electric fatigue test was measured by using a temperature sensor (Keyence thermosensor, Osaka, Japan). To obtain reliable results for long-time changes in material characteristics after fatigue tests, 4 samples were tested under each temperature and additional experiments were performed after 48 h. ***P(E)*** hysteresis loops were determined with a ferroelectric tester (TF Analyzer 2000, aixAcct, Aachen, Germany) at room temperature. The piezoelectric strain constant $\boldsymbol{d_{33}^{S}}$ was measured via laser Doppler vibrometer (DemodulaterAT3600, Graphtec, Yokohama, Japan). The measuring frequency and electric field was 1 kHz and 0.5 kV/mm, respectively.

3-point bending tests were carried out using an Instron 5582 (Instron, Boston, USA) with a load cell capacity of 5 kN and a crosshead speed of 0.1 mm / min. To quantify the average bending strength and reliability of each composition, the flexural strength data for each material is fit to a Weibull distribution, with 15 samples for each composition and fatigue condition, including the poled case as well.

For X-ray diffraction data the silver electrodes were polished off, and the data were obtained by an X-ray diffractometer (X'Pert Pro, PANalytical, Almelo, Netherlands) with a Cu Kα1 radiation source. Step mode measurements contained step width of 0.017° and the total spectrum between an angular interval from 10° to 100° was collected at room temperature. The collected data was refined, using the XRD Rietveld method supported by the software FULLPROF.[84)] We modeled both materials, using space groups P4mm with coexisting Amm2 and used the Pseudo-Voigt function to define the profile shape. Two samples for each composition and temperature were further used for SEM evaluations. The surfaces vertical to the poling directions of the samples were mechanically polished with SiC powder (#600–#2000) and finished by polishing with colloidal silica. To reveal domain structures, the polished samples were chemically etched for about 45 min with a mixture of HF:HCl:H_2O = 1:1:18 by volume. A thin layer of Au/Pd was sputtered onto the samples to avoid charging; then, domain configurations were observed using a SEM system (JSM-7001F, JEOL, Tokyo, Japan) at an acceleration voltage of 5 kV.

5.2 Results

At first, certain properties of the two materials are compared to each other. The x-ray diffraction (XRD) pattern of LNKN6-a and LNKN6-b are shown in Figure 5.1. The microstructure was observed via SEM and is shown in Figure 5.2 (a) and (b).

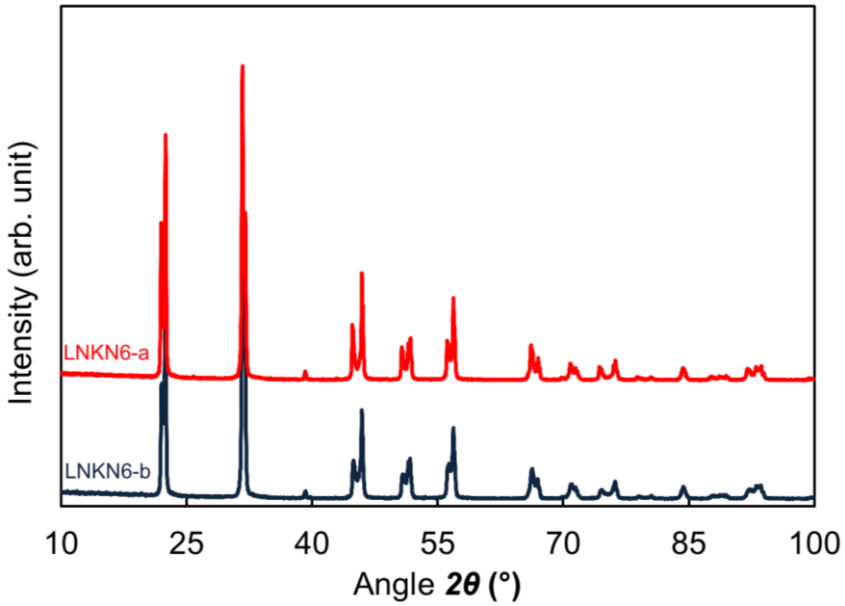

Figure 5.1: X-ray diffraction of LNKN6-a and LNKN6-b.

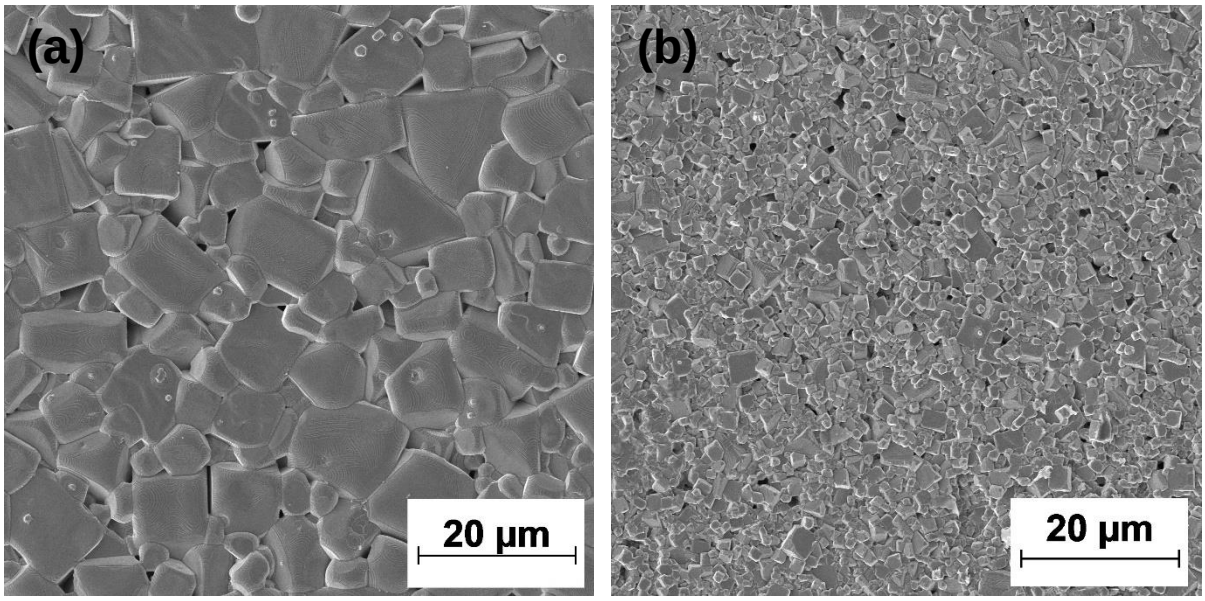

Figure 5.2: SEM images of the microstructure of LNKN6-a (a) and LNKN6-b (b).

As shown by the patterns, both samples do not differ much from each other. However, Rietveld refinement showed the difference in phase composition. Furthermore, different grain sizes can be observed for both samples, with LNKN6-b having a reduced grain size compared to LNKN6-a. Table 5-1 compares the weight percentage ***wt%*** of the tetragonal phase (P4mm) to the orthorhombic phase (Amm2) in both materials before and after poling, as well as the grain size and different piezoelectric properties.

*Table 5-1: Weight percentage of tetragonal phase and piezoelectric properties of LNKN6-a and LNKN6-b. The calculated **R** values of the Rietveld refinement were about R_{wp} = 28 and R_{exp} = 6.9.*

Material	Condition	*wt%* tetragonal phase (%)	d_{31} (pC/N)	k_{31} (%)	Q_m	Y_{11}x10^{10} (N/m^2)	Grain size (µm)
LNKN6-a	**Unpoled**	85.5 ± 2.5	\	\	\	\	9 ± 2
	Poled	86.0 ± 3.5	- 85 ± 2	23.0 ± 0.5	50 ± 3	8.1 ± 0.1	
LNKN6-b	**Unpoled**	2.3 ± 1.2	\	\	\	\	4 ± 1
	Poled	3.5 ± 1.1	- 60 ± 2	22.5 ± 0.2	115 ± 4	8.1 ± 0.1	

The Young's moduli Y_{11} as well as the coupling factors k_{31} for LNKN6-a and LNKN6-b have similar values. Overall, LNKN6-b had a lower weight percentage of the tetragonal phase than LNKN6-b in the poled and unpoled case. For both materials, the weight percentage increased after poling took place. Because d_{31} and Q_m are inversely proportional, LNKN6-a had a higher piezoelectric coefficient d_{31} and lower mechanical quality factor Q_m than LNKN6-b.

Figure 5.3 shows the shows the temperature dependence of the relative permittivity $\varepsilon_{33}/\varepsilon_0$ and the dielectric loss ***tan δ*** for poled LNKN6-a and LNKN6-b.

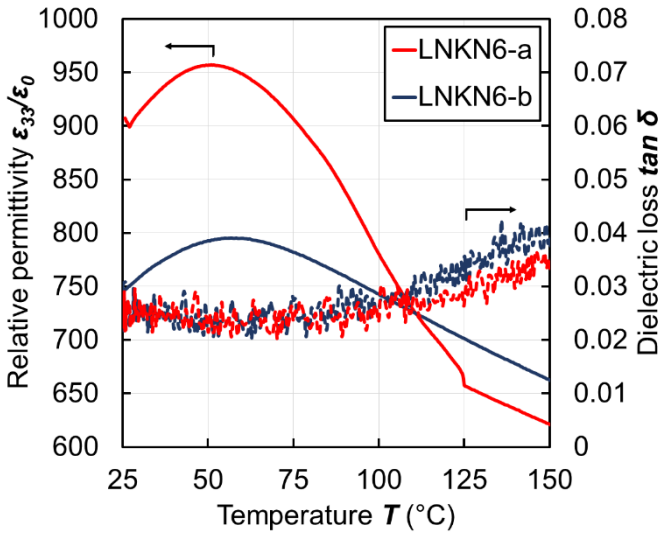

Figure 5.3: Relative permittivity and dielectric loss of LNKN6-a and LNKN6-b as a function of temperature.

The dielectric loss ***tan δ*** was on the same level for both materials and increased with increasing temperature. LNKN6-a had higher relative permittivity values (ε_r = 900) at room temperature than LNKN6-b with ε_r = 750. In the observed temperature range, the permittivity shows a maximum in both materials around 50 °C, with ε_r = 950 and ε_r = 800 for LNKN6-a and LNKN6-b, respectively. After 50 °C, the permittivity of LNKN6-a decreased more significantly than LNKN6-b and showed lower values after a temperature of about 110 °C. LNKN6-b exhibited a very stable temperature dependence of the dielectric permittivity over the range of room temperature to 150 °C. Thus, the composition of LNKN6-b shows less susceptibility against temperature change. After fatigue experiments, changes in the ferroelectric properties were observed.

Figure 5.4 (a) - (d) represents the ***P(E)*** hysteresis loops of LNKN6-a and LNKN6-b before and after fatigue temperatures of room temperature and 150 °C.

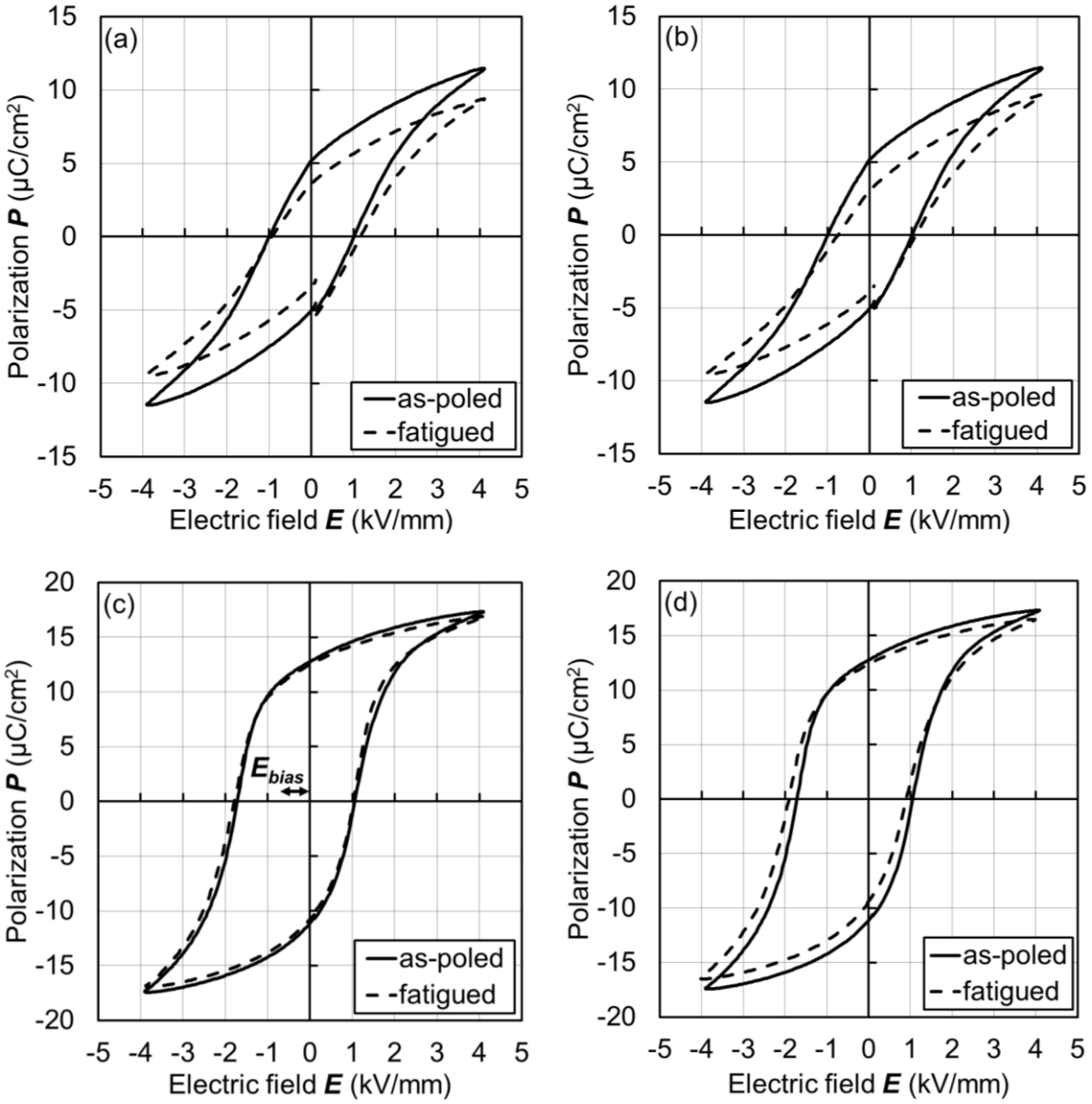

Figure 5.4: P(E) hysteresis of LNKN6-a as-poled and fatigued at room temperature (a) and 150 °C (b), as well as LNKN6-b as-poled and fatigued at room temperature (c) and 150 °C (d).

In general, LNKN6-b has a higher switchable polarization $2P_r$ and coercive field E_C than LNKN6-a. According to the ***P(E)*** hysteresis loops, the switchable polarization $2P_r$ and the coercive field E_C of unfatigued samples were 10.1 µC/cm^2 and 0.95 kV/mm for LNKN6-a and 21.6 µC/cm^2 and 1.35 kV/mm for LNKN6-b, respectively. In both materials, the switchable polarization $2P_r$ decreased after the fatigue experiments.

Figure 5.4 (a) shows the fatigue behavior of LNKN6-a under room temperature and an increase of the coercive field E_C is apparent. In Figure 5.4 (b) - (d), the coercive field E_C remained constant, and the hysteresis loops shifted.

Figure 5.5 (a) and (b) show the changes of switchable polarization $2P_r$ and E_C after 10^6 cycles at different temperatures. The values of the fatigued samples $2P'_r$ and E'_C were normalized by dividing them with the initial values $2P_r$ and E_C, respectively. The highlighted line represents the unfatigued state of a poled sample.

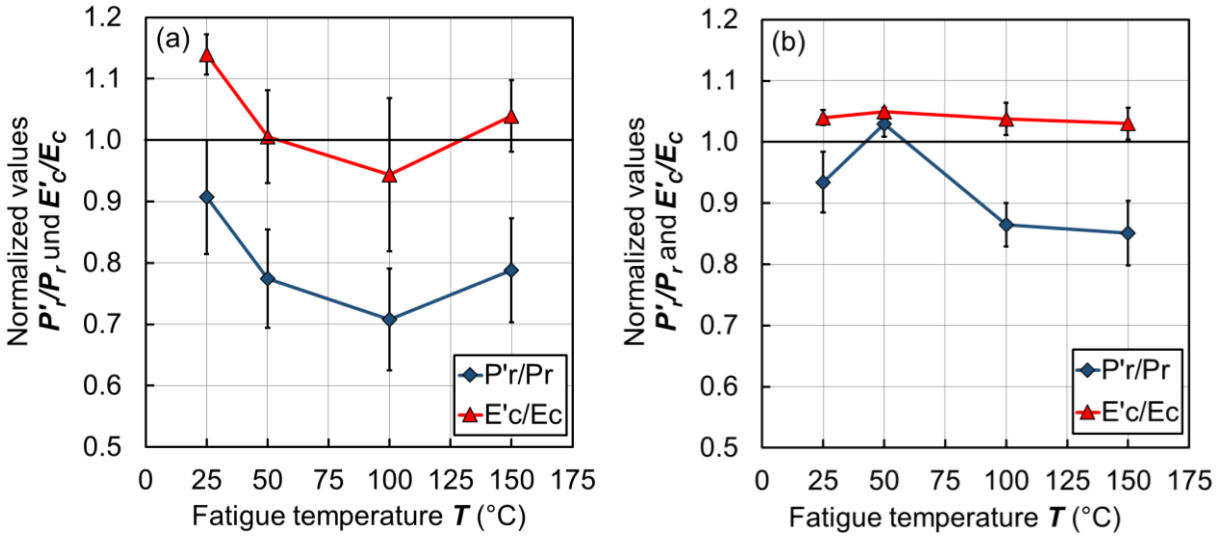

*Figure 5.5: Normalized **2Pr** and coercive field E_C of LNKN6-a (a) and LNKN6-b (b) at different fatigue temperatures.*

As mentioned before, the switchable polarization decreased after the fatigue experiments. As shown in Figure 5.5 (a) and (b), this was the case for LNKN6-a for each temperature condition and for LNKN6-b for each temperature T except 50 °C. On the other hand, the coercive field E_C remained constant for LNKN6-b throughout each condition. For LNKN6-a, the average value of the coercive field after fatigue at temperatures higher than room temperature would also suggest that almost no change occurred in the material. After the fatigue tests at room temperature, the coercive field of LNKN6-a increased for about 15 %. $2P_r$ decreased with increasing temperature and reached a minimum at 100 °C with a nearly 30 % (= 3 µC/cm^2) reduction. At 150 °C $2P_r$ of LNKN6-a and LNKN6-b declined by 20 % (= 2 µC/cm^2) and 15 % (=3.2 µC/cm^2), respectively. Noteworthy is that at 50 °C, $2P_r$ of LNKN6-b remained at the same value as in the unfatigued case, suggesting that no fatigue appeared under this conditions.

As shown in Figure 5.4 (a) – (d), besides changes in coercive field and switchable polarization, the ***P(E)*** loops shifted after the fatigue experiments. Due to the poling process, both samples had an internal bias field E_{bias}. These residual internal bias fields $E_{bias} = ½(|E_C^-| - |E_C^+|)$ were evaluated for both samples to 0.1 kV/mm and 0.35 kV/mm for LNKN6-a and LNKN6-b, respectively. Figure 5.6 shows the internal bias field after the fatigue tests at different fatigue temperatures. The highlighted lines are the values of poled LNKN6-a and LNKN6-b.

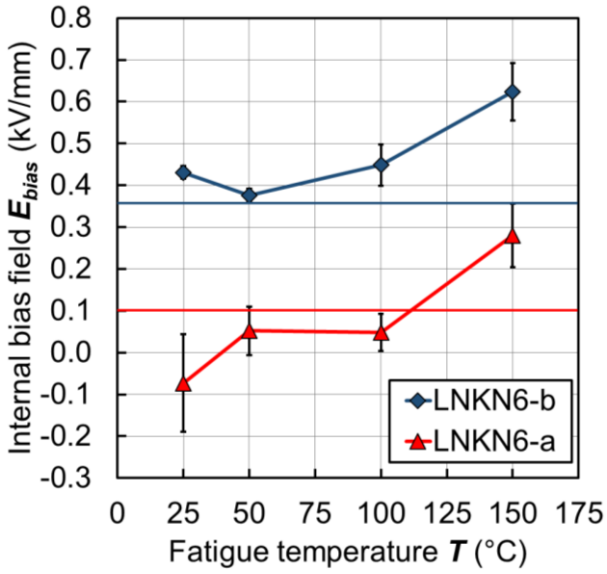

Figure 5.6: Internal field E_{bias} of fatigued LNKN6-a and LNKN6-b at different fatigue temperatures.

At lower temperatures, the changes of the internal bias field differ for both materials. After fatigue at room temperature, the internal bias field of LNKN6-a reached negative values of about – 0.1 kV/mm and at 50 °C and 100 °C E_{bias} reached positive values, but were still slightly lower than the poled case. LNKN6-b, showed an increase of the internal bias field at each temperature condition, except 50 °C. Only for fatigue tests at 150 °C the changes of the internal bias field were similar for both materials. E_{bias} increased for about two times its initial value for LNKN6-a (= 0.29 kV/mm) as well as for LNKN6-b (= 0.6 kV/mm). In Figure 5.6, another considerable fact is the fatigue-free behavior of LNKN6-b at 50 °C.

Table 5-2 summarizes the results of the piezoelectric properties of LNKN6-a and LNKN6-b before and after fatigue at different temperatures.

Table 5-2: Piezoelectric properties of poled and fatigued LNKN6-a and LNKN6-b at selected temperatures.

		as-poled	25°C	50°C	100°C	150°C
LNKN6-a	d_{31} (pC/N)	−85 ± 2	−92 ± 8	−94 ± 2	−96 ± 12	−85 ± 11
	k_{31} (%)	23 ± 0.5	24.1 ± 1.7	23.9 ± 0.8	24.8 ± 1.2	21.8 ± 0.2
	Q_m	50 ± 3	45 ± 10	35 ± 6	39 ± 14	43 ± 17
	Y_{11} x 10^{10} (N/m^2)	8.1 ± 0.05	8.0 ± 0.3	8.0 ± 0.3	8.0 ± 0.4	8.0 ± 0.7
LNKN6-b	d_{31} (pC/N)	−60 ± 2	−56 ± 0.5	−60 ± 1	−61 ± 4	−60 ± 0.5
	k_{31} (%)	22.5 ± 0.2	22 ± 0.3	22.7 ± 0.3	22 ± 0.4	20.9 ± 0.7
	Q_m	115 ± 4	129 ± 8	103 ± 16	128 ± 4	135 ± 7
	Y_{11} x 10^{10} (N/m^2)	8.1 ± 0.05	8.1 ± 0.3	8.1 ± 0.2	8.1 ± 0.4	8.1 ± 0.05

Table 5-2 shows that Y_{11} remained constant throughout the experiments for LNKN6-a and LNKN6-b. Furthermore, the piezoelectric properties k_{31} and d_{31} of both materials show an inversely proportional behavior to Q_m. For LNKN6-a k_{31} and d_{31} increased under fatigue tests up to temperatures of 100 °C, whereas Q_m decreased. At fatigue tests under 150 °C, k_{31} and d_{31} decreased and Q_m increased. The piezoelectric properties of LNKN6-b increased at 50 °C as well as 100 °C. In case of LNKN6-b the k_{31} decreased, whereas the mechanical quality factor Q_m increased. In addition, the piezoelectric strain constants d_{33}^S were observed, which are shown in Figure 5.7, with the solid lines representing the as-poled values of LNKN6-a and LNKN6-b.

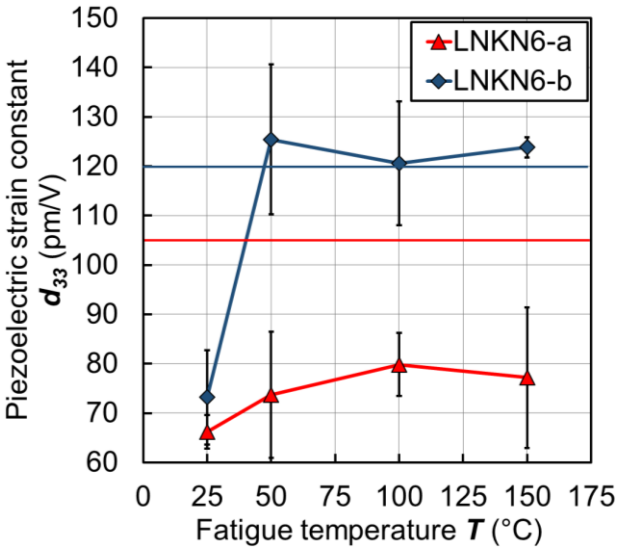

Figure 5.7: Piezoelectric strain constant d_{33}^S of LNKN6-a and LNKN6-b after different fatigue temperatures.

Here, the results show that d_{33}^{S} is decreasing for LNKN6-a throughout the observed temperature range. The degradation had equal values for all fatigue temperatures. In contrast, LNKN6-b seemed only to decrease at room temperature and remained constant after fatigue at 50 – 150 °C.

Figure 5.8 (a) - (c) show the Weibull distributions of LNKN6-a, LNKN6-b and PZT for different fatigue temperatures. Figure 5.8 (d) shows the Weibull distribution of LNKN6-b after fatigue at different electric fields, ranging from 4 to 8 kV.

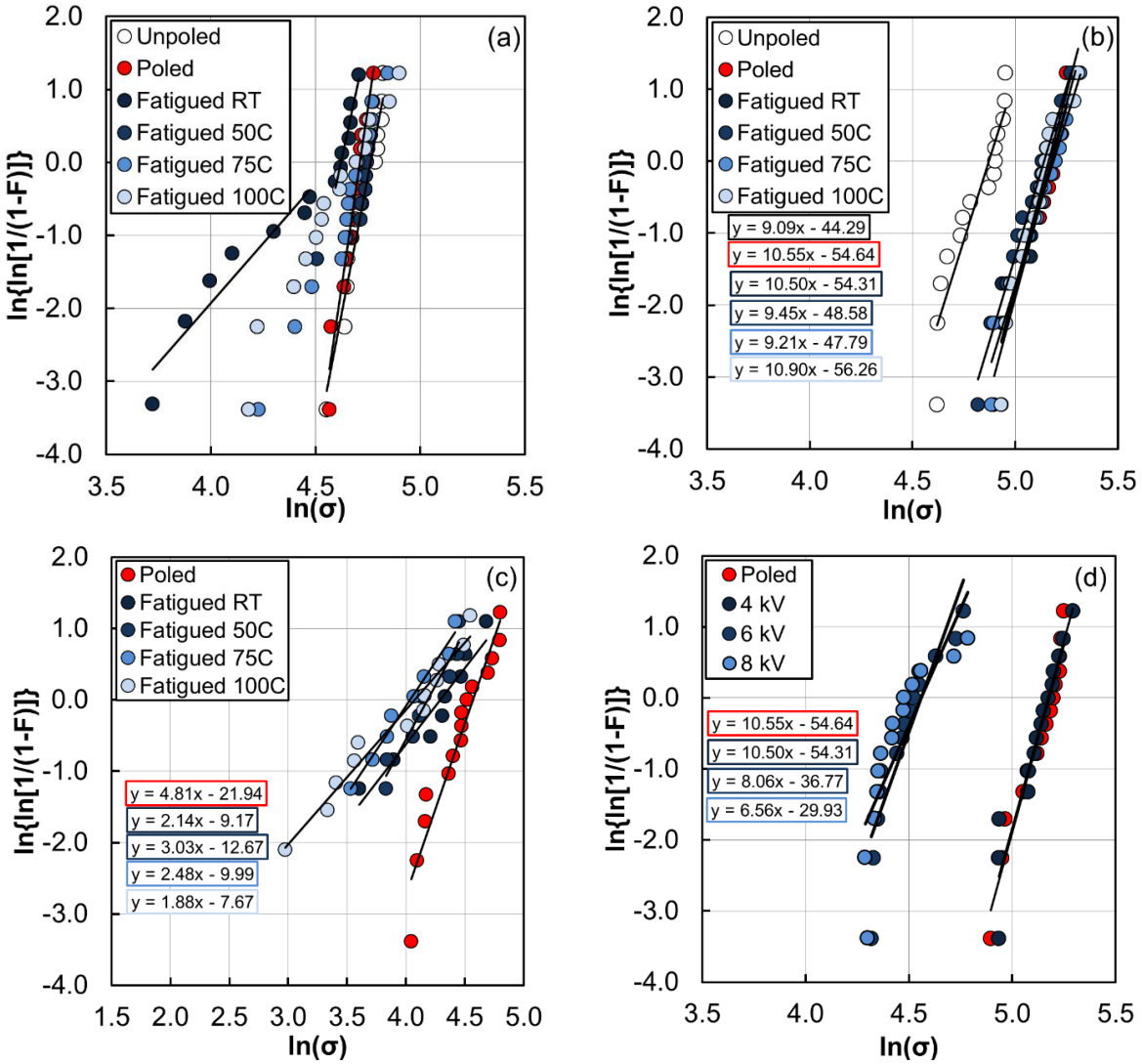

Figure 5.8: Weibull distribution of LNKN6-a (a), LNKN6-b (b) and soft PZT (c) for different fatigue temperatures, as well as LNKN6-b after different electric fields (d).

It was shown that LNKN6-a did not change significantly the flexural strength after poling. The values for unpoled as well as poled were about 115 MPa with a Weibull parameter

m between 15 and 20. Knudsen describes how the porosity and grain size of a material affect the mechanical strength of brittle materials.[94] In our case, due to smaller grain size, LNKN6-b showed improved mechanical properties. Unpoled samples showed a flexural strength σ_0 of 131 MPa, whereas as-poled samples showed an improved value of 177 MPa. The Weibull parameter ***m*** was similar for the unpoled and as-poled samples and was estimated to 9.1 and 10.6, respectively. An improvement of the flexural strength after poling was observed for NKN-based ceramics in chapter 4. Furthermore, LNKN6-a and LNKN6-b showed no significant self-heating effect during fatigue. LNKN6-a showed an increase at room temperature of about 5 °C. At higher fatigue temperatures this temperature difference was not observed. LNKN6-b showed a slight increase of 1 °C for fatigue temperatures from room temperature to 100 °C. We concluded that changes in the temperature are not significant enough to show an effect on the mechanical degradation. The evaluated flexural strength for PZT was about σ_0 = 90 MPa, due to the fact that during poling mechanical degradation occurred, as shown in the literature. It should be noted that the linear fits were only applied to LNKN6-b and PZT, because only in these materials were the values distributed in a line. Whereas, LNKN6-b remained constant over the observed temperature range with a Weibull parameter ***m*** = 10.6, PZT showed decreasing mechanical properties with increasing temperature. Figure 5.8 (d) shows that LNKN6-b decreased in flexural strength and Weibull parameter at unipolar cycling fields of about 6 kV/mm.

These facts are summarized in Table 5-3.

Table 5-3: Flexural strength and Weibull modulus of LNKN6-b and PZT after fatigue at different fatigue temperatures. The numbers in brackets represent the lowest and highest measured value for this condition.

	Fatigue temperature *T* (°C) / Electric field *E* (kV/mm)	**Flexural strength *σ* (MPa)**	**Weibull parameter *m***
LNKN6-b	**unpoled**	131 [102; 141]	9.1
	as-poled	177 [133; 190]	10.6
	R.T. / 4	176 [138; 199]	10.5
	50 / 4	171 [123; 194]	9.5
	75 / 4	179 [132; 204]	9.2
	100 / 4	174 [139; 202]	10.9
	R.T. / 6	96 [75; 117]	8.1
	R.T. / 8	95 [74; 119]	6.6
PZT	**as-poled**	96 [57; 121]	4.8
	R.T. / 4	73 [37;108]	2.1
	50 / 4	65 [46;85]	3.0
	75 / 4	56 [34;82]	2.5
	100 / 4	59 [20;94]	1.9

For LNKN6-a, the Weibull distribution showed bimodal character after fatigue, which can be described by the following equation.

$$F(\sigma) = 1 - f\exp\left\{-\left(\frac{\sigma}{\sigma_{0,1}}\right)^{m_1}\right\} - (1-f)\exp\left\{-\left(\frac{\sigma}{\sigma_{0,2}}\right)^{m_2}\right\} \qquad (5.1)$$

where ***f*** is the fraction of a sub distribution. By looking closer at the different Weibull distributions, bimodal distributions were found in LNKN6-a for all fatigue temperatures.

The results are summarized in Table 5-4:

Table 5-4: Flexural strength and Weibull modulus for bimodal Weibull distributions for LNKN6-a after fatigue at different fatigue temperatures.

Fatigue temperature *T* (°C)	Flexural strength *(*MPa)		Weibull parameter		Fraction f
	σ_{01}	σ_{02}	m_1	m_2	
unpoled	/	117 [95; 124]	/	14.9	/
as-poled	/	111 [96; 118]	/	19.6	/
R.T.	71 [41; 88]	106 [102; 110]	4.1	31.1	0.47
50	88 [65; 104]	117 [111; 120]	5.8	44.0	0.33
75	83 [68; 88]	115 [102; 127]	8.8	16.8	0.2
100	75 [65; 81]	113 [85; 134]	9.1	8.3	0.2

The flexural strength of the second sub distribution remained relatively constant for the observed temperature range, but decreased in all cases for the first sub distribution. It is more difficult to see a tendency for the Weibull parameter ***m***. The first sub distribution decreased at room temperature compared to as-poled samples. With increasing temperature, ***m*** started to increase until a value of 9.1 at 100 °C. The second sub distribution showed increased ***m*** of 31 and 44 at room temperature and 50 °C, respectively. In contrast, higher temperatures seemed to decrease the Weibull parameter ***m***. Compared to as-poled samples, m decreased at 75 °C and 100 °C to 16.8 and 8.3, respectively. The fraction ***f*** of the first sub distribution showed a maximum value of 0.47 at room temperature and decreased with increasing temperature to 0.2 at 100 °C.

5.3 Discussion

After fatigue at several temperatures, no significant changes were observed for piezoelectric charge constants, but the piezoelectric strain constant d_{33}^{S} and ***P(E)*** hysteresis loops showed different fatigue behaviors depending on the material and temperature. For LNKN6-a after each fatigue experiment as well as for LNKN6-b at room temperature, the strain was lower compared to as-poled samples. The switchable polarization $2P_r$ decreased, an internal bias field E_{bias} was observed and the coercive field E_C remained relatively constant. Two noteworthy observations were made for the fatigue conditions of LNKN6-a under room temperature and LNKN6-b under 50 °C.

LNKN6-a showed an increased coercive field after fatigue at room temperature, and no fatigue of LNKN6-b was observed at 50 °C. In many cases, the fatigue behavior was similar to the observations made in the literature for PZT. Fatigue studies on PZT explain different processes that can appear during electric cycling of piezoelectric materials. The inherent processes responsible for unipolar fatigue are attributed to induced charge carrier accumulation during electric field cycling. The domain mobility is not significantly affected by these charge carrier accumulations and it is therefore more likely that these accumulations develop at grain boundaries.[102] The main charge carriers in PZT structures are oxygen vacancies[103] and thus unipolar fatigue effects can be attributed to their accumulation.[20] This accumulation leads to an increase of an internal bias field as well as a decrease of the switchable polarization.[20,46,49,104,105] Yao et al. explained the development of the internal bias field during unipolar fatigue. At grain boundaries the polarization vectors of domains in neighboring grains cannot compensate each other due to crystallographic mismatch. This leads to the occurrence of strong, locally varying depolarization fields, which charge carriers, such as oxygen vacancies try to compensate by redistribution. This accumulation of charges forms the local bias field $\boldsymbol{E_{bias}}$, which has the same orientation as the applied field during fatigue.[20] In order to explain the larger bias field in LNKN6-b, we take a closer look at the dopants. From the ion radii of the different elements, we can estimate if they attach to A or B side of the perovskite structure. For this reason Table 5-5 lists the different dopants and ion radius. It should be noted that the values for B side ions were taken with a coordination number of 6, whereas the A side ions were taken with a coordination number of 12.

Table 5-5: List of elements and their respective ion radius.

Element	Li^+	Sr^{2+}	Mn^{2+}/Mn^{4+}	Si^{4+}	Zr^{4+}
Ion-radius (pm)	92	144	96/53	40	72

Li^+ and Sr^{2+} most probably will take the place on the A side of the perovskite structure. Whereas Li will show no charge defect, the implementation of Sr will be compensated by positive holes. In case of Mn two possibilities remain. Due to the small ion radius and the possibility to have an oxidation state of (IV), the B side is most probable. However, the occupation of the A side cannot be ruled out. As for Si^{4+} and Zr^{4+}, these elements will most likely occupy the B side of the perovskite structure. Thus, it is most

probable that the dopants overall will show an increase of the oxygen vacancies. The overall higher internal bias field in LNKN6-b can be explained, by the increase of oxygen vacancies and space charge accumulation through several dopants. Patterson and Cann showed for CuO-doped NKN ceramics that the fatigue is accelerated, which they explained by the increased number of defects and space charge carriers.[19] Further evidence for increased space charge accumulation in LNK6N-b can be found in the change of switchable polarization. At 150 °C, LNKN6-a showed less of a decrease of the absolute values of $2P_r$ (= 2 µC/cm^2) than LNKN6-b (= 3.2 µC/cm^2). Glaum et al. showed the influence of temperature on E_{bias} and observed a higher induced internal bias field during cycling with increasing temperature.[105] This behavior was also observed for LNKN6-b, where with increasing temperature from 100 °C to 150 °C, the internal bias field after fatigue increased. However space charge accumulation cannot account for all the observed results.

Figure 5.9 (a) and (b) show the micro structure of LNKN6-a and LNKN6-b. The line structure visible in both pictures represent the domain structure.

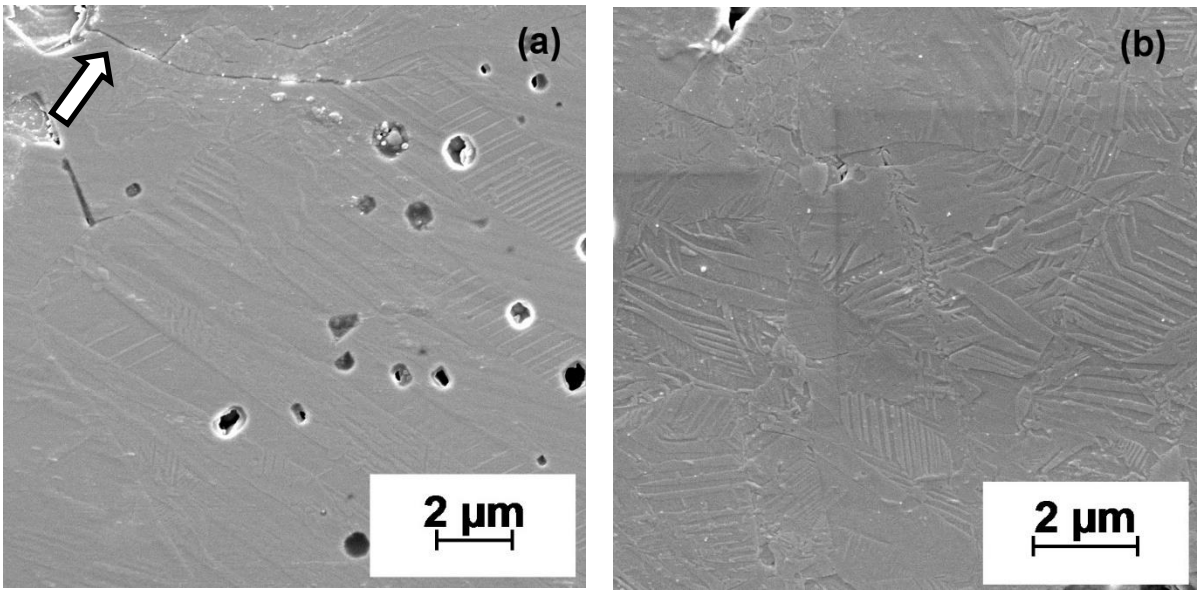

Figure 5.9: Micro structure of fatigued LNKN6-a (a) and LNKN6-b (b) at room temperature. The arrow marks an intragranular micro crack.

An intragranular crack, visible in Figure 5.9 (a), is rarely observed during unipolar cycling, because the introduced stresses are usually too small to initiate cracks. Nevertheless, Jiang et al. showed that crack formation and propagation in PZT during

unipolar cycling depends on grain size and piezoelectric constant d_{ij}[57]. In order the estimate the critical grain size, we used equation (2.6). For estimating the fracture surface energy of the grain boundary, we first calculated the fracture surface energy of the polycrystalline material, by using equation[106]

$$g_{pc} = \frac{(1-\nu^2)\cdot K_{IC}^2}{2Y} \tag{5.2}$$

where ***Y*** is the Young's modulus, ***v*** the Poisson ratio and ***K_C*** the fracture toughness in mode I. In our case, we insert the ***K_C*** value of the indentation tests for poled LNKN6 in perpendicular direction, due to the fact that crack propagation usually occurs perpendicular to the applied electric field. For both materials, the value of poled LNKN6 was used, which is 0.51 MPa√m. This value is consistent with values found in the literature for modified NKN.[24] The fracture surface energy for the grain boundary was then approximated to be 2/3 g_{pc}, because atom bondings are imperfect at the grain boundary. With these values, the critical grain size for LNKN6-a, LNKN6-b and PZT was estimated and summarized in Table 5-6.

Table 5-6: Values needed for the estimation of the critical grain size, as well as the grain size of LNKN6-a, LNKN6-b and PZT.

Material	LNKN6-a	LNKN6-b	LNKN6-b	LNKN6-b	PZT
Young's modulus *Y* (x 10^{10} N/m^2)	7.5	8.0	8.0	8.0	6.9
Piezoelectric constant d_{33} (pC/N)	175	150	150	150	600
Piezoelectric constant d_{31} (pC/N)	90	60	60	60	275
Electric field *E* (kV/mm)	4	4	6	8	4
Fracture surface energy g_b (J/m^2)	1.01	0.95	0.95	0.95	0.04
Grain size *l* (µm)	9 ± 2	4 ± 1	4 ± 1	4 ± 1	1 ± 0.5
Critical grain size l_c (µm)	8	11.2	4.9	2.8	0.1

It should be noted, that g_b of PZT has a value of about 2.4 J/m^2 as shown in the literature.[57] However, these values were estimated for unpoled PZT and can therefore not be applied in this study. With the larger grain size of 9 µm, LNKN6-a was more susceptible to crack formation and propagation, which is consistent with the results we measured. LNKN6-b showed mechanical degradation after an electric field of about 6 kV/mm was applied. The critical grain size for this condition was estimated to be 4.9

µm. With an average grain size of about 4 ± 1 µm, it is quite possible that crack formation appeared at these conditions. Further prove for crack formation can be found in the Weibull distribution of the different Materials. For LNKN6-a, the distribution changed from a unimodal to a bimodal and additionally decreased in value. The occurrence of a sub distribution can be caused by different flaw densities in the as-poled samples of LNKN6-a. An indicator can be found in Figure 5.9 (a), where the crack originated from the largest pore. Thus, a certain pore size and density was needed to form cracks. During fatigue, crack formation and propagation appeared then in a small fraction of LNKN6-a samples, whereas the rest remained unfatigued. This fraction of the sub distribution decreases with increasing temperature and the measured flexural strength of the sub distribution is lower than the initial values measured for poled LNKN6-a. For PZT, with increasing temperature an increase of the crack density was observed. The main reason is the increased domain capability to switch, thereby causing increased stress inside the sample.[60] This behavior can also be observed for LNKN6-a in the temperature range 50 °C to 100 °C. The flexural strength σ_0 as well as Weibull modulus m decrease with increasing temperature, which indicated an increase in the crack density. In addition, the fraction of the sub distribution decreased, which meant that an increasing amount of samples experienced crack propagation. The values also suggested, that during fatigue under room temperature a more significant degradation of the mechanical properties appeared compared to samples fatigued under higher temperatures. It is quite possible, that phase transformation during fatigue experiments occurred, especially since samples fatigued at temperatures > 50 °C showed an increase in the maximum flexural strength compared to room temperature. As domain switching is the main reason for crack formation in the material, phase transformation from tetragonal to orthorhombic is most likely. The orthorhombic phase has an increased amount of domain walls, such as 60°, 90° and 120°, compared to the tetragonal phase with only 90°. In order to decrease the stress from domain switching, the orthorhombic phase increased and allowed for more switching possibilities in LNKN6-a.

After micro-crack formation, the electric field is concentrated at the crack tips and weakened throughout the whole sample. As a result, the effective field inside the sample is less than the applied field, which limits domain switching and consequently decreases polarization and increases the coercive field E_C.[57] Furthermore, the micro cracks reduced unipolar strain as shown above. In LNKN6-b, no cracks were observed

throughout the investigated temperature range, but the decrease in strain at room temperature might suggest the formation of defects in the material. Further, with increasing temperature the crack formation appeared less in LNKN6-a, as suggested by the coercive field measurements from Figure 5.5 (a) and micro structure observation. Hill et al. showed the same behavior in PZT, where with increasing temperature the crack density after unipolar cycling decreased.[60] In case of LNKN6-a, the crack density was the highest after fatigue at room temperature. Because of the negative internal bias field $\boldsymbol{E_{bias}}$ at this temperature, it is suggested that intragranular cracks prevented the material from forming a depolarization field during fatigue. Moreover, LNKN6-a showed larger error bars in Figure 5.5 and Figure 5.6 than LNKN6-b, which can also be the result of micro crack formation, as the process is random. Nevertheless, the fatigue free behavior of LNKN6-b at 50 °C cannot be explained by the above mentioned processes.

Representative impedance measurements are shown in Figure 5.10 (a) – (d) for LNKN6-b at different temperatures. In the figure, the bold lines represent the evaluations of the unfatigued sample, and the dotted lines describe the results of the measurements 48 h after the fatigue experiments. The arrows point in the direction of the changes before and after fatigue tests in the frequencies.

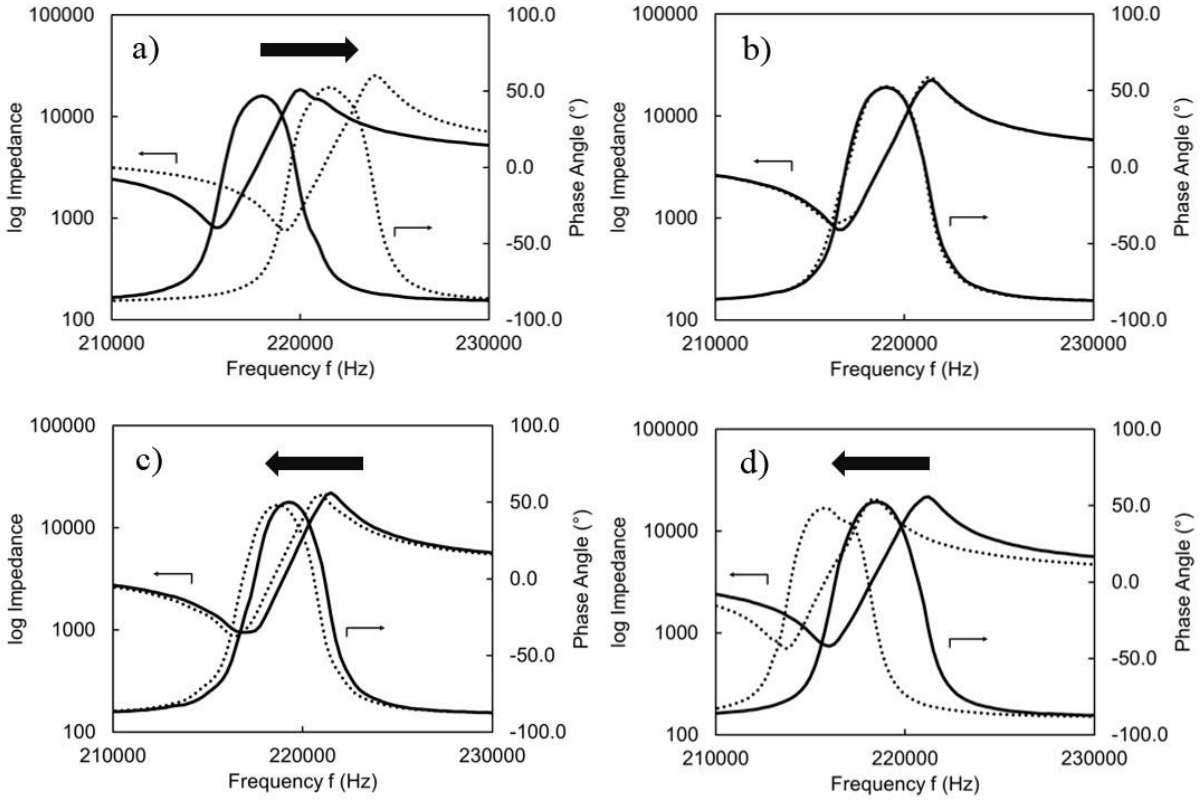

Figure 5.10: Measured values for impedance and phase angle on fatigued LNKN6-b at (a) room temperature, (b) 50 °C, (c) 100 °C and (d) 150 °C. Bold and dotted lines represent measurements of unfatigued and fatigued samples, respectively.

The figures show, that for LNKN6-b samples the fatigue behavior varied with the applied temperature during the tests. At room temperature, resonant and antiresonant frequencies shifted to higher values, together with the maximum in the phase angle. At 50°C, no changes were detected and the sample remained free of fatigue. Above 50°C, fatigue occurred by shifting resonant and antiresonant frequencies slightly to lower values. For LNKN6-a, the measured results shifted to lower frequencies throughout the investigated temperature range.

Figure 5.11 (a) and (b) show the X-ray diffraction patterns from LNKN6-a and LNKN6-b, which are presented as a function of the temperature during fatigue experiments, respectively.

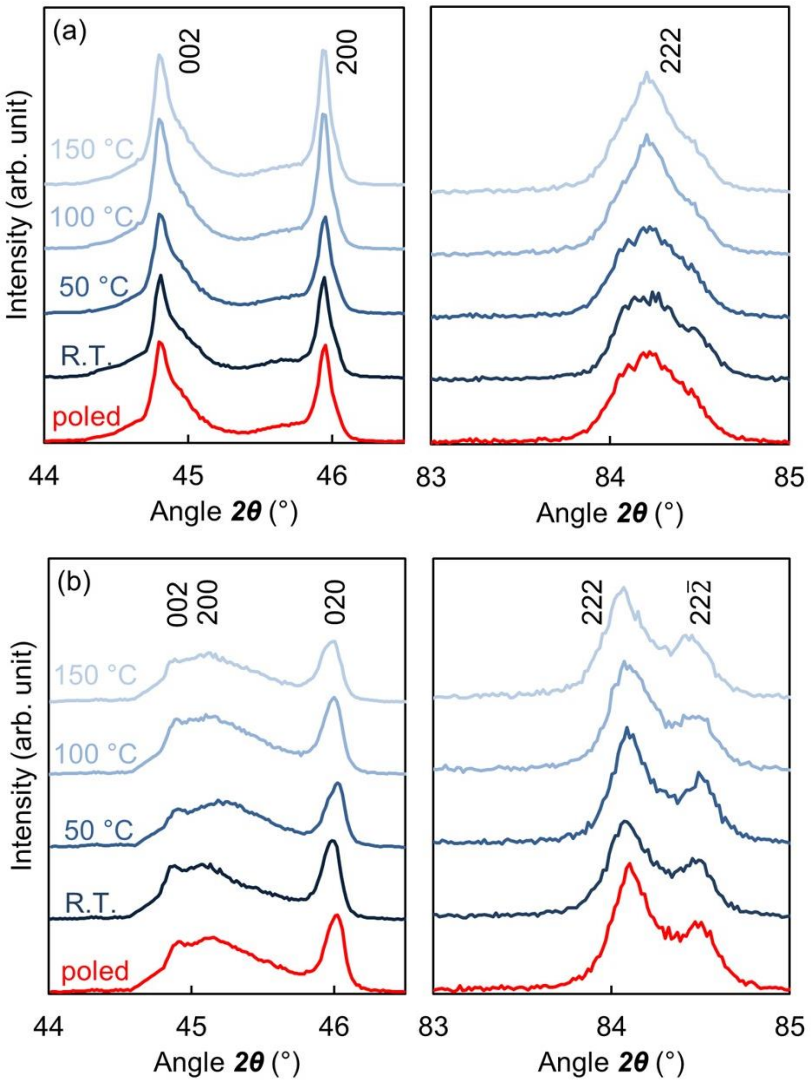

Figure 5.11: XRD profiles of LNKN6-a (a) and LNKN6-b (b) as a function of the fatigue temperature.

Close inspection of the diffraction pattern of LNKN6-b shows two peaks in the range of 2θ = 44° - 47°. The peak at smaller Bragg angles was broaden as a result from the superposition of the (002) and (200) peak. By analyzing the pattern at higher angles at around 84 ° two peaks for LNKN6-b are shown, thereby indicating the coexistence of two phases. It has previously been reported that those phases are orthorhombic and tetragonal.[86] The diffraction pattern of LNKN6-a shows a strong tetragonal character of the material, which is substantiated by the two defined peaks at around 45° and only

one peak around 84°. The region of the pattern of most interest for the characterization of the electric-field-induced transformation is the low and high Bragg angle peaks between 44° and 47°. Upon application of temperature, the reflections in LNKN6-b seemed to remain unchanged, compared to the poled and unfatigued state. In contrast, the intensity of the (200) reflection in the LNKN6-a diffraction pattern clearly increased with increasing temperature. To confirm an electric-field-induced structural phase transformation during fatigue tests, the peak intensities from 44° to 47° were used to evaluate the percentage of the tetragonal phase F_T.[83)]

Figure 5.12 (a) and (b) summarizes the calculated content of the tetragonal phase F_T and the changes of the weight percentage of the tetragonal phase ***wt%***, which were evaluated from the Rietveld refinement, for LNKN6-a and LNKN6-b. The highlighted lines represent the initial values, which were for F_T 75 % for LNKN6-a and 50 % for LNKN6-b, respectively. On the other hand, ***wt%*** was about 85 % for LNKN6-a and about 2 % LNKN6-b.

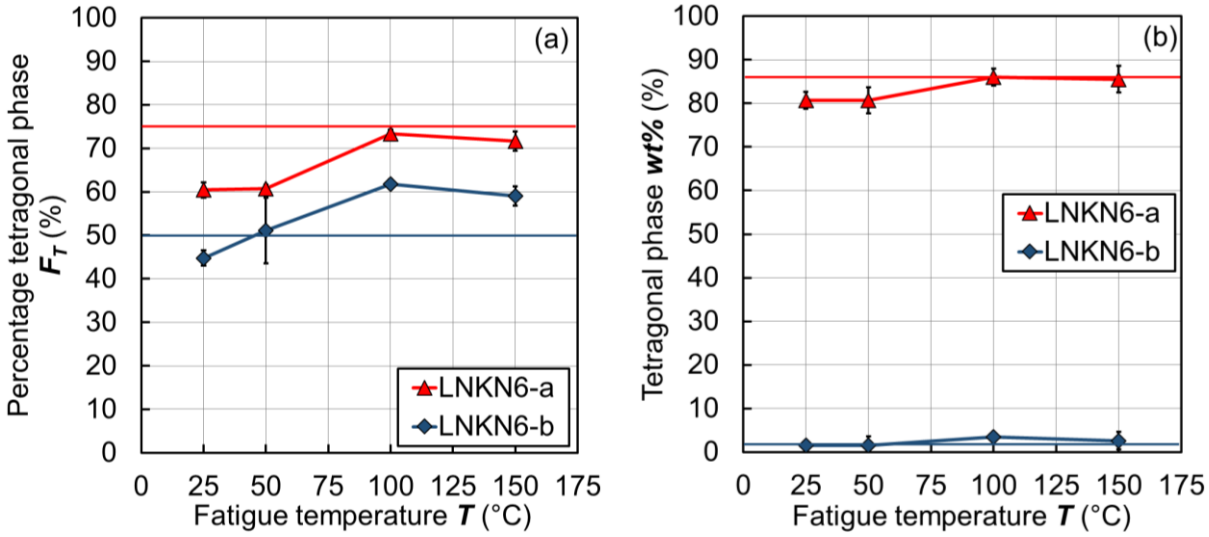

*Figure 5.12: Influence of fatigue temperature on the percentage of the tetragonal phase F_T (a) and the weight percentage of tetragonal phase **wt%** (b) in LNKN6-a and LNKN6-b.*

Comparing both figures, completely different results concerning LNKN6-b can be derived. Whereas the F_T – values increased with increasing fatigue temperature, the weight percentage ***wt%*** remained relatively constant. This error in F_T might be explained by the fact that the equation does not account for a polarized material. We therefore assumed for further discussion that no change in the material occurred.

However, both figures suggested that phase transformation partially appeared in LNKN6-a. In Figure 5.12 (a), those changes either indicated an increase of the tetragonal phase, or further polarization of the sample, as both mechanisms can change the intensity of the peaks. Nevertheless, Rietveld refinement almost showed same behavior, which indicates that the method has its validity. The tetragonal phase of LNKN6-a decreased after fatigue under room temperature and 50 °C. At 100 °C and 150 °C, the tetragonal phase in LNKN6-a showed no changes compared to as-poled samples.

Furthermore, the lattice parameter were evaluated and compared. By looking at different Rietveld refinements in the literature, better reliability factors can be achieved by describing the perovskite structure of the two phase system as a monoclinic one, as shown by Hatano et al.[85]. For this reason, to determine the lattice parameters, the same assumption was made and equations (3.11) to (3.20) were used. It was observed, that poled and unfatigued LNKN6-b samples had lattice parameters of a = 3.997, b = 3.936, c = 4.023 as well as β = 89.7°. From the XRD results, it was shown that the LNKN6-a samples showed tetragonal character and the angle β was estimated to be 90°. Thus, the lattice parameters were then evaluated to be a = b = 3.943 as well as c = 4.038. Another important value, the tetragonality c/a was for unfatigued LNKN6-a and LNKN6-b is 1.024 and 1.007, respectively. With increasing tetragonality, the chance of crack formation increases, which means that LNKN6-a showed higher susceptibility in case of tetragonality, amount of tetragonal phase and grain size.

5.4 Conclusion

The unipolar fatigue behavior of lithium-modified NKN ceramics have been evaluated as a function of temperature in the range from room temperature to 150 °C. In general, the piezoelectric properties in both materials did not decrease significantly, however mechanical degradation was observed. LNKN6-a is especially susceptible to micro crack formation during fatigue at room temperature up to 150 °C. Three-point bending tests showed, that crack formation decreased with increasing temperature. Furthermore, these intergranular cracks lead to a significant decrease of the switchable polarization $\boldsymbol{2P_r}$. This behavior was not observed in LNKN6-b, which showed no micro crack formation throughout the examined temperature range, which is most likely due to smaller grain size. However, in both cases, phase transformation seemed to play an important role. First, LNKN6-b showed fatigue free behavior at 50 °C, which is made possible by phase transformation from orthorhombic to tetragonal. XRD results did not show that phase transformation took place in the material during fatigue, but it is quite possible that phase transformation and the occurring fatigue mechanisms were in an energy equilibrium at 50 °C. Further investigations are necessary to fully understand the processes that occur at this temperature.

Second, LNKN6-a showed a significant improve between room temperature and 50 °C. At higher temperatures the mechanical degradation remained relatively constant. It is therefore suggested that phase transformation from tetragonal to orthorhombic caused this improved behavior. The orthorhombic phase has an increased amount of domain walls, such as 60°, 90° and 120°, compared to the tetragonal phase with only 90°. In order to decrease the stress from domain switching, the orthorhombic phase increased and allowed for more switching possibilities.

6 Crack Propagation during unipolar AC field

In order to investigate the hypothesis, that the orthorhombic phase is more resistant against crack formation and propagation, this chapter compares pure orthorhombic material (Mn-NKN) and pure tetragonal material (PZT) for its fracture toughness and domain structure. Mn-NKN showed higher fracture toughness and resistance against crack propagation despite its large average grain size. In the vicinity of a crack, domain observation showed an increase of 120° and 60° domain walls, which are specific for orthorhombic piezoelectric materials. The domain structure could not be observed for PZT. However, the results suggested that orthorhombic phase was able to decrease the tension field around the crack tip.

6.1 Experimental procedure

Two different materials were used for the fatigue tests, $Na_{0.55}K_{0.45}NbO_3$ + 0.25% MnO (Mn-NKN) and soft PZT. The Mn-NKN samples were synthesized by a mixed-oxide route, explained in chapter 3.1. After sintering at 1092 °C, samples with a size of 2x2 mm^2 and a length of 4 mm were further used. Bulk densities were determined by the Archimedes method. The larger surfaces were coated with silver and afterwards annealed at 700 °C for 5 min. The samples were poled in silicone oil under an applied electrical field of $\boldsymbol{E}$ = 3 kV/mm for 30 min and temperatures of 100 °C and 125 °C for PZT and Mn-NKN, respectively. For the indentation tests, one surface of each sample was indented with a 9.81 N load. The cracks emanating from the corners of the Vickers indents were measured and photographed by laser microscopy. To estimate the fracture toughness $\boldsymbol{K_C}$ and $\boldsymbol{K_{IC}}$ of ferroelectric ceramics, equations (2.10) and (2.11) were used. For fatigue tests, a sinusoidal unipolar signal with a frequency of $\boldsymbol{f}$ = 1; 50 Hz was applied onto the samples for up to 10^4 cycles. The amplitude during these fatigue tests varied from 1 $\boldsymbol{E_C}$ - 4 $\boldsymbol{E_C}$. Care was taken that the applied electric field was aligned in the same direction as the polarization field of each sample. For SEM observations, the surfaces vertical to the poling directions of the samples were mechanically polished with SiC powder (#600 – #2000) and finished by polishing with colloidal silica. To reveal domain structures, the polished samples were chemically etched with a mixture of HF:HCl:H_2O = 1:1:18 by volume. A thin layer of Au/Pd was sputtered onto the samples to avoid charging; then, the surfaces were observed using a SEM system (JSM-7001F, JEOL, Tokyo, Japan) at an acceleration voltage of 5 kV.

6.2 Results and Discussion

The samples were observed via SEM and representative microstructures for the materials are shown in Figure 6.1 (a) and (b).

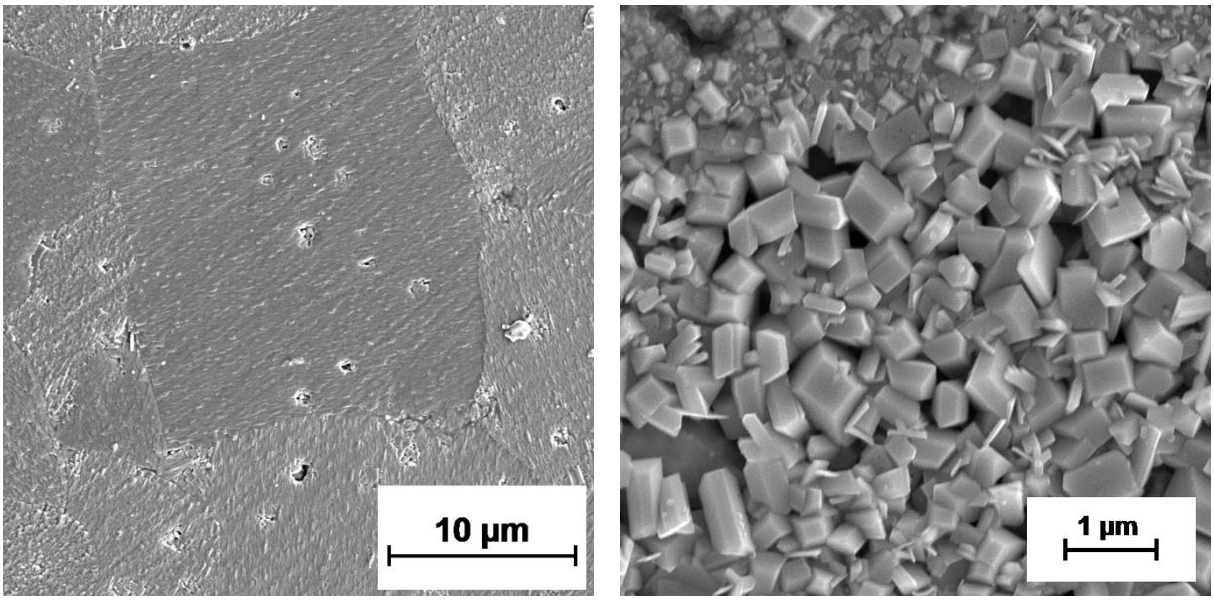

Figure 6.1: SEM images of the microstructure of Mn-NKN (a) and PZT (b).

Basic physical characteristics of the compositions are given in Table 6-1.

Table 6-1: Physical characteristics of the Mn-NKN and PZT.

Material	**Grain size *l* (µm)**	**Density *ρ***	
		Absolute(g/cm³)	**Relative (%)**
Mn-NKN	5.5 – 19	4.19 ± 0,05	93.0
PZT	1.1 ± 0.5	8.13 ± 0,02	98.5

Mn-NKN showed a bimodal grain distribution, with the smallest grain having an average size of about 5.5 µm and the larger grains of about 19 µm. These results showed, that MnO_2 significantly increased the sinter ability of NKN. The grain size for PZT is considerably smaller than for Mn-NKN, with an average size of about 1 µm. The relative density of PZT is increased compared to Mn-NKN, thus the porosity in Mn-NKN was considerably higher. From these results, the mechanical properties of Mn-NKN should be lower according to Knudsen[94)].

Figure 6.2 shows the Vickers hardness of Mn doped NKN and soft PZT. These values represent both materials before and after fatigue, as they did not change significantly.

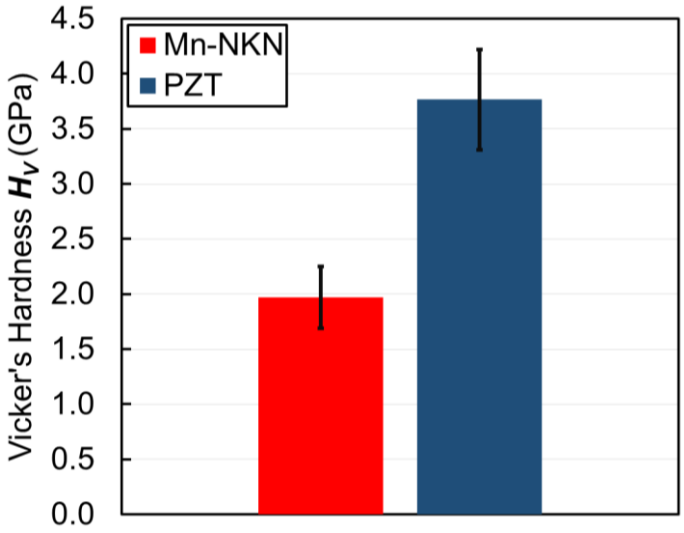

Figure 6.2: Vickers hardness H_V of Mn doped NKN and soft PZT.

It is shown that Mn-NKN has a lower hardness of about 2 GPa compared to PZT with a hardness of about 3.6 GPa. Compared to other alkali niobate based ceramics Mn-NKN had a slightly lower value than NKN. This could be explained by increased porosity and grain size. On the other hand, PZT's increased hardness was a result of high density and significantly smaller grain size. Furthermore, the fracture toughness K_C and K_{IC} were measured. The results are represented in Figure 6.3 (a) and (b).

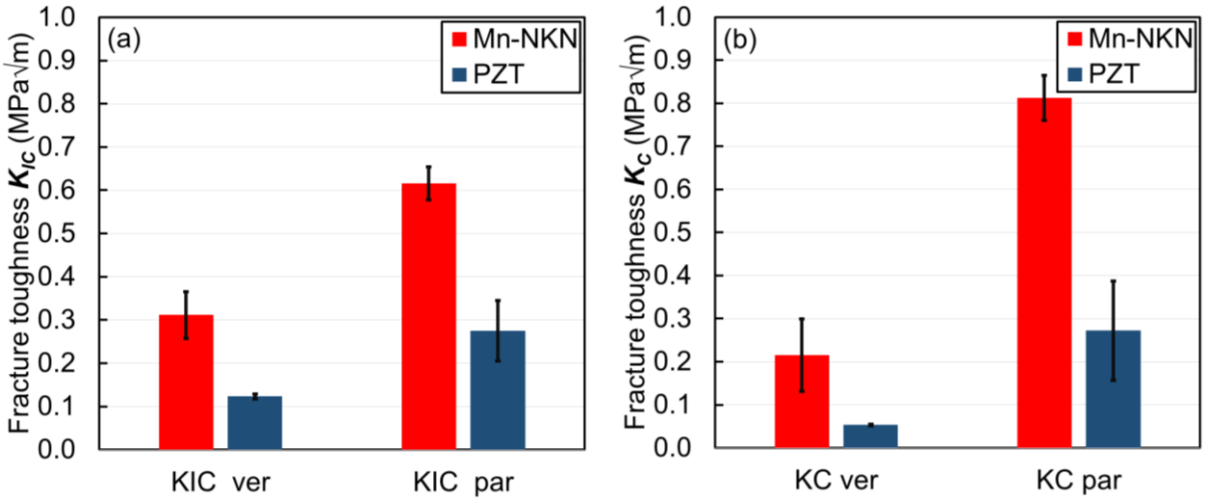

Figure 6.3: Fracture toughness K_{IC} (a) and K_C (b) for Mn-NKN and PZT before fatigue. Parallel and perpendicular direction are subjected to the poling direction.

In both cases, Mn-NKN had a higher fracture toughness than PZT in vertical as well as parallel to the poling direction. The fracture toughness KIC of Mn-NKN was estimated to be 0.3 and 0.6 MPa$\sqrt{}$m in the vertical and parallel case, respectively. A more significant difference was estimated in the case of fracture toughness KC. The values for Mn-NKN were 0.2 and 0.8 MPa$\sqrt{}$m for the vertical and parallel case respectively. The same behavior was observed for PZT, with a fracture toughness KIC and KC of 0.1 and 0.05 for the vertical case, respectively. Higher values were measured parallel to the poling direction with 0.3 for KIC as well as KC. In spite of the larger grain size and porosity, Mn-NKN showed higher resistance against crack formation. Afterwards, the samples were exposed to a unipolar electric field. Crack propagation appeared especially in PZT samples. Figure 6.4 summarizes these results.

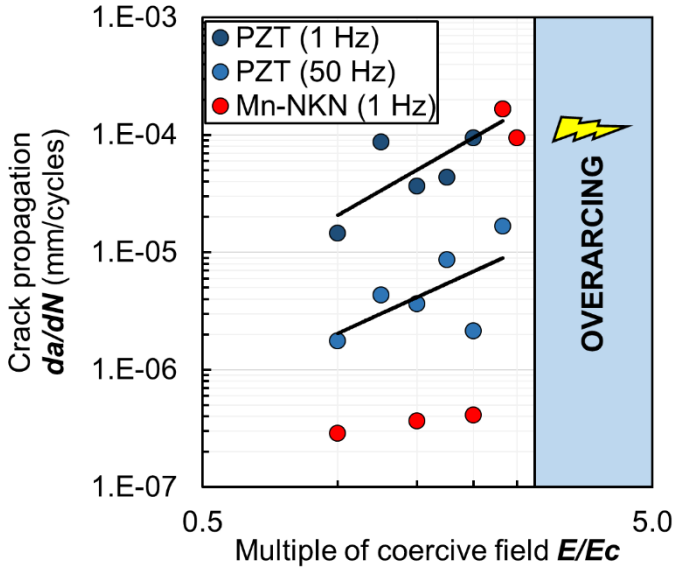

Figure 6.4: Crack propagation as a function of the multiple of the coercive field E_C for Mn-NKN and PZT at different frequencies.

The frequency dependence was only observed for PZT. With increasing frequency, the crack propagation per cycle decreased. For Mn-NKN, at frequencies of 1 Hz, the crack propagation was very low and only after electric fields of about 2.5 E_C significant crack propagation occurred. At higher frequencies no crack propagation was observed for the observed cycle numbers. Pojprapai et al. explained this behavior due to ferroelastic strain mismatch in the material. Domain reorientation causes internal stress and the crack starts propagating when the stress intensity factor reaches the critical value K_{IC}. By increasing the frequency less domain reorientation occurs and consequently less

internal stress. Hence, fatigue crack growth rates per cycle decrease with increasing cycling frequency.[107] With increasing electric field the crack propagation increased. It was shown further that Mn-NKN showed a higher resistance against crack propagation against an applied unipolar field. To explain the reason, it is necessary to compare the critical grain size for both materials. In order the estimate the critical grain size, we used equation (2.6) and (5.2) as shown in chapter 5.

Figure 6.5 shows the critical grain size as a function of the applied electric field ***E***.

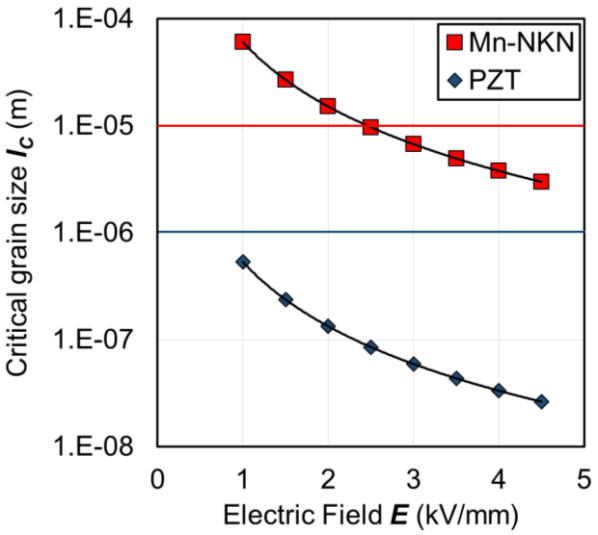

Figure 6.5: Critical grain size l_c of PZT and Mn-NKN as a function of the applied electric field ***E***. Lines represented the average grain size apparent in the respective material.

The results show that the critical grain size for PZT was for each electric field lower than the average grain size. Thus, crack propagation was observed for PZT for each condition. In contrast, Mn-NKN's critical grain size had higher values for electric fields up to 2.5 kV/mm. At ***E*** > 2.5 kV/mm the critical grain size received lower values than the average grain size. For this reason, crack propagation was observed for Mn-NKN at those electric fields.

Figure 6.6 shows an intragranular crack, which occurred in fatigued Mn-NKN ceramics at electric fields of about 2.5 kV/mm.

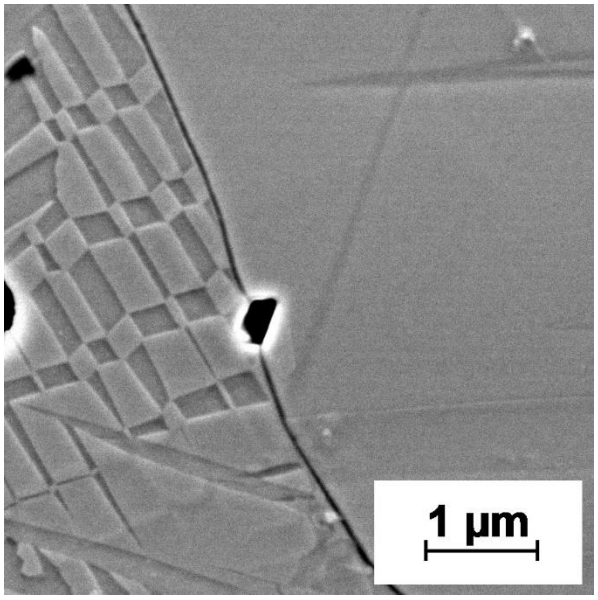

Figure 6.6: SEM-image of an intragranular crack of fatigued Mn-NKN ceramics.

It should be noted that the domain structure of PZT could not be observed, due to the small grain size. Around the crack, the domain structure appears differently than unfatigued samples. The linear structure changed to smaller domains with changing domain walls. These domain walls are characteristic for orthorhombic crystal structures. Given the fact, that domains tend to increase during unipolar fatigue tests, the changes observed are therefore considered to origin from the stress field around the crack tip. In chapter 4, it was discussed that the domain wall motion (= extrinsic contribution) had a critical effect on the mechanical properties of NKN-based ceramics. The major reason is due to the increased internal stress that is caused by the motion of domain walls. It is therefore probable that external stress switches domain walls. Compared to tetragonal crystal systems, orthorhombic crystal structures have increased switching possibilities of domain walls. For this reason, an increased amount of 60° and 120° domain walls were found at the crack. The reduction of the stress inserted by the crack is therefore more apparent in orthorhombic systems. Thus, increased K_C and K_{IC} were measured in the Mn-NKN systems, in spite of the larger grain size.

6.3 Conclusion

Crack propagation during unipolar fatigue was observed for orthorhombic Mn-NKN and tetragonal PZT. It was shown that cracks in Mn-NKN propagated less than cracks in PZT. Only at higher electric fields of about 2.5 kV/mm, crack propagation occurred. By estimating the critical grain size, it was shown that for Mn-NKN the same electric field of about 2.5 kV/mm was mandatory. Thus, the theoretical results confirmed those from the experimental procedures. PZT exhibited crack propagation at 1 kV/mm, which was also confirmed by the theoretical approach. Even though, Mn-NKN possessed a significantly higher grain size, PZT was more susceptible to mechanical degradation. Comparing both materials, the higher piezoelectric coefficients of PZT seemed to be major reason. In addition, the fracture surface energy of PZT is significantly lower than for Mn-NKN. This fact might be explained due to differences in the phase. The orthorhombic crystal structure allows for a higher number of domain walls with various angles, whereas the tetragonal phase only allows for 90° domain walls. Thus, internal stresses in the material can be better compensated if an orthorhombic phase exists. SEM images seem to confirm this behavior. An increased number of 120° and 60° domains were visible at the crack.

7 Electromechanical fatigue process under bipolar AC field

In this chapter, the bipolar fatigue behavior of NKN-based ceramics are discussed as well as the influence of temperature and pressure. For this purpose, two different materials, $Li_{0.06}Na_{0.47}K_{0.47}NbO_3$ (LNKN6) and $Na_{0.55}K_{0.45}NbO_3$ + 0.25% MnO (Mn-NKN), have been examined at various uniaxial pressures ranging from 0.1 to 100 MPa and various temperatures ranging from room temperature to 150 °C. It was shown that the harder ferroelectric Mn-NKN could maintain its piezoelectric properties at pressures up to 25 MPa. When bipolar fatigue occurred under pressures over the coercive stress of ~ 30 MPa, the sample depolarized and formed micro cracks. In contrast, the softer LNKN6 did not show fatigue at higher pressures between 25 and 50 MPa. However, in both materials, higher temperatures enhanced domain wall and charge carrier movements and conclusively domain wall pinning.

7.1 Experimental procedure

Two different materials were used for the fatigue tests, with the chemical compositions of $Li_{0.06}Na_{0.47}K_{0.47}NbO_3$ (LNKN6) and $Na_{0.55}K_{0.45}NbO_3$ + 0.25% MnO (Mn-NKN). The samples were synthesized by a mixed-oxide route, with the starting powders K_2CO_3, Na_2CO_3, Nb_2O_5 (99.9%), and Li_2CO_3 (99.8%) dried separately at 120 °C for at least 4 h to remove moisture. After weighing and mixing the powders prior to preparing each composition, they were milled with ZrO_2 balls for 16 h. For both compositions, calcination was carried out at 910 °C for 10 h and a second milling step for 16 h was performed. The calcined powders were then pressed uniaxially at 75 MPa into bars with an area of 2 x 2 mm^2 and a length l of 5 mm. Additionally, the green bodies were isostatically cold-pressed at 300 MPa before sintering at $\boldsymbol{T}$ = 1082 °C for LNKN6 and $\boldsymbol{T}$ = 1092 °C for Mn-NKN. The temperatures were held for 0.5 h at heating and cooling rates of 3 °C/min. Their bulk densities were determined by the Archimedes method. The quadratic surfaces were coated with silver and afterwards annealed at 700 °C for 5 min. Then, the samples were poled in silicone oil under an applied electrical field of E = 3 kV/mm for 30 min and temperatures of 75 and 125 °C for LNKN6 and Mn-NKN, respectively. By using different temperatures for each composition, the respective maximum piezoelectric properties could be obtained. For the fatigue tests, a sinusoidal bipolar signal with a frequency f of 50 Hz and a peak amplitude of 0.75 kV/mm, which

is equal to the coercive field E_C for LNKN6 and Mn-NKN, was applied. These fatigue tests were performed at various temperatures between room temperature and 150 °C, and pressures from 0.1 to 100 MPa. The samples were maintained under these conditions for up to approximately 10^6 cycles. To obtain reliable results on the long-term changes in the characteristics of the materials, additional experiments were carried out 48 h after the fatigue experiments. Different electrical properties were determined by the resonance and antiresonance method using an impedance analyzer (Impedance analyzer 4294A, Agilent Technologies, Santa Clara, USA). Furthermore, the relationship between the polarization *P* and the electric field *E* was investigated by determining the *P-E* hysteresis loops, using a ferroelectric tester (TF Analyzer 2000, AixAcct, Aachen, Germany) under room temperature and a measurement frequency of 1 Hz. Further tests include SEM, which required a certain preparation of the samples. The surface of the sample placed vertically in the poling direction was mechanically polished with sheets of SiC paper (#600 – #2000) and finished by polishing with colloidal silica. To determine the domain structure, the polished samples were chemically etched for 45 min with a mixture of HF: HCL: H_2O (1: 1: 18 by volume). For stress-strain measurements, a custom-made mechanical testing machine (Imoto IMC-90FB) was used. An integrated furnace enabled the tests at temperatures up to 100 °C. The pressure applied was manually increased in 5 MPa steps and the strain was noted after each step. The strain rate was estimated to be about 0.5 mm/min. To measure the strain during the compressive tests, strain gauges (Kyowa) were attached onto the samples. The signals were calibrated before each measurement and evaluated using the same software program (DCS-100A).

7.2 Results

7.2.1. Effect of voltage

Figure 7.1 (a) and (b) show the effect of the applied electric amplitude, which was in the range from 0.5 to 2 E_C, which is 0.75 kV/mm in both materials. The initial $2P_r$ values were 50 and 25 pC/N for Mn-NKN and LNKN6, respectively, and decreased over time for both materials.

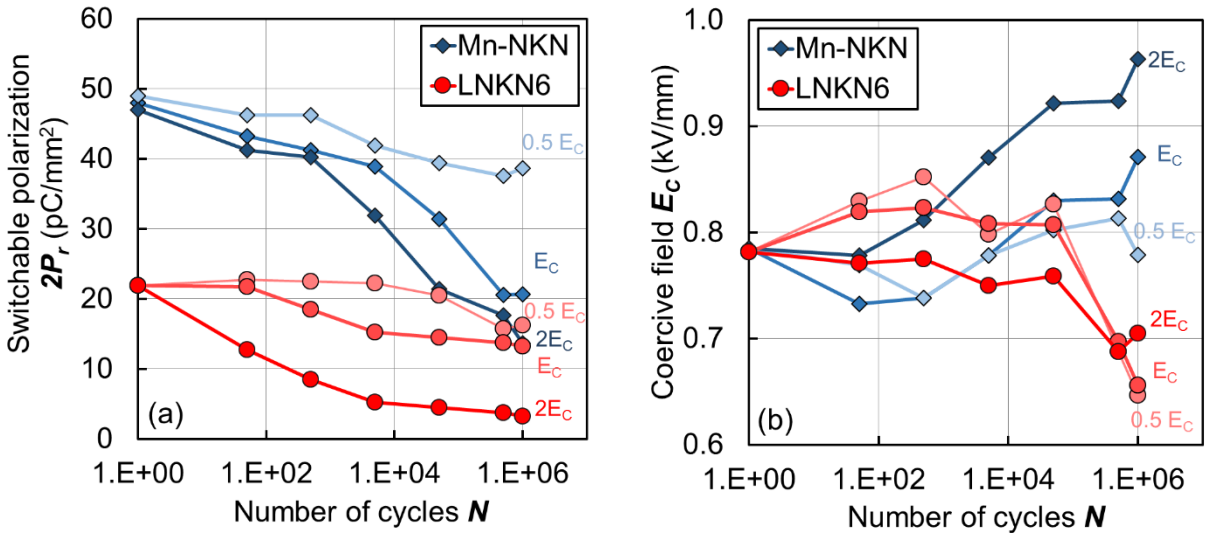

Figure 7.1: $2P_r$ (a) and E_C (b) during fatigue tests under different voltages at room temperature for Mn-NKN and LNKN6.

Significant differences were observed when the fatigue test results were compared in terms of the applied electric fields. In general, with increasing amplitude, fatigue was amplified and appeared at lower cycles. In the case of Mn-NKN, $2P_r$ degraded by about 70%, when 2 E_C was applied and decreased by 18% when the applied field is 0.5 E_C. In comparison, LNKN6 lost 90% of its $2P_r$ when an amplitude of 2 E_C was applied and 30% when 0.5 E_C was applied. In contrast, E_C changes differed between the two materials. Whereas the E_C of Mn-NKN increased maximally by 23% with increasing number of cycles and applied electric field, the E_C of LNKN6 tended to decrease under the three applied electric fields. Hereby, the end value under each condition was about 10% lower than the initial E_C.

7.2.2. Effect of pressure

To determine the effect of pressure on the fatigue behavior of lead-free alkali niobate ceramics, the experiments were carried out under a constant temperature of 25 °C. Figure 7.2 (a) and (b) show how $2P_r$ and E_c changed after 10^6 cycles at different pressures applied during the fatigue tests. In order to do so, the $2P'_r$ and E'_c of the fatigued samples were normalized by dividing them by the initial $2P_r$ and E_c, respectively.

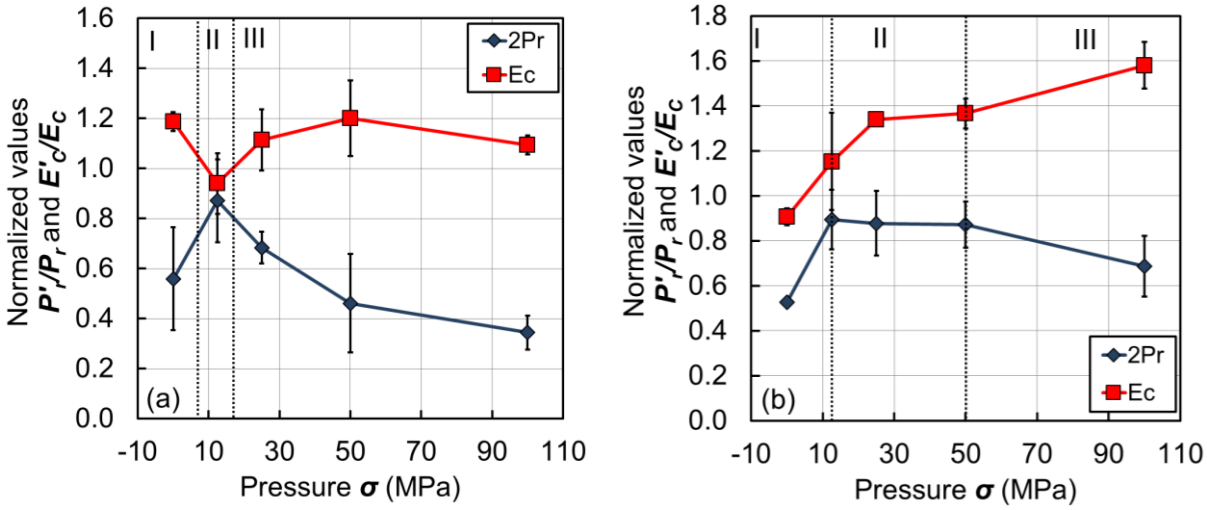

Figure 7.2: Normalized $2P'_r/2P_r$ and E'_c/E_c after 10^6 cycles under different pressures at room temperature for Mn-NKN (a) and LNKN6 (b). Areas I to III represent different mechanisms appearing in this range.

For Mn-NKN, its graph was divided into three different areas. The first area showed the fatigue behavior when no pressure was applied during the experiments. As shown before, $2P_r$ decreased whereas E_c increased. In the second area, to which approximately 12.5 MPa was applied, no marked fatigue was apparent and $2P_r$ and E_c, considering a margin of error, were comparable to their initial values. In the third area, which includes pressures higher than 25 MPa, fatigue occurred under each condition, again with decreasing $2P_r$ and increasing E_c. However, comparing these results with those of samples under no compressive stress, the changes in $2P_r$ were 60% instead of 50%. In contrast, LNKN6 samples became fatigued under each condition. Nonetheless, three areas are apparent, among which the first area ranged from 0.1 to 12.5 MPa. The largest change measured was 40%, which was observed when the samples were under no constant compressive stress. At pressures between

25 and 50 MPa, the $2P_r$ remained constant at their initial values, and E_C at an increased value. In the third area, fatigue occurred with further increasing E_C and decreasing $2P_r$.

In addition, Table 7-1 shows the alterations in the piezoelectric properties of Mn-NKN at room temperature and different pressures.

Table 7-1. Piezoelectric and dielectric values of Mn-NKN after cycles N = 10^6 under different pressures.

		12.5 MPa		25 MPa	
		10^6	Difference (%)	10^6	Difference (%)
k_{33}	0.52	0.51	**-2**	0.41	**-21**
Y_{33} (GPa)	75	75	**0**	73	**-2**
d_{33} (pC/N)	95	99	**4**	100	**5**
Maximum phase angle	75	70	**-6**	-71	**-100**
Q_m	70	68	**-2**	31	**-56**

When no compressive stress was applied, the samples depolarized and the evaluation of piezoelectric properties was impossible. At higher pressures, such as 50 and 100 MPa, the same behavior was observed. In contrast, samples under a constant pressure of 12.5 MPa showed piezoelectric characteristics. At 25 MPa, domain reorientation seemed to alter the phase angle maximum of the impedance measurements to negative values. Therefore, the calculated k_{33} and d_{33} values cannot be considered absolute results. Table 7-2 shows the changes in the piezoelectric properties of LNKN6. The impedance measurements could be carried out for samples fatigued up to 50 MPa. At higher pressures, the sample showed no resonance or antiresonance signals. This behavior was also apparent for the samples that were fatigued without an applied pressure. Note that the alterations in the material for each condition were the same.

Table 7-2. Piezoelectric and dielectric values of LNKN6 after cycles N = 10^6 under different pressures.

		12.5 MPa		25 MPa		50 MPa	
		10^6	Difference (%)	10^6	Difference (%)	10^6	Difference (%)
k_{33}	0.50	0.43	**-15**	0.45	**-10**	0.41	**-17**
Y_{33} (GPa)	80	84	**5**	83	**4**	79	**-1**
d_{33} (pC/N)	215	142	**-34**	157	**-27**	148	**-31**
Maximum phase angle	57	37	**-35**	24	**-58**	43	**-25**
Q_m	15	21	**37**	24	**60**	27	**81**

On the other hand, k_{33} and d_{33} decreased by 15 and 30% respectively, and the mechanical quality factor Q_m, as well as the Young's modulus Y, increased. Furthermore, the measured maximum phase angles were positive for each condition. Figure 7.3 shows the permittivities of both materials. Hereby, the fatigued permittivity ε'_{33} was divided by the unfatigued permittivity ε_{33}; the permittivities were 275 for Mn-NKN and 1300 for LNKN6.

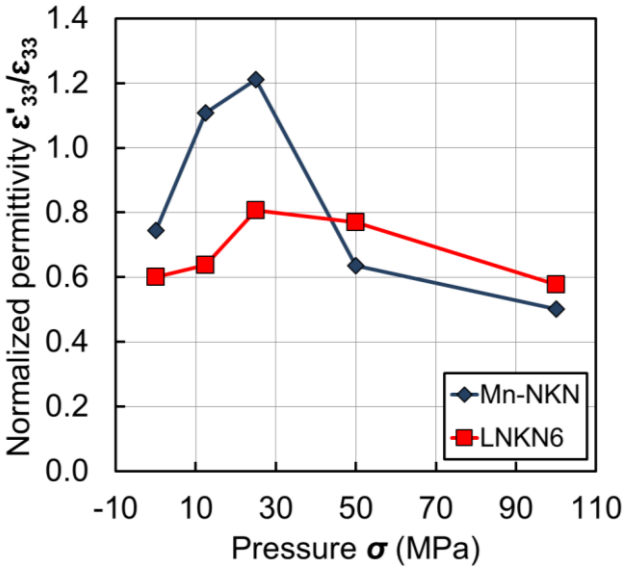

Figure 7.3: Normalized permittivity as a function of the applied pressure for Mn-NKN and LNKN6.

For Mn-NKN, the permittivity decreased at all pressures except 12.5 and 25 MPa. Hereby, a slight increase of 10% was observed. On the other hand, LNKN6 showed a decrease of at least 20% at all pressures. The highest permittivity was obtained at constant pressures of 25 and 50 MPa.

7.2.3. Effect of temperature

By keeping a constant pressure of 12.5 MPa, the temperature was increased from room temperature to 150 °C. Figure 7.4 show the changes in E_C and $2P_r$ for the experiments on E_C and $2P_r$.

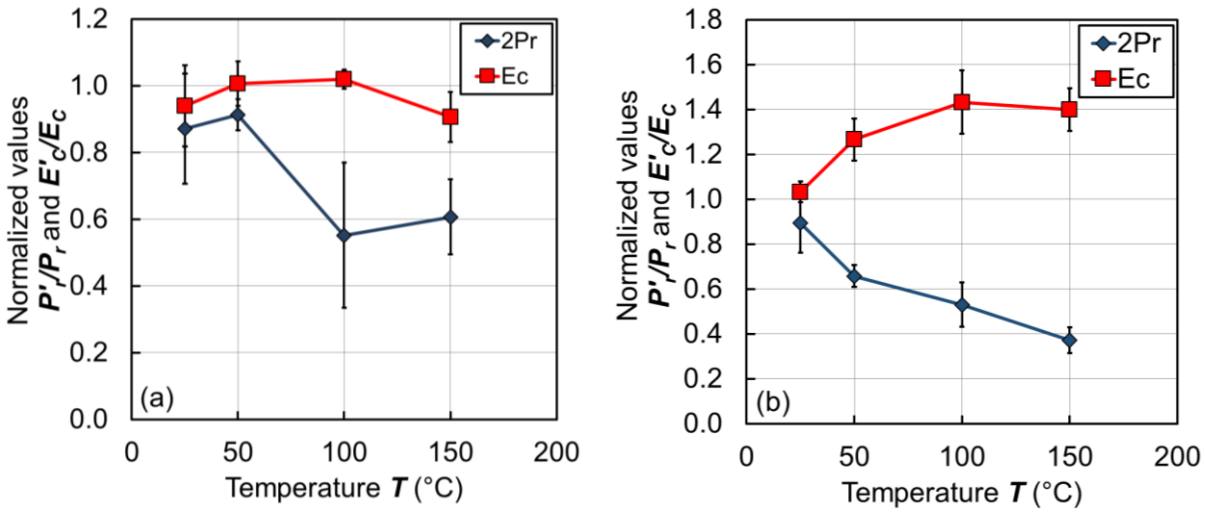

Figure 7.4: Normalized $2P'_r/2P_r$ and E'_c/E_c after 10^6 cycles under different temperatures at a constant pressure of 12.5 MPa for Mn-NKN (a) and LNKN6 (b).

E_C remained relatively constant over time at different temperatures for the Mn-NKN samples. However, $2P_r$ decreased by about 50% at temperatures higher than 100 °C. LNKN6 showed a decrease in $2P_r$ with increasing temperature. Moreover, E_C increased with increasing temperature. Table 7-3 shows a summary of the calculated values of the impedance measurements for Mn-NKN.

Table 7-3. Piezoelectric and dielectric values of Mn-NKN after cycles N = 10^6 under different temperatures.

		50 °C		100 °C		150 °C	
		10^6	Difference (%)	10^6	Difference (%)	10^6	Difference (%)
k_{33}	0.52	0.48	**-7**	0.41	**-21**	0.24	**-54**
Y_{33} (GPa)	75	73	**-3**	71	**-5**	72	**-4**
d_{33} (pC/N)	95	92	**-3**	78	**-18**	30	**-68**
Maximum phase angle	75	58.5	**-22**	-10	**-100**	-33	**-100**
Q_m	70	52	**-26**	36	**-49**	40	**-43**

Note that the piezoelectric values decreased with increasing temperature, which is particularly represented by k_{33}, which degraded by 50% at a temperature of 150 °C. Table 7-4 shows the results for the LNKN6 samples whose piezoelectric properties decreased with increasing temperature, which indicated that depolarization occurred during the fatigue tests.

Table 7-4. Piezoelectric and dielectric values of LNKN6 samples after cycles N = 10^6 under different temperatures.

		50 °C		100 °C		150 °C	
		10^6	**Difference (%)**	**10^6**	**Difference (%)**	**10^6**	**Difference (%)**
k_{33}	0.50	0.46	**-7**	0.42	**-15**	0.23	**-45**
Y_{33} (GPa)	80	79	**-2**	77	**-4**	75	**-6**
d_{33} (pC/N)	215	180	**-16**	160	**-25**	105	**-51**
Maximum phase angle	57	39	**-31**	23	**-60**	-33	**-100**
Q_m	15	10	**-31**	8	**-43**	7	**-50**

Figure 7.5 shows the normalized permittivity as a function of temperature for both materials.

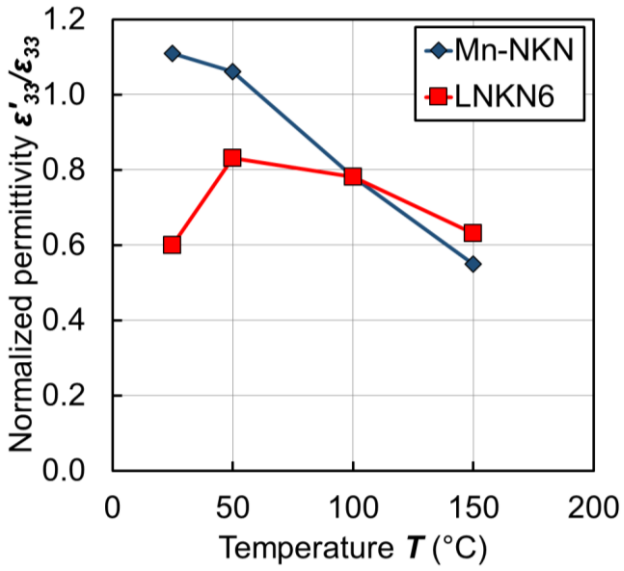

Figure 7.5: Normalized permittivity as a function of the applied temperature for Mn-NKN and LNKN6.

Mn-NKN showed an identifiable trend, whereby its permittivity decreased with increasing temperature, with the most significant change of 40% at 150 °C. The permittivity of LNKN6 decreased in general for each condition by about 20 to 40 %.

7.3 Discussion

The results of the fatigue experiments indicated that different fatigue mechanisms occurred, depending on the material and condition. Mn-NKN seemed to form micro cracks during the experiments, which is indicated by the increasing E_C. This hypothesis is further supported by the decrease in its permittivity. Micro crack formation during long-term cyclic loading is a major mechanism of fatigue generation and is mostly induced by bipolar electric fields with amplitudes high enough to induce polarization switching.[63] It was reported that severe crack growth mostly originates near the electrode[73], but preexisting micro cracks and pores[74], secondary phases[60], as well as the relief of residual stresses[75] can serve as additional sources for crack growth. The increasing crack density then results in degraded domain switching kinetics along with other factors, such as decreased permittivity.[49,108] For LNKN6, domain wall pinning seemed to have appeared, which the most observed mechanism is during the application of a bipolar cyclic electric field. Besides the continuous reorientation of the ferroelectric domains, electronic and ionic charge carriers are redistributed. Consequently, domain walls become immovable and can be described by different models.[27] Overall, domain wall pinning reduces the switchable polarization and changes the domain morphology.[69,109]

Figure 7.6 (a) – (d) show the domain structures of the unfatigued and fatigued Mn-NKN samples, respectively.

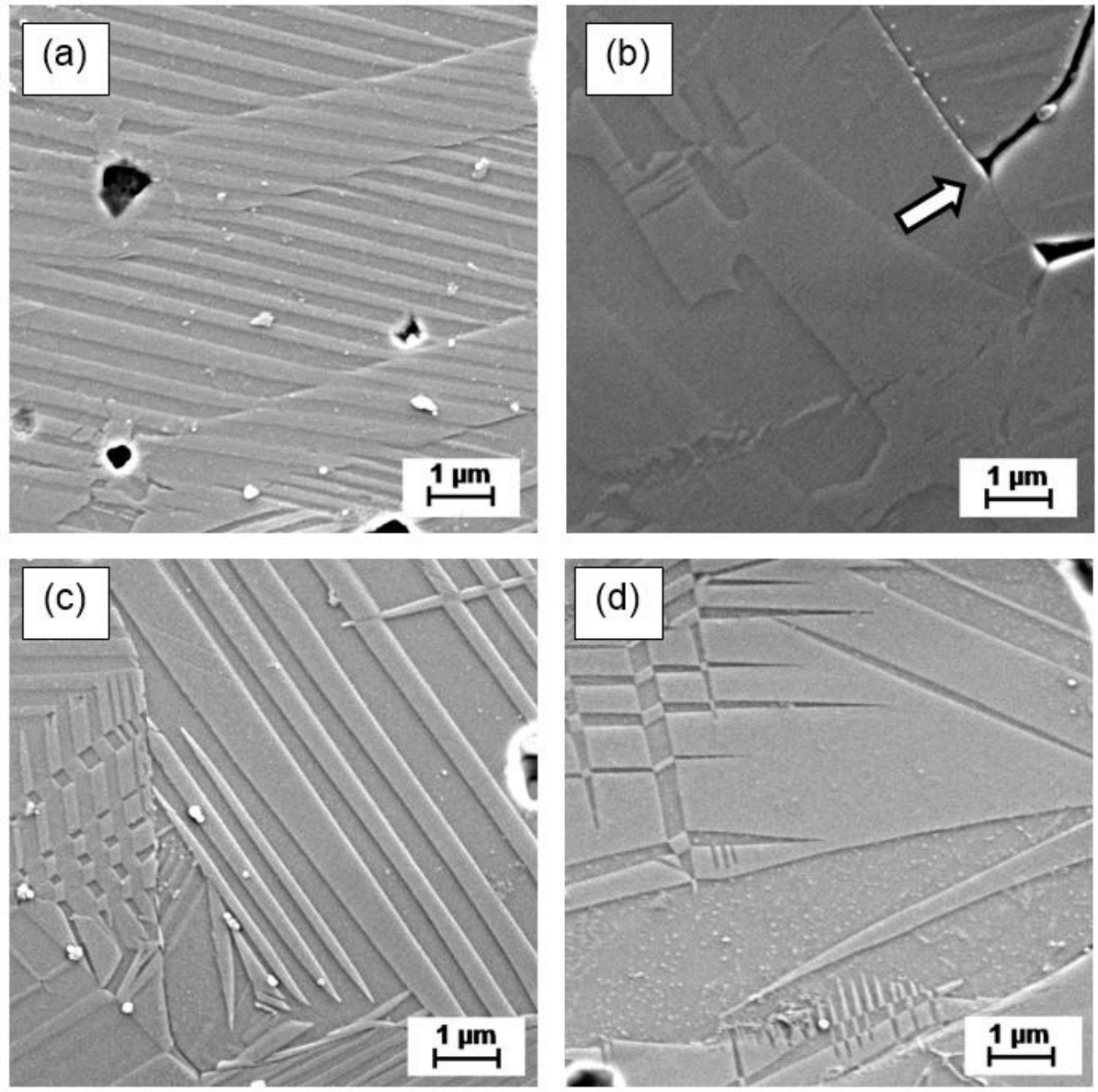

Figure 7.6: Domain structures of Mn-NKN: unfatigued (a), fatigued under room temperature and 0.1 MPa (b), fatigued under room temperature and 100 MPa (c), and fatigued under 150 °C and 12.5 MPa (d).

Poled samples show a linear structure throughout each grain. After electric fatigue took place, an increase in the domain width could be observed as well as micro cracks, which are indicated by an arrow. In addition, at higher temperatures, domains showed the same behavior. In contrast, when higher pressures were applied, the domain width remained constant, but a zig-zag structure was apparent.

Figure 7.7 (a) and (b) show summaries of the results at various domain widths. The initial domain width was about 0.7 µm for both Mn-NKN and LNKN6.

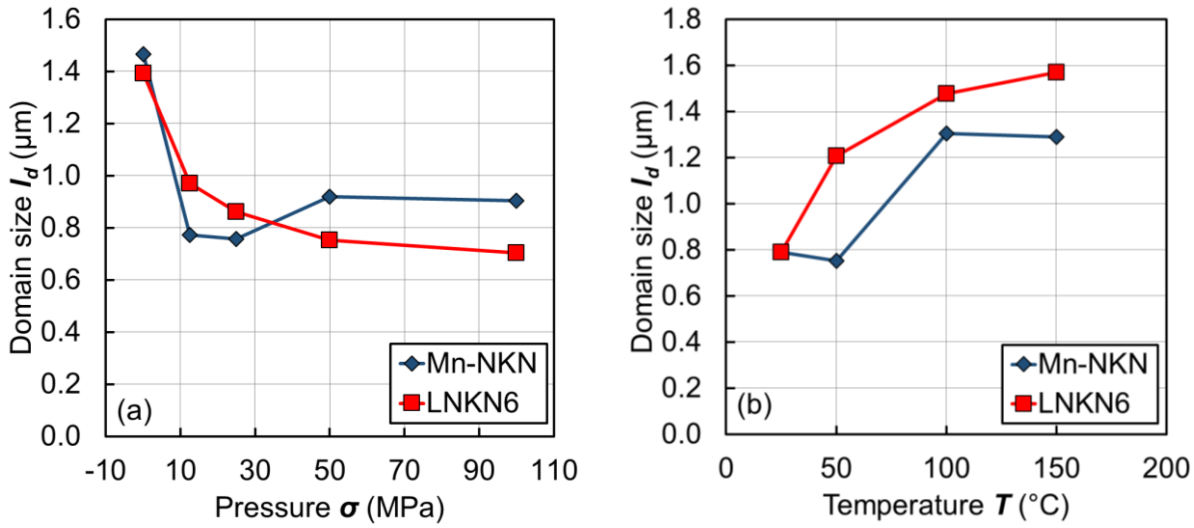

Figure 7.7: Domain width as a function of applied pressure (a) and temperature (b).

The results show the case when the domain wall pinning occurred, which is shown as an increase in domain size. As shown by Shvartsman et al.[109], the domain structure separated into a finer nanodomain structure after fatigue took place. This is due to stresses that occur between switchable and non-switchable regions. These stresses can be released by twinning of domains such that electric cycling leads to a very fine domain structure with distorted domain walls.[109] This fact was confirmed by Guo et al., who observed domain changes in-situ via TEM during bipolar fatigue.[69] Moreover, an increase in domain width has been so far only observed in unipolar fatigue tests.[14] This fine domain structure might be impossible to observe by etching techniques and therefore appear as a larger domain on SEM images. Thus, the three different areas, which were observed in both materials when a constant pressure was applied, could be explained as follows. First, Mn-NKN formed micro cracks when no pressure was applied. This formation was suppressed at a pressure of approximately 12.5 MPa. However, at higher pressures, the material seemed to form micro cracks owing to the applied compressive stress. In contrast, LNKN6 showed domain wall pinning throughout each condition. Nonetheless, with increasing pressure, this mechanism seemed to attenuate and the material seemed to start forming micro cracks at an applied stress of 100 MPa. As for increasing temperature, domain wall pinning seemed

predominate with increasing domain width. This is due to the fact that domain wall pinning is dependent on domain wall motion, and in the case of Mn-NKN, being a harder ferroelectric material, domain switching is less. Rather, domain switching is apparent, when a certain electric field is applied. In contrast, softer materials show domain switching across different electric fields. Furthermore, the thermodynamic theory predicts that polarization and E_C decrease with increasing temperature. Thus, the results suggest that E_C increases with increasing pressure. To understand further the effects of pressure and temperature on these fatigue mechanisms, stress strain curves were evaluated for the samples under different temperatures. The results are shown in Figure 7.8 (a) and (b).

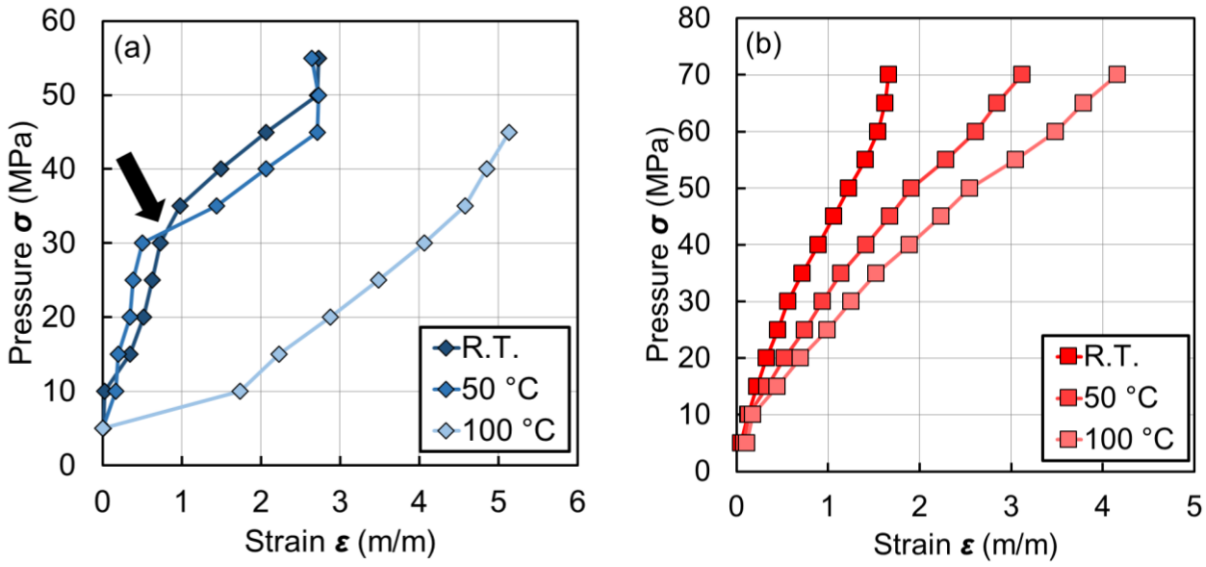

Figure 7.8: Stress-strain curves of Mn-NKN (a) and LNKN6 (b) under different temperatures.

Mn-NKN showed a deviating stress strain curve at room temperature and 50 °C. This behavior is due to domain switching, which starts appearing after a certain compressive stress is applied. The affected point of application is indicated by an arrow, and is called coercive stress.[110] At a temperature of about 100 °C, this affected point vanished and Mn-NKN showed a linear behavior. Even at lower temperatures, LNKN6 showed a linear behavior, which indicated that domain movement appeared at different pressures. This behavior is caused by the soft ferroelectric nature of LNKN6, where the polarization gradually changes with increasing electric field. Thus, domain movement enhanced with increasing temperature and finally domain wall pinning. On

the other hand, compressive stress suppresses domain switching and domain wall pinning, and reduces micro crack formation as well.

7.4. Conclusion

The effects of voltage, pressure, and temperature on the bipolar fatigue behavior of alkali-niobate-based ceramics have been examined. Soft LNKN6 as well as hard Mn-NKN were observed. It was shown that both materials had different predominant fatigue mechanisms. Whereas LNKN6 fatigue occurred with domain wall pinning, micro crack formation occurred in Mn-NKN. These fatigue mechanisms increased with increasing electric field. However, when a certain pressure was applied, these mechanisms were attenuated. Because Mn-NKN is a hard ferroelectric, domain switching does not appear at low electric fields or under compressive stresses. For this reason, at low pressures, the piezoelectric properties were also unchanged after the fatigue experiments. However, at a pressure of 50 MPa, which is higher than the coercive stress, the sample became unpoled. Domain wall pinning did not occur under this condition, because the pressure seemed to decrease domain movement. However, owing to the increase in E_C, micro crack formation cannot be ruled out at higher pressures. In comparison, LNKN6 showed degradations of the piezoelectric properties under each condition. This could be due to the soft ferroelectric characteristics and the domain switching occurring at low pressures and electric fields. For this reason, domain wall pinning as well as domain switching through applied stress could have occurred during fatigue tests. Different temperatures had different effects on the Mn-NKN samples. Up to 50 °C, domain wall pinning was still suppressed, as shown by the unaltered domain size. At higher temperatures, domain wall pinning seemed to be predominant. Fatigue started to occur in LNKN6 even at low temperatures, and domain wall pinning became predominant with increasing temperature.

8 Summary and conclusion

The first objective was to determine the mechanical properties of lead-free alkali niobate ceramics. It was shown that NKN-based ceramics showed similar flexural strength in the unpoled state. Noteworthy is the fact that during polarization, the mechanical properties could be further improved. In contrast, PZT samples showed so far only mechanical degradation after poling. By observing to contrasting cases in LNKN4 and LNKN6, we were able to examine the possible causes. LNKN4 showed even after low field polarization a decrease in flexural strength, whereas LNKN6 improved even at high electric fields. The main reason was the difference in the intrinsic extrinsic contribution ratio. Higher extrinsic contribution, as shown by LNKN4, increased the internal stress in the sample, thereby causing enhanced crack propagation perpendicular to its polarization. Due to a lower extrinsic contribution, LNKN6 showed improved mechanical and piezoelectric properties and was therefore used in further experiments.

The second objective of this work was the observation of the fatigue behavior under unipolar AC-field. We compared two samples with LNKN6-basis. Pure LNKN6 (LNKN6-a) showed higher fatigue behavior than LNKN6 with additives (LNKN6-b). Crack formation occurred in LNKN6-a due to increased grain size compared to LNKN6-b. Increasing temperature decreased the crack density in the sample. The results for LNKN6-a also suggested that through phase transformation from tetragonal to orthorhombic, the crack density decreased. The orthorhombic phase has an increased amount of domain walls, such as 60°, 90° and 120°, compared to the tetragonal phase with only 90°. In order to decrease the stress from domain switching, the orthorhombic phase increased and allowed for more switching possibilities. On the other hand, LNKN6-b showed a higher electric bias field, which is caused by charge carrier accumulation. This accumulation is a common fatigue mechanism during unipolar fatigue and is caused by oxygen vacancies and other charge carriers in the sample. Because of the additives, space charge carriers in the sample are increased and thus fatigue by space charge accumulation as well. Noteworthy is the fatigue free behavior of LNKN6-b at 50 °C, which is made possible by phase transformation from orthorhombic to tetragonal. XRD results did not show that phase transformation took place in the material during fatigue. However, it is quite possible that phase transformation and the occurring fatigue mechanisms were in an energy equilibrium at

50 °C. Overall, it seemed that orthorhombic and tetragonal phase were in a local energy minimum in both samples. Depending on temperature and the predominant fatigue mechanism the material shifted to orthorhombic or tetragonal phase transformation.

In order to investigate the hypothesis, that the orthorhombic phase is more resistant against crack formation and propagation, further experiments were conducted By comparing pure orthorhombic material (Mn-NKN) and pure tetragonal material (PZT) for its fracture toughness, and crack propagation during unipolar cycling. It was shown that cracks in Mn-NKN propagated less than cracks in PZT. Only at higher electric fields of about 2.5 kV/mm, crack propagation occurred. By estimating the critical grain size, it was shown that for Mn-NKN the same electric field of about 2.5 kV/mm was mandatory. Thus, the theoretical results confirmed those from the experimental procedures. PZT exhibited crack propagation at 1 kV/mm, which was also confirmed by the theoretical approach. Even though, Mn-NKN possessed a significantly higher grain size, PZT was more susceptible to mechanical degradation. Comparing both materials, the higher piezoelectric coefficients of PZT seemed to be major reason. In addition, the fracture surface energy of PZT is significantly lower than for Mn-NKN. This fact might be explained due to differences in the phase. The orthorhombic crystal structure allows for a higher number of domain walls with various angles, whereas the tetragonal phase only allows for 90° domain walls. Thus, internal stresses in the material can be better compensated if an orthorhombic phase exists. SEM images seem to confirm this behavior. An increased number of 120° and 60° domains were visible at the crack.

In the last point, we concentrated on the bipolar fatigue behavior of LNKN6 in comparison to a hard ferroelectric material, Mn-NKN. Like unipolar fatigue, the two materials had different predominant fatigue mechanisms. Domain wall pinning occurred predominantly in LNKN6, whereas micro crack formation was mostly observed in Mn-NKN. These fatigue mechanisms increased with increasing electric field. Temperature increased domain wall pinning, but decreased micro crack formation. Up to 50 °C, domain wall pinning was still suppressed in Mn-NKN, as shown by the unaltered domain size. At temperatures > 50 °C, domain wall pinning seemed to be predominant. Fatigue started to occur in LNKN6 even at low temperatures, and domain wall pinning increased with increasing temperature. When a certain pressure was applied, these mechanisms were attenuated. Because Mn-NKN is a hard

ferroelectric, domain switching does not appear at low electric fields or under compressive stresses. For this reason, at low pressures, the piezoelectric properties were also unchanged after the fatigue experiments. At a pressure of 50 MPa, which is higher than the coercive stress, the sample became unpoled. Domain wall pinning did not occur under this condition, because the pressure seemed to decrease domain movement. However, owing to the increase in E_C, micro crack formation cannot be ruled out at higher pressures for Mn-NKN. In comparison, LNKN6 showed degradations of the piezoelectric properties under each condition. This could be due to the soft ferroelectric characteristics and the domain switching occurring at low pressures and electric fields. For this reason, domain wall pinning as well as domain switching through applied stress could have occurred during fatigue tests.

In conclusion, lead-free alkali niobate ceramics show improved mechanical properties compared to PZT after poling. This is important, as actuators are used under mechanical stress. Especially LNKN6, with its high piezoelectric and mechanical properties seemed to be promising. However, unipolar fatigue tests showed that micro crack formation is a problem and lowers the mechanical properties. This problem could be counteracted by changing the grain size in the material. Another problem is that pure LNKN6 is a soft ferroelectric material. Thus, even at low pressures the material would become unpoled during application. Dopants, such as MnO_2, which would increase the hardness of the ferroelectric properties, might be the solution to this problem. However, doping also increases the amount of charge carriers in the material and therefore domain wall pinning. Furthermore, even though LNKN6 possess a high Curie temperature, the phase transformation from orthorhombic to tetragonal seemed to play an important role during fatigue. The phase transition temperature $T_{O\text{-}T}$ was for our experiments about 50 °C. At this temperature, improved fatigue resistance was observed. This would suggest, that by changing the phase transition temperature, NKN-based materials could be adapted to the operating temperature of an application. Therefore, LNKN6 is still an interesting character, but needs to be adjusted through dopants, if used in industrial applications.

References

1. Statistics of global shipments of electronic components. *Japan Electronics and Information Technology Association* (2015). at <http://home.jeita.or.jp/>
2. Huber, J. E., Fleck, N. A. & Ashby, M. F. The selection of mechanical actuators. *Proc. R. Soc. London A* **453,** 2185–2205 (1997).
3. Zupan, M., Ashby, M. F. & Fleck, N. Actuator classification and selection - The development of a database. *Adv. Eng. Mater.* **4,** 933–940 (2002).
4. Aksel, E. & Jones, J. L. Advances in lead-free piezoelectric materials for sensors and actuators. *Sensors* **10,** 1935–1954 (2010).
5. Genenko, Y. A., Glaum, J., Hoffmann, M. J. & Albe, K. Mechanisms of aging and fatigue in ferroelectrics. *Mater. Sci. Eng. B* **192,** 52–82 (2015).
6. Lupascu, D. & Rödel, J. Fatigue in bulk lead zirconate titanate actuator materials. *Adv. Eng. Mater.* **7,** 882–898 (2005).
7. Saito, Y. *et al.* Lead-free piezoceramics. *Nature* **432,** 84 – 87 (2004).
8. Priya, S. & Nahm, S. *Lead-free piezoelectrics*. (Springer, 2012). doi:10.1017/CBO9781107415324.004
9. Jaffe, B., Cook, W. R. & Jaffe, H. *Piezoelectric ceramics*. *Piezoelectric Ceramics* (Academic Press, 1971). doi:10.1016/B978-0-12-379550-2.50002-8
10. Lines, M. E. & Glass, A. M. *Principles and applications of ferroelectrics and related materials*. (Oxford University Press, 1977). doi:10.1093/acprof:oso/9780198507789.001.0001
11. Moulson, A. J. & Herbert, J. M. *Electroceramics: Materials, Properties, Applications*. (John Wiley & Sons, 2003).
12. Senousy, M. S., Rajapakse, R. K. N. D., Mumford, D. & Gadala, M. S. Self-heat generation in piezoelectric stack actuators used in fuel injectors. *Smart Mater. Struct.* **18,** 045008 (2009).
13. Zhao, G.-L., Zhang, H., Zhang, B.-P. & Li, J.-F. Sintering and electrical properties of Cu-particle-dispersed (Na,K,Li)NbO3. *Ceram. Int.* **36,** 583–587 (2010).
14. Guo, Y., Kakimoto, K. & Ohsato, H. Phase transitional behavior and piezoelectric properties of (Na0.5K0.5)NbO3-LiNbO3 ceramics. *Appl. Phys. Lett.* **85,** 4121 – 4123 (2004).
15. Matsubara, M., Yamaguchi, T., Kikuta, K. & Hirano, S. Effect of Li Substitution on the piezoelectric properties of potassium sodium niobate ceramics. *Jpn. J. Appl. Phys.* **44,** 6136–6142 (2005).
16. Tsurekawa, S., Hatao, H., Takahashi, H. & Morizono, Y. Changes in ferroelectric domain structure with electric fatigue in Li0.06(Na0.5K0.5)0.94NbO3 ceramics. *Jpn. J. Appl. Phys.* **50,** 09NC02 (2011).
17. Zhang, S., Xia, R., Hao, H., Liu, H. & Shrout, T. R. Mitigation of thermal and fatigue behavior in K(0.5)Na(0.5)NbO(3)-based lead free piezoceramics. *Appl. Phys. Lett.* **92,** 152904–1529043 (2008).

18. Hao, J., Xu, Z., Chu, R., Li, W. & Fu, P. Good temperature stability and fatigue-free behavior in Sm2O3-modified 0.948(K0.5Na0.5)NbO3–0.052LiSbO3 lead-free piezoelectric ceramics. *Mater. Res. Bull.* **65,** 94–102 (2015).

19. Patterson, E. & Cann, D. Piezoelectric properties and unipolar fatigue behavior of KNN-based Pb-free piezoceramics. *IEEE Trans. Ultrason. Ferroelectr. Freq. Control* **58,** 1835–1841 (2011).

20. Yao, F. Z. *et al.* Fatigue-free unipolar strain behavior in CaZrO3 and MnO2 co-modified (K,Na)NbO3-based lead-free piezoceramics. *Appl. Phys. Lett.* **103,** 192907 (2013).

21. Yao, F.-Z. *et al.* Nanodomain engineered (K, Na)NbO 3 lead-free piezoceramics - Enhanced thermal and cycling reliabilities. *J. Am. Ceram. Soc.* **98,** 448–454 (2015).

22. Zhang, H. *et al.* Reliability enhancement in nickel-particle-dispersed alkaline niobate piezoelectric composites and actuators. *J. Eur. Ceram. Soc.* **31,** 795–800 (2011).

23. Shen, Z.-Y. *et al.* Electrical and mechanical properties of fine-grained Li/Ta-modified (Na,K)NbO 3 -based piezoceramics prepared by spark plasma sintering. *J. Am. Ceram. Soc.* **1383,** 1378–1383 (2010).

24. Yilmaz, E. D., Mgbemere, H. E., Özcoban, H., Fernandes, R. P. & Schneider, G. Investigation of fracture toughness of modified (KxNa1−x)NbO3 lead-free piezoelectric ceramics. *J. Eur. Ceram. Soc.* **32,** 3339–3344 (2012).

25. Fett, T., Munz, D. & Thun, G. Bending strength of a PZT ceramic under electric fields. *J. Eur. Ceram. Soc.* **23,** 195–202 (2003).

26. Fu, R. & Zhang, T.-Y. Influences of temperature and electric Field on the bending strength of lead zirconate titanate ceramics. *Acta Mater.* **48,** 1729–1740 (2000).

27. Glaum, J. & Hoffman, M. Electric fatigue of lead-free piezoelectric materials. *J. Am. Ceram. Soc.* **97,** 665–680 (2014).

28. Matthias, B. T. & Remeika, J. P. Dielectric Properties of Sodium and Potassium Niobates. *Phys. Rev.* **82,** 727–729 (1951).

29. Jaeger, R. E. & Egerton, L. Hot pressing of potassium-sodium niobates. *J. Am. Ceram. Soc.* **45,** 209–213 (1962).

30. Egerton, L. & Dillon, D. M. Piezoelectric and dielectric properties of ceramics in the system potassium-sodium niobate. *J. Am. Ceram. Soc.* **42,** 438 –442 (1959).

31. Wada, S., Seike, A. & Tsurumi, T. Poling treatment and piezoelectric properties of potassium niobate ferroelectric single crystals. *Japanese J. Appl. Physics, Part 1 Regul. Pap. Short Notes Rev. Pap.* **40,** 5690–5697 (2001).

32. Ahn, C. W., Park, C. S., Dittmer, R., Hong, S. H. & Priya, S. Effect of elemental diffusion on temperature coefficient of piezoelectric properties in KNN-based lead-free composites. *J. Mater. Sci.* **45,** 3961–3965 (2010).

33. Guo, Y., Kakimoto, K. & Ohsato, H. Structure and electrical properties of lead-free (Na0.5K0.5)NbO3-BaTiO3 ceramics. *Jpn. J. Appl. Phys.* **43,** 6662–6666 (2004).

34. Zuo, R., Ye, C. & Fang, X. Na0.5K0.5NbO3–BiFeO3 lead-free piezoelectric ceramics. *J. Phys. Chem. Solids* **69,** 230–235 (2008).

35. Ming, B.-Q., Wang, J.-F., Qi, P. & Zang, G.-Z. Piezoelectric properties of (Li, Sb, Ta) modified (Na,K)NbO3 lead-free ceramics. *J. Appl. Phys.* **101,** 054103 (2007).

36. Ahn, C. W. *et al.* Correlation between phase transitions and piezoelectric properties in lead-free (K,Na,Li)NbO3-BaTiO3 ceramics. *Jpn. J. Appl. Phys.* **47,** 8880–8883 (2008).

37. Du, H. *et al.* An approach to further improve piezoelectric properties of (K0.5Na0.5)NbO3-based lead-free ceramics. *Appl. Phys. Lett.* **91,** 202907 (2007).

38. Ahn, C. W., Choi, C. H., Park, H. Y., Nahm, S. & Priya, S. Dielectric and piezoelectric properties of (1-x)(Na0.5K0.5)NbO3 - xBaTiO3 ceramics. *J. Mater. Sci.* **43,** 6784–6797 (2008).

39. Haertling, G. H. Properties of hot-pressed ferroelectric alkali niobate ceramics. *J. Am. Ceram. Soc.* **50,** 329–330 (1967).

40. Ahn, C. W. *et al.* Effect of CuO and MnO2 on sintering temperature, microstructure, and piezoelectric properties of 0.95(K0.5Na0.5)NbO3-0.05BaTiO3 ceramics. *Mater. Lett.* **62,** 3594–3596 (2008).

41. Mgbemere, H. E., Herber, R.-P. & Schneider, G. A. Effect of MnO2 on the dielectric and piezoelectric properties of alkaline niobate based lead free piezoelectric ceramics. *J. Eur. Ceram. Soc.* **29,** 1729–1733 (2009).

42. Carl, K. & Hardtl, K. H. Electrical after-effects in Pb(Ti, Zr)O3 ceramics. *Ferroelectrics* **17,** 473–486 (1977).

43. Zhang, L. X. & Ren, X. In situ observation of reversible domain switching in aged Mn-doped BaTiO3 single crystals. *Phys. Rev. B - Condens. Matter Mater. Phys.* **71,** 1–8 (2005).

44. Ren, X. Large electric-field-induced strain in ferroelectric crystals by point-defect-mediated reversible domain switching. *Nat. Mater.* **3,** 91–94 (2004).

45. Postnikov, V. S., Pavlov, V. S. & Turkov, S. K. Internal friction in ferroelectrics due to interaction of domain boundaries and point defects. *J. Phys. Chem. Solids* **3,** 1785 – 1791 (1970).

46. Balke, N., Lupascu, D. C., Granzow, T. & Rödel, J. Fatigue of lead zirconate titanate ceramics. I: Unipolar and DC loading. *J. Am. Ceram. Soc.* **90,** 1081–1087 (2007).

47. Balke, N., Granzow, T. & Rödel, J. Degradation of lead-zirconate-titanate ceramics under different dc loads. *J. Appl. Phys.* **105,** (2009).

48. Wang, D., Fotinich, Y. & Carman, G. P. Influence of temperature on the electromechanical and fatigue behavior of piezoelectric ceramics. *J. Appl. Phys.* **83,** 5342–5350 (1998).

49. Luo, Z. *et al.* Bipolar and unipolar fatigue of ferroelectric BNT-based lead-free piezoceramics. *J. Am. Ceram. Soc.* **94,** 529–535 (2011).

50. Nuffer, J., Lupascu, D. C. & Rödel, J. Damage evolution in ferroelectric PZT

induced by bipolar electric cycling. *Acta Mater.* **48,** 3783–3794 (2000).

51. Nejezchleb, K., Kroupa, F., Boudys, M. & Zelenka, J. Poling process, microcracks, and mechanical quality of PZT ceramics. *Ferroelectrics* **81,** 1303–1306 (1988).

52. Shin, B.-C. & Kim, H.-G. Grain-size dependence of electrically induced microcracking in $BaTiO_3$ ceramics. *Ferroelectrics* **100,** 209–212 (1989).

53. Chung, H. T. & Kim, H. G. Characteristics of domain in tetragonal phase PZT ceramics. *Ferroelectrics* **76,** 327–333 (1987).

54. Shin, B.-C. & Kim, H.-G. Partial discharge, microcracking, and breakdown in BaTiO 3 ceramics. *Ferroelectrics* **77,** 161–166 (1988).

55. Subbarao, E. C., Srikanth, V., Cao, W. & Cross, L. E. Domain switching and microcracking during poling of lead zirconate titanate ceramics. *Ferroelectrics* **145,** 271–281 (1993).

56. Chung, H.-T., Shin, B.-C. & Kim, H.-G. Grain-size dependence of electrically induced microcracking in ferroelectric ceramics. *J. Am. Ceram. Soc.* **72,** 327–329 (1989).

57. Jiang, Q., Subbarao, E. C. & Cross, L. E. Grain size dependence of electric fatigue behavior of hot pressed PLZT ferroelectric ceramics. *Acta Metall. Mater.* **42,** 3687–3694 (1994).

58. Jiang, Q., Cao, W. & Cross, L. E. Electric fatigue in lead zirconate titanate ceramics. *J. Am. Ceram. Soc.* **77,** 211–215 (1994).

59. Kim, S.-J. & Jiang, Q. Microcracking and electric fatigue of polycrystalline ferroelectric ceramics. *Smart Mater. Struct.* **5,** 321–326 (1996).

60. Hill, M. D., White, G. S., Hwang, C.-S. & Lloyd, I. K. Cyclic Damage in Lead Zirconate Titanate. *J. Am. Ceram. Soc.* **79,** 1915–1920 (1996).

61. Zhu, T., Fang, F. E. I. & Yang, W. E. I. Fatigue crack growth in ferroelectric ceramics below the coercive field. *Ferroelectrics* **18,** 1025 – 1027 (1999).

62. Cao, H. & Evans, A. G. Electric-field-induced fatigue crack growth in piezoelectrics. *J. Am. Ceram. Soc.* **77,** 1783–1786 (1994).

63. Weitzing, H., Schneider, G., Steffens, J., Hammer, M. & Hoffmann, M. Cyclic fatigue due to electric loading in ferroelectric ceramics. *J. Eur. Ceram. Soc.* **19,** 1333–1337 (1999).

64. Schneider, G., Felten, F. & McMeeking, R. M. The electrical potential difference across cracks in PZT measured by Kelvin probe microscopy and the implications for fracture. *Acta Mater.* **51,** 2235–2241 (2003).

65. Kerkamm, I., Hiller, P., Granzow, T. & Rödel, J. Correlation of small- and large-signal properties of lead zirconate titanate multilayer actuators. *Acta Mater.* **57,** 77–86 (2009).

66. Wang, H., Wereszczak, A. a. & Lin, H.-T. Fatigue response of a PZT multilayer actuator under high-field electric cycling with mechanical preload. *J. Appl. Phys.* **105,** 014112 (2009).

67. Nuffer, J., Lupascu, D. C. & Rödel, J. Stability of pinning centers in fatigued lead–zirconate–titanate. *Appl. Phys. Lett.* **80,** 1049 (2002).

68. Warren, W. L. *et al.* Polarization suppression in Pb(Zr,Ti)O3 thin films. *J. Appl. Phys.* **77,** 6695 (1995).

69. Guo, H., Liu, X., Rödel, J. & Tan, X. Nanofragmentation of ferroelectric domains during polarization fatigue. *Adv. Funct. Mater.* **25,** 270–277 (2015).

70. Verdier, C., Morrison, F. D., Lupascu, D. C. & Scott, J. F. Fatigue studies in compensated bulk lead zirconate titanate. *J. Appl. Phys.* **97,** 024107 (2005).

71. Larsen, P. K., Dormans, G. J. M., Taylor, D. J. & van Veldhoven, P. J. Ferroelectric properties and fatigue of PbZr0.51Ti0.49O3 thin films of varying thickness: Blocking layer model. *J. Appl. Phys.* **76,** 2405 (1994).

72. Lee, J. J., Thio, C. L. & Desu, S. B. Electrode contacts on ferroelectric Pb(ZrxTi1−x)O3 and SrBi2Ta2O9 thin films and their influence on fatigue properties. *J. Appl. Phys.* **78,** 5073 (1995).

73. Dos Santos E Lucato, S. L., Lupascu, D. C., Kamlah, M., Rödel, J. & Lynch, C. S. Constraint-induced crack initiation at electrode edges in piezoelectric ceramics. *Acta Mater.* **49,** 2751–2759 (2001).

74. Nuffer, J., Lupascu, D. C., Glazounov, A., Kleebe, H. J. & Rödel, J. Microstructural modifications of ferroelectric lead zirconate titanate ceramics due to bipolar electric fatigue. *J. Eur. Ceram. Soc.* **22,** 2133–2142 (2002).

75. Hall, D. A., Mori, T., Comyn, T. P., Ringgaard, E. & Wright, J. P. Residual stress relief due to fatigue in tetragonal lead zirconate titanate ceramics. *J. Appl. Phys.* **114,** 024103 (2013).

76. Balke, N., Lupascu, D. C., Blair, T. & Gruverman, A. Thickness profiles through fatigued bulk ceramic lead zirconate titanate. *J. Appl. Phys.* **100,** 114117 (2006).

77. Yang, G., Yue, Z., Ji, Y., Chu, X. & Li, L. Improvement of fatigue resistance for multilayer lead zirconate titanate (PZT)-based ceramic actuators by external mechanical loads. *J. Appl. Phys.* **104,** 126103 (2008).

78. Gross, D. & Seelig, T. *Fracture mechanics : With an introduction to micromechanics*. *Journal of Chemical Information and Modeling* **53,** (Springer, 2006).

79. Lawn, B., Evans, A. & Marschall, D. Elastic/plastic indentation damage in ceramics: the median/radial crack system. *J. Am. Ceram. Soc.* **63,** 574–581 (1980).

80. Shindo, Y., Oka, M. & Horiguchi, K. Analysis and Testing of Indentation Fracture Behavior of Piezoelectric Ceramics Under an Electric Field. *J. Eng. Mater. Technol.* **123,** 293 (2001).

81. Park, S. & Sun, C. Fracture criteria for piezoelectric ceramics. *J. Am. Ceram. Soc.* **78,** 1475–1480 (1995).

82. Yang, W., Fang, F. & Tao, M. Critical role of domain switching on the fracture toughness of poled ferroelectrics. *Int. J. Solids Struct.* **38,** 2203–2211 (2001).

83. Fu, J., Zuo, R. Z. & Liu, Y. X-ray analysis of phase coexistence and electric poling processing in alkaline niobate-based compositions. *J. Alloys Compd.* **493,** 197–201 (2010).

84. Roisnel, T. & Rodríquez-Carvajal, J. WinPLOTR: A windows tool for powder diffraction pattern analysis. *Mater. Sci. Forum* **378-381,** 118–123 (2001).

85. Hatano, K. *et al.* Polarization system and phase transition on (Li,Na,K)NbO3 ceramics. *Jpn. J. Appl. Phys.* **49,** 1–5 (2010).

86. Wang, K. & Li, J.-F. Analysis of crystallographic evolution in (Na,K)NbO3-based lead-free piezoceramics by x-ray diffraction. *Appl. Phys. Lett.* **91,** 262902 (2007).

87. Lente, M. H. & Eiras, J. A. 90° Domain reorientation and domain wall rearrangement in lead zirconate titanate ceramics characterized by transient current and hysteresis loop measurements. *J. Appl. Phys.* **89,** 5093–5099 (2001).

88. Kobayashi, K., Mizuno, Y., Hatano, K. & Randall, C. A. Rayleigh behavior in the lead free piezoelectric Lix(Na0.5K0.5)1-xNbO3 ceramic. *Appl. Phys. Express* **5,** 31501 (2012).

89. Ogawa, T., Ishii, K., Matsumoto, T. & Nishina, T. Poling field dependence of longitudinal and transverse wave velocities, Young's modulus, and Poisson's ratio in piezoelectric ceramics. *Jpn. J. Appl. Phys.* **51,** 09LD03 (2012).

90. Schneider, G. A. Influence of electric field and mechanical stresses on the fracture of ferroelectrics. *Annu. Rev. Mater. Res.* **37,** 491–538 (2007).

91. Engert, A. R. *et al.* Influence of small cyclic and DC electrical loads on the fracture toughness of ferroelectric ceramics. *J. Eur. Ceram. Soc.* **31,** 531–540 (2011).

92. Jin, D., Chen, X. & Xu, Z. Influence of dispersed coarse grains on mechanical and piezoelectric properties in (Bi0.5Na0.5)TiO3 ceramics. *Mater. Lett.* **58,** 1701–1705 (2004).

93. Zhang, Z. & Rishi, R. Influence of grain size on ferroelastic toughening and piezoelectric behavior of lead zirconate titanate. *J. Am. Ceram. Soc.* **78,** 3363–3368 (1995).

94. Knudsen, F. P. Dependence of mechanical strength of brittle polycrystalline specimens on porosity and grain size. *J. Am. Ceram. Soc.* **42,** 376 –387 (1959).

95. Garg, A. & Goel, T. Mechanical and electrical properties of PZT ceramics (Zr:Ti=0.40:0.60) related to Nd3+ Addition. *Mater. Sci. Eng. B* **60,** 128–132 (1999).

96. Hizebry, A., Saadaoui, M., Elattaoui, H., Chevalier, J. & Fantozzi, G. R-curve and subcritical crack growth in lead zirconate titanate ceramics. *Mater. Sci. Eng. A* **499,** 368–373 (2009).

97. Strecker, K., Ribeiro, S. & Hoffmann, M.-J. Fracture toughness measurements of LPS-SiC: a comparison of the indentation technique and the SEVNB method. *Mater. Res.* **8,** 121–124 (2005).

98. Okayasu, M., Sato, K. & Mizuno, M. Influence of domain orientation on the mechanical properties of lead zirconate titanate piezoelectric ceramics. *J. Eur. Ceram. Soc.* **31,** 141–150 (2011).

99. Wang, J. & Zhang, T. Y. Phase field simulations of polarization switching-

induced toughening in ferroelectric ceramics. *Acta Mater.* **55,** 2465–2477 (2007).

100. Lynch, C. Fracture of ferroelectric and relaxor electro-ceramics: influence of electric field. *Acta Mater.* **46,** 599–608 (1998).

101. Hatano, K., Yamamoto, A., Doshida, Y. & Mizuno, Y. Microstructural control of (Li,Na,K)NbO3 ceramics using additives. *J. C* **123,** 561–564 (2015).

102. Verdier, C., Lupascu, D. C. & Rödel, J. Stability of defects in lead–zirconate–titanate after unipolar fatigue. *Appl. Phys. Lett.* **81,** 2596–2598 (2002).

103. Guiffard, B., Boucher, E., Eyraud, L., Lebrun, L. & Guyomar, D. Influence of donor co-doping by niobium or fluorine on the conductivity of Mn doped and Mg doped PZT ceramics. *J. Eur. Ceram. Soc.* **25,** 2487–2490 (2005).

104. Luo, Z. *et al.* Effect of ferroelectric long-range order on the unipolar and bipolar electric fatigue in Bi0.5Na0.5TiO3-based lead-free piezoceramics. *J. Am. Ceram. Soc.* **94,** 3927–3933 (2011).

105. Glaum, J., Granzow, T., Schmitt, L. A., Kleebe, H.-J. & Rödel, J. Temperature and driving field dependence of fatigue processes in PZT bulk ceramics. *Acta Mater.* **59,** 6083–6092 (2011).

106. Miyata, N. & Jinno, H. Strength and fracture surface energy of phase-separated glasses. *J. Mater. Sci.* **16,** 2205–2217 (1981).

107. Pojprapai, S. *et al.* Frequency effects on fatigue crack growth and crack tip domain-switching behavior in a lead zirconate titanate ceramic. *Acta Mater.* **57,** 3932–3940 (2009).

108. Zhukov, S. *et al.* Dynamics of polarization reversal in virgin and fatigued ferroelectric ceramics by inhomogeneous field mechanism. *Phys. Rev. B* **82,** 014109–1–8 (2010).

109. Shvartsman, V. V., Kholkin, A. L., Verdier, C. & Lupascu, D. C. Fatigue-induced evolution of domain structure in ferroelectric lead zirconate titanate ceramics investigated by piezoresponse force microscopy. *J. Appl. Phys.* **98,** 094109 (2005).

110. Calderon-Moreno, J. M. Stress induced domain switching of PZT in compression tests. *Mater. Sci. Eng. A* **315,** 227–230 (2001).

Acknowledgements

First and foremost, I would like to express my sincere gratitude to my advisor Prof. Dr. Ken-ichi Kakimoto, for providing me with the opportunity to complete my PhD thesis at the Nagoya Institute of Technology. It has been an honor to be his first PhD student. I am very grateful for his patience, motivation, enthusiasm, and immense knowledge in piezoceramics that, taken together, make him a great mentor.

I would also like to thank my committee members, Prof. Dr. Manabu Gomi and Prof. Dr. Toru Asaka for serving as my committee members even at hardship. I also want to thank them for their insightful comments and suggestions.

My sincere thanks to present and past members of the laboratory of electroceramics. The group has been a source of good advice and great support. I am especially grateful for my tutor Kensuke Kato, who helped me during my first months in Japan.

I also wish to thank Taiyo Yuden Co., Ltd. for the overall support of my work and providing it with samples. Special thanks to Keiichi Hatano for sharing his knowledge and giving me invaluable advices.

For the non-scientific side of my thesis, a most heartfelt thanks to my family. Words cannot express how grateful I am to my stepfather, Jörg Ziegler and my mother, Birgit Martin-Ziegler, for all of the sacrifices that you've made on my behalf. To my Mom, thanks for all of the care packages and kind words of support. Thanks to my sisters, Oranna and Hannah, who are funny, witty, kind and caring. I'm glad we've only become better friends as we've gotten older. I would also like to thank all of my friends, old and new, who supported me in writing, and incented me to strive towards my goal. At the end I would like to express appreciation to my partner Narumi Shimizu for being loving, encouraging and supporting, especially in the moments when there was no one to answer my queries during the final stages of this PhD.